



LAWRENCE  
LIVERMORE  
NATIONAL  
LABORATORY

# Overview of the Physics and Engineering Design of NSTX Upgrade

J. Menard et. al

September 9, 2011

Nuclear Fusion

## **Disclaimer**

---

This document was prepared as an account of work sponsored by an agency of the United States government. Neither the United States government nor Lawrence Livermore National Security, LLC, nor any of their employees makes any warranty, expressed or implied, or assumes any legal liability or responsibility for the accuracy, completeness, or usefulness of any information, apparatus, product, or process disclosed, or represents that its use would not infringe privately owned rights. Reference herein to any specific commercial product, process, or service by trade name, trademark, manufacturer, or otherwise does not necessarily constitute or imply its endorsement, recommendation, or favoring by the United States government or Lawrence Livermore National Security, LLC. The views and opinions of authors expressed herein do not necessarily state or reflect those of the United States government or Lawrence Livermore National Security, LLC, and shall not be used for advertising or product endorsement purposes.

# Overview of the Physics and Engineering Design of NSTX Upgrade

J.E. Menard<sup>1</sup>, S. Gerhardt<sup>1</sup>, M. Bell<sup>1</sup>, J. Bialek<sup>2</sup>, A. Brooks<sup>1</sup>, J. Canik<sup>3</sup>, J. Chrzanowski<sup>1</sup>, M. Denault<sup>1</sup>, L. Dudek<sup>1</sup>, D.A. Gates<sup>1</sup>, W. Guttenfelder<sup>1</sup>, R. Hatcher<sup>1</sup>, J. Hosea<sup>1</sup>, R. Kaita<sup>1</sup>, S. Kaye<sup>1</sup>, C. Kessel<sup>1</sup>, E. Kolemen<sup>1</sup>, H. Kugel<sup>1</sup>, R. Maingi<sup>3</sup>, M. Mardenfeld<sup>1</sup>, D. Mueller<sup>1</sup>, B. Nelson<sup>4</sup>, C. Neumeyer<sup>1</sup>, M. Ono<sup>1</sup>, E. Perry<sup>1</sup>, R. Ramakrishnan<sup>1</sup>, R. Raman<sup>4</sup>, S. Sabbagh<sup>1</sup>, M. Smith<sup>1</sup>, V. Soukhanovskii<sup>5</sup>, T. Stevenson<sup>1</sup>, R. Strykowski<sup>1</sup>, G. Taylor<sup>1</sup>, P. Titus<sup>1</sup>, K. Tresemer<sup>1</sup>, M. Viola<sup>1</sup>, M. Williams<sup>1</sup>, R. Woolley<sup>1</sup>, H. Zhang<sup>1</sup>, Y. Zhai<sup>1</sup>, A. Zolfaghari<sup>1</sup>, and the NSTX Team

<sup>1</sup>Princeton Plasma Physics Laboratory, Princeton, NJ, USA

<sup>2</sup>Columbia University, New York, NY, USA

<sup>3</sup>Oak Ridge National Laboratory, Oak Ridge, TN, USA

<sup>4</sup>University of Washington, Seattle, WA, USA

<sup>5</sup>Lawrence Livermore National Laboratory, Livermore, CA, USA

**Abstract.** The spherical tokamak (ST) is a leading candidate for a fusion nuclear science facility (FNSF) due to its compact size and modular configuration. The National Spherical Torus eXperiment (NSTX) is a MA-class ST facility in the U.S. actively developing the physics basis for an ST-based FNSF. In plasma transport research, ST experiments exhibit a strong (nearly inverse) scaling of normalized confinement with collisionality, and if this trend holds at low collisionality, high fusion neutron fluences could be achievable in very compact ST devices. A major motivation for the NSTX Upgrade (NSTX-U) is to span the next factor of 3-6 reduction in collisionality. To achieve this collisionality reduction with equilibrated profiles, NSTX-U will double the toroidal field, plasma current, and NBI heating power and increase the pulse length from 1-1.5s to 5-8s. In the area of stability and advanced scenarios, plasmas with higher aspect ratio and elongation, high  $\beta_N$ , and broad current profiles approaching those of an ST-based FNSF have been produced in NSTX using active control of the plasma  $\beta$  and advanced resistive wall mode control. High non-inductive current fractions of 70% have been sustained for many current diffusion times, and the more tangential injection of the 2nd NBI of the Upgrade is projected to increase the NBI current drive by up to a factor of 2 and support 100% non-inductive operation. More tangential NBI injection is also projected to provide non-solenoidal current ramp-up as needed for an ST-based FNSF. In boundary physics, NSTX measures an inverse relationship between the scrape-off layer heat-flux width and plasma current that could unfavorably impact next-step devices. Recently, NSTX has successfully demonstrated substantial heat-flux reduction using a snowflake divertor configuration, and this type of divertor is incorporated in the NSTX-U design. The physics and engineering design supporting NSTX Upgrade is described.

PACS numbers: 28.52.Av, 52.25.Fi, 52.55.Fa, 52.55.Rk, 52.55.Wq

## 1. Introduction

The spherical tokamak (ST) [1, 2] is a leading candidate for a Fusion Nuclear Science Facility (FNSF) due to its compact size and modular configuration [3, 4]. The National Spherical Torus eXperiment (NSTX) [5, 6] is a MA-class ST facility in the U.S. actively developing the physics basis for an ST-based FNSF. Access to low collisionality  $\nu^*$  plasmas in the ST configuration is particularly important to more fully understand transport, stability, and non-inductive start-up and sustainment in the ST. In particular, NSTX [7] and MAST [8, 9] observe a strong inverse scaling of normalized confinement with  $\nu^*$ . An example of this scaling is shown in Figure 1 for NSTX neutral beam heated H-mode experiments in which the plasma  $q, \beta$ , and  $\rho_*$  were approximately fixed as the electron collisionality  $\nu_e^*$  was varied by a factor of 3. If the strong favorable scaling of increased dimensionless confinement  $\Omega_i \tau_E \propto B_T \tau_E$  with reduced collisionality holds at low collisionality, high fusion neutron fluxes and fluences could be achievable in very compact ST devices only 30-50% larger in major radius than existing ST devices, thereby enabling a reduced size and cost ST-based Fusion Nuclear Science Facility (ST-FNSF). On the other hand, there is evidence from conventional aspect ratio tokamaks operating in H-mode that the collisionality exponent in the dimensionless confinement scaling may depend on the collisionality itself [10]. In particular, from Figure 22 of Reference [10], the collisionality exponent is near -0.75 for  $\nu_i^* \approx 1$  in C-Mod, -0.25 for  $\nu_i^* \approx 0.01$  in JET, and is nearly zero in the ITER IPB98(y,2) H-mode scaling [11, 12] which varies as  $B_T \tau_E \propto \rho_*^{-0.70} \beta^{-0.90} \nu_*^{-0.01} q^{-3.0} \epsilon^{0.73} \kappa^{2.3}$ . Further, while the range of  $\nu_e^*$  available from scaling studies on NSTX is limited, the data in Figure 1 (not the fit to the data) may be consistent with a weakening dependence of  $B_T \tau_E$  on  $\nu_e^*$  as  $\nu_e^*$  is reduced. To more definitively determine the scaling of confinement with collisionality in regimes representative of next-step STs, an additional factor of 3-6 reduction in  $\nu^*$  is needed to overlap with the upper-end of  $\nu^*$  values for an ST-FNSF, and access to this reduced collisionality is a major motivation for the Upgrade of NSTX. Given the strong dependence of the ITER confinement scaling on  $\beta$  and elongation  $\kappa$ , continued access to high  $\beta$  and  $\kappa$  will also continue to be important to assess ST confinement dependence on these parameters.

For high-power ST H-mode plasmas, the electron and ion thermal diffusivities are found to have different scaling dependencies [13]. In particular, the ion confinement is typically near neoclassical values in the outer half of the plasma minor radius and has a nearly linear plasma current dependence. In contrast, the electron confinement is anomalous and has a nearly linear toroidal field dependence. Several instabilities potentially responsible for anomalous electron thermal transport have been studied in NSTX including Electron Temperature Gradient (ETG) modes [14, 15, 16, 17, 18],

Global Alfvén Eigenmodes (GAE) [19, 20], and micro-tearing modes [21, 22, 23, 24].

Unraveling the simultaneous effects of these instabilities is a major research goal of NSTX Upgrade by extending the achievable collisionality, toroidal field, and plasma current. For example, ETG-driven anomalous diffusivity is expected to depend on magnetic field strength through the electron larmor radius scaling [25] (and possibly on  $\beta$ ), the GAE instability drive [20] is expected to depend on the fast ion velocity normalized to the Alfvén speed, the fast-ion  $\beta$  fraction, and the fast-ion distribution function anisotropy, and micro-tearing-induced anomalous transport is expected to depend on collisionality and also on magnetic field strength through electron larmor radius scaling [22].

As shown in Figure 2, recent nonlinear gyrokinetic simulations of micro-tearing-induced electron transport [24] have shown reasonable agreement with experimentally inferred electron thermal diffusivities for the limited range of shots and minor radii tested and ignoring  $E \times B$  shear. It should be noted that the inclusion of experimental values of  $E \times B$  shear can reduce or suppress the predicted micro-tearing transport, but modest increases in temperature gradient can recover experimentally relevant transport. These simulations indicate that micro-tearing-induced electron transport should continue to scale nearly linearly with collisionality over approximately one order of magnitude in collisionality as the collisionality is reduced below present NSTX values. Thus, collisionality variation could impact which type(s) of instabilities dominate anomalous electron transport in NSTX Upgrade plasmas. Beyond impacting turbulent transport, reduced collisionality could also impact toroidal rotation damping [26, 27, 28], RWM stability [28, 29], error-field correction [30, 31], pedestal stability [32], and many other physics areas.

To improve the understanding of ST confinement, stability, and other physics, a major upgrade to NSTX is planned to span the next factor of 3-6 reduction in collisionality while also extending regimes and capabilities including fully non-inductive current ramp-up and sustainment and the development of mitigation techniques for high heat flux. The physics and engineering design of NSTX Upgrade is described in detail in Section 2 and is summarized in Section 3.

## 2. Physics Requirements and Engineering Design

### 2.1. Physics Requirements

#### 2.1.1. Overview

As described in Section 1, access to reduced collisionality is a major research goal of NSTX Upgrade. Reduced normalized collisionality (ratio of collision frequency to bounce frequency)  $\nu^* \propto qRn/T^2\epsilon^{3/2}$  [33] requires increased temperature  $T$  and/or

reduced density  $n$  for fixed plasma major radius  $R$ , inverse aspect ratio  $\epsilon = 1/A$ , and safety factor  $q$ . Combining Troyon scaling [34, 35, 36, 37] for the  $\beta$  limit:  $nT \propto \beta_N I_P B/a$  with the Greenwald density limit [38, 39] scaling:  $n \propto I_P/a^2$  implies  $T \propto \beta_N a B/f_{GW}$  where  $\beta_N$  is the normalized  $\beta$ ,  $a$  is the minor radius,  $B$  is the magnetic field strength, and the Greenwald density fraction  $f_{GW} \equiv \bar{n}_e[10^{20}m^{-3}]/I_P[MA]$ . Thus, at fixed  $f_{GW}$  and  $\beta_N$ , increased  $T$  requires increased  $B$  and is the major motivation for increased magnetic field strength in NSTX Upgrade. Using these definitions and assuming fixed geometry, it follows that  $\nu^* \propto f_{GW}^3/\beta_N^2 B_T$ . Here the vacuum toroidal field  $B_T$  at the plasma geometric center  $R_0$  is used for  $B$ ,  $\beta_T \equiv 2\mu_0\langle p\rangle/B_T^2$ , and  $\beta_N \equiv \beta_T a B_T/I_P$  with units of  $\%mT/MA$ . This scaling for  $\nu^*$  highlights the importance of access to low  $f_{GW}$  and high  $\beta_N$  and  $B_T$  for achieving low collisionality. To access similar safety factor  $q$  at higher  $B_T$ ,  $I_P$  should be scaled linearly with  $B_T$ , sufficient auxiliary heating power  $P_{heat}$  should be provided to access the desired  $\beta_N$ , and the required  $P_{heat}$  will depend on the confinement scaling.

The research goals of NSTX Upgrade extend beyond accessing reduced collisionality. In particular, it is also important to address non-inductive ramp-up and sustainment, the establishment of equilibrated integrated scenarios, ST confinement and stability scaling and understanding, high-power and particle exhaust understanding and mitigation, and investigations of advanced operating scenarios, respectively. Scoping studies of NSTX-U operating scenarios are important for identifying and meeting the Upgrade performance requirements to achieve these physics research goals. To satisfy these performance requirements, five representative NSTX-U operating scenarios are investigated and motivate the Upgrade design: (1) 100% non-inductive current drive, (2) partially-inductively-driven long-pulse, (3) high/maximum plasma current, (4) high current plus high heating power and divertor heat flux, and (5) high bootstrap fraction with high confinement. Table 1 summarizes parameters of interest for these five NSTX-U scenarios projected from NSTX data using 0-D scaling analysis supported by TRANSP simulations. Table 1 also includes comparisons of TRANSP analysis for three NSTX experimental discharges to corresponding 0-D scalings for benchmarking purposes, and also includes parameters for a computed NSTX reference scenario at two densities. A more comprehensive exploration of NSTX Upgrade equilibrium scenarios calculated using free-boundary TRANSP simulations can be found in Reference [40].

### 2.1.2. Scenario Projection Methodology

Three representative NSTX discharges are analyzed using TRANSP to form a 0-D scaling model for defining an NSTX reference scenario and for projecting to NSTX Upgrade scenarios. This 0-D scaling model is also consistent with confinement scaling results for NSTX advanced scenarios [41]. The NSTX NBI-heated H-mode discharges

used here all have an ITER IPB98(y,2) confinement enhancement factor  $H_{98} = 1.0$ , span a range of  $f_{GW}$  from 0.6 to 0.95 and have  $I_P = 0.7 - 1.3\text{MA}$ ,  $A = 1.45 - 1.5$ , and  $\kappa = 2.45 - 2.6$ . Profile peaking factors for the temperature, density, and pressure (thermal and fast) in the 0-D model are taken from the average values from the 3 discharges, and the total pressure profile peaking factor includes the contribution from the model-estimated fast-ion pressure. As shown on the left-hand side of Table 1, there is good agreement (as expected) between the 0-D scaling model predictions and TRANSP calculations for the volume-average temperatures, profile peaking factors, thermal and fast stored energy and  $\beta$  values, bootstrap fraction, and NBI current drive. The middle (white columns) of Table 1 show parameters for an NSTX reference scenario with  $I_P = 1\text{MA}$  computed from the 0-D model for density values  $f_{GW} = 0.5$  and 1.0. These  $f_{GW}$  values span the lower and upper bounds of NSTX normalized density (see Figure 3) and allow direct comparison with NSTX Upgrade scenario projections which use the same  $f_{GW}$  values as shown on the right-hand side of Table 1.

An overview of the calculations and assumptions for the NSTX Upgrade scenarios in Table 1 is as follows: The NSTX Upgrade aspect ratio  $A$  is fixed at 1.7 and the elongation  $\kappa$  is fixed at 2.75. These values are based on typical results obtained with free-boundary equilibrium calculations. The toroidal field values chosen are 0.75T to access high  $\beta$  and/or long pulse, and 1.0T for elevated  $q$  and/or access at least a factor of 2 reduction in  $\nu^*$ . NSTX Upgrade scenarios are evaluated assuming two confinement scalings: ITER IPB98(y,2) H-mode scaling [11, 12] (with a confinement scaling multiplier of unity, i.e.  $H_{98} = 1$ ) and an ST-specific confinement scaling based on combined NSTX and MAST scalings described in more detail in Section 2.1.3. For the 0-D scalings described here, the effects of toroidal rotation are ignored. However, estimates of the projected toroidal rotation normalized to the NSTX reference scenario are also provided in Section 2.1.3 and in Table 1.

One potential issue for operation at high density is a degradation of confinement. In particular, achieving  $H_{98} = 1$  with  $f_{GW} = 1$  may not be possible without sufficient boundary shaping [12]. However, high triangularity has been shown to enable access to  $H_{98} = 1$  with  $f_{GW}$  approaching 1 [42, 43]. To address this issue, Figure 3a shows the NSTX confinement multiplier  $H_{98}$  versus Greenwald fraction using the confinement database from Section 4.2 of Reference [41]. As is evident from the figure, there is no obvious degradation of confinement multiplier with normalized density for this database of NSTX plasmas with a wide range of plasma parameters and where all shots use at least some lithium conditioning of the PFCs [41]. One possible explanation for this weak dependence of  $H_{98}$  on density is the high triangularity and strong boundary shaping already incorporated in most NSTX operating scenarios [44, 41]. Figure 3a also shows that  $0.5 \leq f_{GW} \leq 1.05$  bounds nearly all of the NSTX data in this dataset, and Figure 3b

shows that  $f_{GW}$  in the range of  $0.6 - 0.9$  is more representative of higher  $I_P$  operation in NSTX. Based on these results,  $f_{GW} \approx 0.75$  is taken to be most representative of NSTX operation, and NSTX Upgrade scenarios are calculated at bounding values of  $f_{GW} = 0.5$  and  $1.0$  in Table 1. However, from Figure 3b it is also evident that it is typically difficult to access high Greenwald fraction at high plasma current in NSTX. This is due in large part to the reduced flat-top duration (due to limited solenoid flux) at high current which does not provide sufficient time for the density to reach high  $f_{GW}$  or to approach equilibrated conditions. Thus, increased flat-top duration in NSTX Upgrade would significantly aid density limit studies at high current. Figure 3c shows  $H_{98}$  versus elongation and may indicate a weak degradation in normalized confinement with increased elongation. However,  $H_{98} \geq 1$  has been achieved for  $\kappa \leq 2.75$  in NSTX and supports using  $H_{98} = 1$  and  $\kappa = 2.75$  for NSTX Upgrade scenario projections as used in Table 1.

Using the assumed toroidal field, confinement model, and normalized density fraction, it is straightforward to project the thermal stored energy, volume-average temperatures (based on scaled NSTX profile shapes), and plasma resistivity and NBI current drive efficiency assuming a constant  $Z_{eff} = 2.5$ . To account for the fact that the electrons are typically the dominant energy loss channel in NSTX, and to approximate the effects of collisional coupling between electrons and ions as the density is varied, the ratio  $T_i/T_e$  is linearly reduced from 1.12 to 1.02 as the Greenwald fraction is increased from 0.5 to 1 in the NSTX Upgrade scenario projections. It should also be noted that for the 80-100keV deuterium NBI heating of NSTX, the power to the electrons and ions is approximately equal when  $T_e = 1.2\text{keV}$ , and more power goes to the ions for higher electron temperatures. With the toroidal field, plasma current, and electron temperature determined, the normalized electron collisionality  $\nu_e^*$  in Table 1 is calculated at fixed  $\epsilon = A^{-1}$  at a representative  $q$  surface in the plasma core (taken to be  $q = 2$ ) and also for the cylindrical safety factor  $q^* \equiv \epsilon(1 + \kappa^2)\pi a B_T / \mu_0 I_P$  to better account for  $q$  variation from scenario to scenario.

The NSTX Upgrade scenario pulse durations are designed to utilize most or all of the TF flat-top and/or available OH solenoid flux. In particular, all of the Table 1 scenarios with heating powers of 10MW or below have  $I_P$  flat-top values of 5s or more to provide a number of current redistribution times comparable to or larger than the number in the NSTX reference scenario. For scenarios requiring flat-top inductive current drive, the pulse duration requirement, plasma resistivity, and surface voltage required to support a given plasma current are used to determine the required OH solenoid flux and to ensure the flux used does not exceed the total available flux.

For the neutral beam heating and current drive calculations, an NBI full energy of injection  $E_{NBI} = 80\text{keV}$  is typically used, except for the  $P_{NBI} = 15\text{MW}$  scenario



which has  $E_{NBI} = 100\text{keV}$ . The fast-ion stored energy is assumed to be proportional to the product of  $P_{NBI}$  and the fast-ion thermalization time [45, 46] and is normalized to TRANSP fast-ion stored energy calculations for NSTX. The fast-ion and thermal stored energies are then used to compute the total stored energy,  $\beta_N$ , and  $\beta_T$  values. The NBI current drive efficiency [47] is assumed to be proportional to  $P_{NBI}T_e(1 - 1/Z_{eff})/n_e$  [48, 49] and is normalized to TRANSP NBI current drive calculations which have been previously shown good agreement with experimentally inferred values in NSTX [50, 51] when core MHD activity is sufficiently weak. The bootstrap current fraction [52, 53, 54]  $f_{BS} = I_{BS}/I_P$  is assumed to scale as  $C_{BS}\sqrt{\epsilon}\beta_{pol-th}$  where  $\beta_{pol-th}$  is the poloidal beta using the thermal pressure and  $C_{BS} = 0.52$  is used based on NSTX bootstrap current fraction analysis from TRANSP. Once the bootstrap current and NBI current are calculated for a given scenario, these currents are subtracted from the total scenario target current, and the remaining current must be provided by inductive current drive. The plasma  $T_e$  and  $Z_{eff}$  are used to calculate a plasma resistance value and to compute the required surface voltage to drive any inductive current.

### 2.1.3. Energy and Momentum Confinement

The thermal energy confinement scalings used in the 0-D scenario projections are assumed to vary as  $\tau_{E,thermal} \propto I_P^{\alpha_I} B_T^{\alpha_B} n^{\alpha_n} P^{\alpha_P} R^{\alpha_R} \epsilon^{\alpha_\epsilon}$ . The ST confinement scaling exponents from NSTX using OLS (ELMy) analysis [55] are:  $\alpha_I = 0.58, \alpha_B = 1.01, \alpha_n = 0.43, \alpha_P = -0.70$ . Similarly, the scaling exponents from MAST also using OLS analysis [8] and assuming the thermal stored energy is linearly proportional to the total stored energy are:  $\alpha_I = 0.59, \alpha_B = 1.4, \alpha_n = 0.0, \alpha_P = -0.73$ . It should be noted that OLS and PCEIV analyses give similar but not identical exponents for the engineering variables in each of the NSTX and MAST scalings, and the differences in the exponents for the different analysis methods are comparable to the values of the uncertainties of the exponents themselves. Further, to account for the differences between the NSTX and MAST exponents, the ST-specific confinement scaling used in all subsequent analysis shown in Table 1 uses the average value of the exponents from NSTX and MAST rounded to the nearest single decimal place, namely:  $\alpha_I = 0.6, \alpha_B = 1.2, \alpha_n = 0.2, \alpha_P = -0.7$ . The major radius and inverse aspect ratio exponents are taken from the ITER IPB98(y,2) H-mode scaling:  $\alpha_R = 2.0, \alpha_\epsilon = 0.6$ . The elongation dependence is ignored here since a fixed value  $\kappa=2.75$  is used in the 0D analysis for NSTX Upgrade. The ST-specific confinement scaling coefficient is chosen based on matching the ITER scaling  $\tau_E$  for the NSTX reference scenario in Table 1 with  $I_P = 1\text{MA}$ ,  $B_T=0.45\text{T}$ ,  $A=1.5$ ,  $R_0 = 0.86\text{m}$ ,  $\kappa=2.6$ ,  $P_{NBI} = 6\text{MW}$ , and  $f_{GW} = 1$ .

With respect to collisionality reduction relative to the NSTX reference scenario, a factor of 4-5 decrease in collisionality is projected to be achievable at fixed Greenwald

fraction by operating at 1T, 1.5MA, and 6MW assuming ST confinement scaling (right-most green columns). This strong decrease in collisionality at current and power values similar to the present NSTX is the result of the strong toroidal field dependence of the ST confinement scaling. In contrast, if ITER H-mode confinement scaling is assumed, only a factor of 2-3 reduction in collisionality would be achieved even with two times higher current and/or power (red and left-most NSTX-U green columns) due to the weak toroidal field dependence of the ITER confinement scaling. Thus, the ability to double the toroidal field, plasma current, and heating power is needed to reduce the uncertainty in the scaling of ST energy confinement as plasma temperatures are increased toward the values of next-step STs.

An important requirement for achieving reduced ion collisionality through increased ion temperature is to suppress ITG/TEM ion-gyro-scale turbulence. Previous confinement studies in NSTX have shown the ion thermal diffusivity in NBI-heated H-mode plasmas is near neoclassical values in the outer half of the minor radius [7]. This is consistent with the likely suppression of low-k turbulence since the  $E \times B$  shearing rate  $\gamma_E = (r/q)d(E_r/RB_P)/dr \approx -(r/q)\partial\Omega_\phi/\partial r$  [56, 57] significantly exceeds the ITG/TEM maximum linear growth rate  $\gamma_{lin}$  [7]. Here  $\Omega_\phi = v_\phi/R$  is the toroidal angular rotation frequency,  $v_\phi$  is the toroidal rotation velocity,  $R$  is the major radius, and the poloidal rotation and pressure gradient terms in the radial force balance equation used to determine  $E_r$  have been ignored. To estimate the approximate magnitude of the toroidal rotation velocity  $v_\phi$  in NSTX Upgrade, we note that the angular momentum flux  $\Gamma_\phi = -mnR\chi_\phi\partial v_\phi/\partial r + mnRv_{pinch}v_\phi$  has both a diffusive and a pinch contribution [58]. Here  $m$  and  $n$  are the ion mass and density respectively. The angular momentum diffusivity  $\chi_\phi$  is anomalous and generally exceeds the neoclassical momentum diffusivity by a large factor, and a predictive capability for  $\chi_\phi$  does not yet exist. However, in the outer region of the plasma, the momentum pinch measured in NSTX is in reasonable agreement with a low-k turbulence-driven pinch term of the form:  $Rv_{pinch} \approx -\chi_\phi(4 + R/L_n)$  where  $L_n$  is the density gradient scale-length [59, 58]. Using this expression for the pinch term, the momentum flux can be approximated as  $\Gamma_\phi \approx -mn\chi_\phi[R\partial v_\phi/\partial r + (4 + R/L_n)v_\phi]$ , and in steady-state,  $\nabla \cdot \Gamma_\phi = S_\phi$  where  $S_\phi$  is a source term for angular momentum (i.e. NBI). Assuming similar profile shapes between NSTX and NSTX Upgrade, then  $v_\phi \propto S_\phi/n\chi_\phi$ . The values of  $\chi_\phi$  in the outer region of the plasma in NSTX are observed to be roughly proportional to  $\chi_i$ , and after accounting for the inward pinch term in the analysis, the Prandtl number  $\chi_\phi/\chi_i \approx 0.5 - 0.8$  [58]. Assuming  $\chi_\phi \propto \chi_i$ , then  $v_\phi \propto S_\phi/n\chi_i$ , and if  $\chi_i \approx \chi_{i-neo}$ , then  $v_\phi \propto S_\phi T_i^{1/2} I_P^2/n^2$ . The validity of this scaling for  $v_\phi$  is clearly questionable, as it remains unclear if  $\chi_\phi$  in NSTX scales with either the turbulent or neoclassical  $\chi_i$ , and this is a topic for future research.

Nevertheless, the above 0-D scaling for  $v_\phi$  can be applied to the scenarios in Table 1

which tabulates the projected toroidal rotation normalized to the NSTX reference cases at the same Greenwald density fraction. The calculations indicate that the toroidal rotation could be up to 4 times larger in the Upgrade and approximately a factor of two higher on average considering all of the Upgrade scenarios in Table 1. Finally, it is noted that the ITG/TEM linear growth rate  $\gamma_{lin}$  is proportional to  $T_i^{1/2}$ , and that for all the scenarios with strong NBI heating,  $\gamma_E/\gamma_{lin}$  in NSTX-U will be comparable to or will exceed the NSTX ratio. Thus, it is expected that ITG/TEM turbulence will remain largely suppressed. However, the low-NBI-power scenario with high bootstrap fraction has a ratio  $\gamma_E/\gamma_{lin} \approx 1/3$  of the NSTX reference value, so it is questionable whether the turbulent ion thermal diffusivity would remain sub-dominant to the neoclassical diffusivity in this scenario.

#### 2.1.4. Pulse Duration Requirements

The required coil and plasma current pulse duration is another important consideration for the design of NSTX-U. The current redistribution time [60]  $\tau_{CR}$  is generally the longest profile relaxation time-scale, and on NSTX, 3-4 current redistribution times are typically required to achieve an equilibrated  $q$  profile. If the confinement continues to scale nearly inversely with collisionality at low collisionality, the current redistribution time could increase as much as a factor of 5 (compare right-most green columns Table 1 to NSTX reference values). Thus, to ensure similar profile relaxation in the Upgrade, the plasma current and TF flat-top durations must increase by a factor of 5 to 5s and 6.6s, respectively.

#### 2.1.5. Ohmic Heating Solenoid Flux Requirements

To assess ST physics at 2 times higher TF and similar safety factor  $q$ , the plasma current must double from 1MA to 2MA. Sufficient loop voltage must also be provided for any needed inductive current drive. The operating scenario analysis indicates that 2MA plasmas at intermediate power levels (10MW) assuming ITER confinement scaling and Greenwald fraction of 1 require the highest surface voltage (0.2V) for sustainment, and these scenarios determine the required flat-top OH flux of approximately 1Wb to sustain a 5s plasma current flat-top.

In addition to the flat-top flux, plasma initiation and current ramp-up are also important considerations for specifying the OH flux requirement. For plasma initiation/breakdown, the magnetic null quality and/or toroidal electric field must be sufficiently high for the plasma electron avalanche to occur to form a closed flux surface tokamak configuration. A key metric for plasma breakdown is the electron energy gained before loss to the surrounding walls via parallel transport along the total (toroidal + poloidal) background magnetic field, and this gain is proportional to the Lloyd parameter

$E_\phi B_\phi / B_\perp$  [61]. The NSTX Lloyd parameter is typically 4.2kV/m at the major radius of the centerstack where plasma breakdown is initiated ( $R_{BD}=0.185\text{m}$ ) for a stray poloidal field  $B_\perp$  of 10 Gauss in the field-null region and a nominal toroidal field  $B_T = 0.36\text{T}$  (60% of maximum toroidal field) at the plasma geometric center ( $R_0 = 0.86\text{m}$ ). This value of the Lloyd parameter provides reliable plasma break-down in NSTX for all toroidal field values commonly used in the experiment, and the same specification is used for NSTX Upgrade ( $R_{BD}=0.315\text{m}$ ) for a nominal toroidal field  $B_T = 0.6\text{T}$  (again 60% of maximum toroidal field) at the Upgrade plasma geometric center ( $R_0 = 0.93\text{m}$ ). To achieve this in the Upgrade, the available breakdown loop voltage is increased from 2.9 to 4.7V which requires an increase in the OH power supply voltage from 2.7kV to 4.1kV.

The ohmic flux required for plasma current ramp-up is a function of the plasma resistance which is a function of plasma temperature and  $Z_{eff}$ , and is therefore a function of auxiliary heating and current drive and confinement scenario (L-mode vs. H-mode). NBI heating and an early H-mode transition [62, 63] during the current ramp-up are commonly used on NSTX to minimize OH flux consumption to maximize the current flat-top duration. To illustrate the impact of NBI heating and H-mode transition during the current ramp, Figure 4 compares the ramp-up evolution of ohmic L-mode versus early-NBI + H-mode plasmas with similar  $I_P$  ramp-rate and other initial plasma parameters. Sufficient NBI heating power is required (typically 3-4MW) to induce H-mode during the current ramp, and a brief 10-20ms pause in the  $I_P$  ramp is also sometimes used to reduce the H-mode threshold power to induce H-mode. As shown in Figure 4a for the NBI + H-mode case, 2MW of NBI power is injected at  $t=50\text{ms}$  followed by an additional 2MW of heating power at  $t=100\text{ms}$ , and the H-mode is induced (without a pause in the current ramp) at  $t=125\text{ms}$ . As shown in Figure 4b, the evolution of the surface voltages are similar for the ohmic L-mode and NBI + H-mode plasmas prior to the application of NBI heating at  $t=50\text{ms}$ . As shown in Figure 4b, following the application of NBI heating power at  $t=50\text{ms}$ , the resistive component [64, 65] (green) of the surface voltage decreases from 1.4V to 0.6V by the time of H-mode onset while the inductive component (blue) decreases only slightly. Figure 4b also shows that following the H-mode transition, the resistive component decreases further, and that the inductive component decreases from 0.7V to 0.3-0.4V compared to the ohmic L-mode value of 0.8V. Thus, the largest reduction in surface voltage in the NBI + H-mode ramp-up is from the reduction in the resistive component, but both components are reduced by NBI + H-mode during the ramp-up. It should also be noted that any NBI current-drive associated with the NBI heating during the ramp-up will also contribute to the reduction of the surface voltage required for current ramp-up. Overall, the combination of early NBI + H-mode reduces the required surface voltage by a factor of 2 to 2.5 following the H-mode transition, and this significantly reduces the solenoid flux consumed during the

current ramp.

Given the difficulty of accurately modeling the flux consumption required for break-down and ramp-up, Figure 5 shows the flux used to achieve a given flat-top plasma current in NSTX for usage in extrapolating to NSTX Upgrade. As shown in Figure 5a, the total break-down plus ramp-up flux consumption for NBI + H-mode extrapolates to 0.73Wb for NSTX shapes, which corresponds to 0.8Wb for NSTX Upgrade plasmas with larger major radius. Figure 5a also shows that the Ohmic L-mode ramp-up extrapolates to a significantly higher solenoid flux requirement of 1.22Wb for NSTX plasma shapes which corresponds to 1.4Wb for NSTX Upgrade plasmas. As shown in Figure 5b, the major-radius-normalized total poloidal flux consumption (Ejima-Wesley coefficient [64, 66]) extrapolates to 0.3-0.35 for the NBI + H-mode ramp-up which is 50-55% of the Ohmic L-mode value and approximately 60% of the ohmic plasma value reported previously in NSTX [65] for current ramp-rates near 5MA/s. Thus, including the breakdown+ramp-up flux required (0.8Wb) assuming NBI + H-mode during the ramp-up in addition to the current flat-top flux (1Wb), the total OH flux required is estimated to be 1.8-2Wb to support 2MA plasma current with 5s flat-top.

If NBI heating + H-mode confinement was not utilized in the current ramp, the total solenoid flux requirement would increase by approximately 30% and require a 13 – 15% increase in the diameter of the centerstack. Such an increase would increase the minimum (i.e. limiter to limiter) aspect ratio of NSTX Upgrade from 1.5 to 1.6 and eliminate the ability to achieve diverted plasmas with aspect ratios matching those of proposed future STs with  $A \leq 1.6$  such as ARIES-ST. Further, such a diameter increase would also significantly reduce the remaining horizontal inboard divertor surface area and eliminate the space for additional divertor coils. Such considerations strongly influence the choice of diameter of the centerstack and OH solenoid and therefore motivate the usage of NBI heating + H-mode during the plasma current ramp of NSTX Upgrade.

#### 2.1.6. Access to High Beta

The ability to access normalized and toroidal beta values in NSTX-U comparable to those achieved in NSTX is also important for assessing the stability and transport as a function of beta and  $\nu^*$  at reduced  $\nu^*$ . As is evident from Table 1, for the ST confinement scaling, access to high temperature and beta is achievable with heating power comparable to that in NSTX. However, for ITER H-mode scaling, substantially more power (factor of 2-3 times higher) is required to achieve similar beta values at similar safety factor  $q^*$  (see middle yellow and red NSTX-U columns in the Table). The poloidal field coil system must also be capable of providing sufficient field to maintain equilibrium force balance to access high  $\beta$  values at full toroidal field and plasma current.

For NSTX,  $\beta_T = 20 - 25\%$  and  $\beta_N = 4.5 - 6$  have been sustained for many energy confinement times and at least a current redistribution time [41]. As is evident from Table 1, access to similar performance values in NSTX Upgrade requires supporting plasmas with stored energy  $W_{TOT}$  up to 1.35MJ. Access to the with-wall  $\beta_N$  limit  $\leq 6.5$  and  $l_i$  up to 0.6 [41] requires additional poloidal field capability for  $W_{TOT}$  up to 1.5 – 1.6MJ.

### 2.1.7. Poloidal Field Requirements

To enable engineering design of the upgrade, systematic free-boundary equilibrium calculations have been performed to determine the Upgrade poloidal field requirements. The design range spans aspect ratio  $A = 1.6$  to  $1.9$ , internal inductance  $l_i = 0.4$  to  $1.1$ , elongation  $\kappa = 2.1$  to  $2.9$ , triangularity  $\delta = 0.2$  to  $0.7$ , squareness  $\zeta = -0.15$  to  $0.12$ , magnetic balance  $\delta_{Rsep} = -1.5$  to  $0$ cm, normalized beta  $\beta_N = 1, 5$ , and  $8$ , and OH solenoid current  $= 0$  and  $\pm 24$ kA (i.e. the power supply limits) to determine the divertor poloidal field (PF) needed for cancellation of OH leakage flux. Figure 6 shows the 32 plasma boundaries of free-boundary equilibria used for assessing the PF coil current requirements for 2MA NSTX Upgrade plasmas. Each boundary shown is actually a plot of three plasma boundaries for each state of the OH coil current described above, and this set of 96 equilibria provides the set of configurations used for the detailed engineering design of the Upgrade. The PF coil currents for each configuration are shown in Figure 7 for 2MA plasmas with  $\beta_N = 5$ , and the PF coil locations and sizes and the minimum and maximum currents as a function of  $\beta_N$  are shown in Figure 8. As is evident from Figure 8, the most substantial changes in coil current for varied  $\beta_N$  are for the primary vertical field coil (PF5) and the inner-most divertor coil (PF1A).

In addition to accounting for variation in the plasma shape, the PF coil current requirements have also been assessed as a function of plasma current profile (internal inductance) and normalized beta for 2MA, 1T plasmas. The plasma inductance and beta primarily influence the required vertical field (PF5) coil current, and as shown in Figure 9, increased inductance and beta both increase the required vertical field. The Upgrade power supply system [67] is designed to increase the maximum PF5 current by 50% from 20kA to 30kA nominal maximum operating current. This enhancement will enable 2MA equilibria with  $\beta_N$  up to 5 at  $l_i = 1$ , and  $\beta_N$  up to 8 at  $l_i = 0.6$ , and this increased vertical field capability supports all scenarios used for the Upgrade design, including access to the with-wall  $\beta_N$  limit. For reference, the NSTX Upgrade OH and PF coil turns-count and minimum and maximum currents used for the electromagnetic forces and structural analysis are summarized in Table 2. It should be noted that the PF2 and PF4 power supplies are nominally unipolar in the present NSTX and in the NSTX Upgrade design but can be upgraded to bipolar operation.

### 2.1.8. Vertical Control Requirements

In addition to providing sufficient field for plasma equilibrium, the PF coil and power supply system must also provide robust vertical position control. NSTX uses the rt-EFIT real-time equilibrium reconstruction algorithm [68] for real-time shape and vertical position control [69, 70, 71, 72] which has enabled the sustainment of high elongation  $\kappa = 2.5 - 2.8$  plasmas with high performance [44, 41]. Very high  $\kappa = 2.8 - 3$  has also been controlled for shorter durations in NSTX [63]. The vertical stability and controllability of the tokamak plasma is a function of the internal inductance, plasma pressure, distance between the plasma and the conducting wall, the location and type of sensors used for measuring vertical position, and the plasma aspect ratio and boundary shape [73, 74, 75, 76, 77, 1, 78, 79]. Assessing the impact of increased  $A$  and  $\kappa$  on ST confinement and stability is an important objective of NSTX Upgrade research. Increased  $A$  and  $\kappa$  are both destabilizing to the  $n = 0$  mode, and this trend has motivated dedicated experiments in NSTX to simultaneously increase  $A$  and  $\kappa$  (by increasing the inboard plasma-wall gap) in order to determine the  $n = 0$  controllability space for boundary shapes similar to those expected in NSTX Upgrade [41]. In these dedicated experiments, plasmas with  $A = 1.65 - 1.75$  and  $\kappa = 2.7 - 2.9$  were formed and controlled and the natural evolution of the current profile provided variation (i.e. an increase) of  $l_i$ .

Figure 10a shows the NSTX experimental  $\kappa$  versus  $l_i$  operating space sorted by aspect ratio with the lowest  $A = 1.2 - 1.4$  in red, typical NSTX  $A = 1.4 - 1.6$  in blue, and the highest  $A = 1.6 - 1.8$  in green from the experiments dedicated to producing NSTX Upgrade-like shapes. As is evident from Figure 10a,  $\kappa \approx 2.7 - 2.8$  has been sustained for  $l_i < 0.65$  for a range of aspect ratios  $A = 1.4 - 1.8$  which includes aspect ratios  $A = 1.6 - 1.8$  anticipated for NSTX Upgrade. However, for the cases with  $A = 1.6 - 1.8$ , loss of vertical control occurred for  $l_i \geq 0.65$  indicating that control of higher  $\kappa$  and/or high  $\kappa$  at higher  $l_i$  will require vertical control improvements such as improved plasma vertical motion detection utilizing more magnetic sensors (recently implemented) and control gain optimization (planned) [72]. Typical  $l_i$  values for NSTX high-performance plasmas are  $0.5 - 0.65$  [51, 41]. Most importantly, the  $A = 1.7$ ,  $\kappa = 2.7 - 2.8$  plasmas obtained thus far have  $l_i \leq 0.55$  [41], and these plasmas and parameters (indicated by the square black symbol in Figure 10a) provide the basis for the 0-D scalings in Table 1. Further, these higher aspect ratio plasmas obtained in NSTX also provide the basis for free-boundary TRANSP projections to NSTX Upgrade [40] including an assessment of the equilibrium and kink stability properties as a function of confinement and profile assumptions, gap between the plasma and outer limiter and conducting wall, anomalous fast-ion diffusivity, and impurity concentration.

A potentially important consideration for NSTX Upgrade vertical stability (and

$n > 0$  stability) is the impact of reduced collisionality on pressure profile peaking [80, 81]. For example, increased density profile peaking would make the bootstrap current profile [82] more peaked and increase  $l_i$ . Assuming density profile peaking in NSTX Upgrade scales similarly to conventional aspect ratio tokamaks, and further assuming the collisionality decreases by a factor of 5 in NSTX Upgrade and the NBI power and temperature double, Equation 3 of Reference [81] can be used to estimate the increment in density peaking factor to be 0.2 to 0.3. Most of this projected increment comes from the collisionality dependence of the density peaking factor since the projected normalized NBI particle source term  $\Gamma_{NBI}^* \leq 0.1$ . Figure 10b shows that the most probable thermal pressure profile peaking factor in NSTX is  $p(0)/\langle p \rangle \approx 1.8$ . If this value increases by 0.3 to 2.1 in NSTX Upgrade, Figure 10c shows that the projected internal inductance from TRANSP simulations increases from 0.5 to 0.6-0.7 essentially independent of plasma scenario and spanning a range of non-inductive current fraction  $f_{NI} = 0.5 - 1$  as shown in Figure 10d. Thus, if the pressure profile peaking factor increases by more than 0.2-0.3 in NSTX Upgrade, the vertical control improvements mentioned above may be required to operate stably with  $\kappa \geq 2.7$ . It is also possible that peaking of the pressure will not increase significantly in NSTX Upgrade, as there is evidence that the temperature profile can broaden with increased toroidal field [7]. Further, the application of lithium surface coatings has also been shown to lead to broadened electron temperature profiles and reduced internal inductance [83].

## 2.2. Upgrade Engineering Design

To summarize the combination of requirements above, the Upgraded NSTX device should: double  $B_T$  at  $R=0.93\text{m}$  from 0.5T to 1T and increase the TF flat-top duration to 6-7s, double  $I_P$  from 1MA to 2MA and provide a 5s flat-top at full current, double the neutral beam injection (NBI) heating power from  $P_{NBI} = 5\text{MW}$  to 10MW and sustain it for 5s, and nearly triple the OH flux from 0.75Wb to 2Wb. Representative waveforms for the NSTX and NSTX Upgrade currents are shown in Figure 11 and illustrate the substantial increase in device performance to be achieved with the Upgrade.

### 2.2.1. New Centerstack

An important feature of the NSTX device design is the ability to remove the center-stack (CS) independent of the vacuum vessel and the external PF and TF magnets. Thus, Upgrade performance requirements can potentially be met by replacing the present CS with a new larger CS thereby providing more cross-sectional area and conductor to carry the TF current and also providing increased OH flux. The increased size of the new CS is shown graphically in Figure 12a by the red outline overdrawn on the present CS. Figure 12b shows the doubling of the TF conductor diameter which



enables the doubling of TF current with 5 times longer pulses. The TF flat-top pulse length of 6.5s at full current is limited by the temperature rise within the coil, and Figure 12c shows the predicted temperature distribution within the conductor at the end of TF flat-top operating at the maximum toroidal field of 1 Tesla [84]. Figure 12c shows that the maximum temperature reaches 117°C without water cooling, and tends to peak near the region where the TF inner conductor interfaces with the flag extension and also on the inner diameter of the flexible joint arch. Both locations are regions of maximum current density. With water cooling, the maximum upper/lower temperatures of the inner TF conductor reach 111/113°C which is within the allowable limits for the epoxy chosen to bond the insulation to the conductor [84]. The outer TF conductors are also water cooled, but only reach approximately 50°C for the same full-current pulse. The flexible joints [85] connecting the inner and outer TF conductors and enabling the vertical growth of the inner TF bundle are cooled between shots by thermal conduction to the inner and outer TF conductors.

The OH coil diameter also nearly doubles in the new CS and can provide up to nearly 4 times higher solenoid flux-swing for sufficiently fast swing, and 3 times higher flux-swing for 5s 2MA flat-top plasmas. Coil self-forces and forces from electromagnetic interactions with other PF coils have been accounted for, and the maximum OH conductor temperature is designed to be limited to 100°C [86]. The water cooling flow-rate will be controlled to limit the thermal stress induced by the water coolant "wave" that propagates through the vertical height of the OH during the post-shot cool-down period. It should be noted that the number of OH coil windings in NSTX Upgrade has been reduced from the originally planned 1016 [86] to 884 to enable inter-shot cool-down times of 15 minutes or less (versus 19 minutes) to increase the number of possible full-performance shots per hour. For reference, the typical inter-shot period on NSTX is 10-12 minutes. As shown in Figure 13, this larger CS incorporates the larger TF and OH while also including three upper and lower divertor PF coils PF1A,B,C (compared to two/one PF coils in the lower/upper divertor of NSTX) and also providing an insulating break for biasing the CS casing relative to the vessel for Coaxial Helicity Injection (CHI) current start-up. This larger outer diameter (OD) CS increases the minimum aspect ratio of fully limited plasmas from  $A = 1.3$  to 1.5. As a result, diverted plasmas will typically have  $A \geq 1.6$ . While this aspect ratio is larger than the present NSTX, it is comparable to the optimal aspect ratio identified in ST-FNSF [3, 4], ST Pilot Plant [87], and ARIES-ST reactor studies [88].

Lastly, another important design feature of the new CS is the relocation of the OH coil current leads from the top to the bottom of the centerstack to eliminate the stress on the leads arising from the vertical thermal expansion of the OH coil. Further, the OH coil lead area has been redesigned to utilize a coaxial current feed (shown in Figure 14)

to minimize the non-axisymmetric fields from, and forces on, the OH coil which play a significant role in generating the  $n=1$  error field in the present NSTX [30].

### 2.2.2. Structural Enhancements

Doubling the TF and plasma current increases the forces on the coil supports and vacuum vessel (VV) up to a factor of 4, and substantial analysis and design has been performed to provide structural reinforcement against these increased loads. A graphical summary of the external structural modifications for NSTX Upgrade is shown in Figure 15. In Figure 15, the PF coils are shown in blue, the outer TF coils are shown in red, and the TF coils are connected mechanically to the vacuum vessel through cylindrical "umbrella" structures (grey) at the top and bottom of the vessel. The NSTX Upgrade structural modifications include a new flexible umbrella upper lid to allow OH/TF vertical thermal expansion while transferring torsional loads of the CS to the outer vessel, stronger connections of the TF coils to the umbrella structure and strengthening of the umbrella legs and feet, new TF support rings and clevises to transfer torsional loads on the TF coils to the vacuum vessel, new and upgraded vertical field coil (PF4 and 5) separator struts to take increased inter-coil forces, improved PF2 and PF3 coil supports, a new pedestal on which the CS is supported, and improved vessel supports.

Particular emphasis has been placed on the increased torsional load applied to the outer TF legs from the Lorentz force of the poloidally directed TF coil current crossed with the radial and vertical field from the PF coils. Evaluation of the three components of the load in cylindrical coordinates finds the radial load is carried by the cylindrical umbrella and the near-midplane TF coil supports, and the vertical load and the out-of-plane (OOP) load are transferred through the umbrella structure producing high stress in the umbrella feet, the arches, and the VV ribs and dome. Analysis based on worst-case poloidal field (PF) currents shows that some structures would be over-stressed with peak stresses  $> 1$  GPa for NSTX Upgrade parameters.

To eliminate such overloading, the load path will be modified in NSTX Upgrade. First, by adding structural support to transfer outer TF coil load to the VV at clevis connections above and below the midplane combined with upgraded clevises, maximum transfer of the OOP loads to the mid-section of the vessel can occur. Figure 16a shows the array of 12 supports above the midplane that will provide this load transfer, and an identical set is also used below the midplane. These connections reduce loads on the umbrella structure at the top and bottom of the vessel, but will increase loads in the mid-section of the vessel. Interferences with auxiliary systems and supports constrain the design options and limit the addition of trusses to help sustain the OOP load. Nevertheless, sufficient space exists to create a much sturdier support ring via

connections between the TF outer coils as indicated by the toroidally continuous circle of new coil clamps shown in Figure 16a. This support ring reduces the pull-out (in-plane) loads, and in combination with the tie-bars, transfers much of the in-plane and OOP load to the VV. The support ring also reduces the pull-out (in-plane) radial load at the umbrella structure. Details of the improved clamps and connections of the TF to the VV are shown in Figure 16b. These structures are effective at reacting loads from PF currents for both up-down symmetric and asymmetric equilibria. It should be noted that up-down asymmetric currents result in a net twist load which requires an attachment to the VV. The tie bars can take the net twist and also provided adequate OOP support for up-down symmetric equilibria.

The second modification to reduce peak stresses at the umbrella structure involves strengthening the umbrella itself. Figure 17a shows the outer TF coils (red) connecting to the upper umbrella structure, and Figure 17b shows the reinforcement strips and bolt enhancements that will strengthen the aluminum block structures that connect the TF coils to the umbrella. Further, Figure 17c shows the arch reinforcement ring that will be added to the umbrella, the new legs that will be installed, and the improved attachments for the umbrella feet.

Of the 96 equilibrium scenarios used for the engineering design of NSTX Upgrade, the two that generate the largest out-of-plane (OOP) forces and torques on the TF outer legs are numbers 34 and 79. These cases correspond to equilibria F (up-down asymmetric) and U (up-down symmetric) in Figure 6 with the OH coil supply current at -24kA, i.e. at the end of the OH coil second swing. In the upper half of the outer TF, the worst-case toroidal forces and torques are 175/180kN and 320/330kN-m for equilibria F/U, respectively. With the redesigned coil support configuration, the maximum predicted coil stress is 103 MPa and the insulation shear stress is within 11 MPa, and both values are within the allowable values. After reinforcement, the umbrella structure has a maximum stress of 130MPa, and the peak umbrella arch stress is 85 MPa compared to 304 MPa prior to reinforcement. The stress in the VV is below 106 MPa (within allowable) and has a safety margin factor of 8.5 for non-linear buckling for scenario 79. The TF support system also maintains the peak stress in the outer TF coil within allowable values for the VV bake-out (150°C). Lastly, with the redesigned coil support configuration, Figure 18 shows the maximum displacement over the entire coil/vessel/umbrella system is limited to 3.1mm. This is more than 8 times smaller than the 27mm maximum displacement that would have been experienced with the original NSTX support system at full NSTX Upgrade parameters.

### 2.2.3. 2nd Neutral Beam Injector

Beyond the new CS and ex-vessel structural enhancements, a 2nd neutral beam from

TFTR has been chosen to provide the factor of 2 increase in auxiliary heating and current drive power for NSTX Upgrade, as this is presently the most mature and capable technology applicable to ST plasma parameters. The performance parameters of the NSTX neutral beams [89] are provided in Figure 19 for reference. Of particular relevance is the decrease in achievable NBI pulse duration (set primarily by the thermal limits of the ion dumps) from 5s to 1.6s as the beamline power is increased 50% from 5MW to 7.5MW. This decrease highlights the importance of the 2nd NBI for providing sufficient heating power for the pulse-lengths expected in the Upgrade. If plasma scenarios with pulse-lengths substantially longer than 5s become accessible in NSTX Upgrade, additional NBI pulse-length enhancements may be possible by using "high-hat" ion dumps with two stacked plates (still inertially cooled) to spread the dumped beam ion footprint as originally proposed for the TPX NBI upgrade [90].

The 2nd NBI of NSTX Upgrade not only serves to increase the auxiliary heating power to access reduced  $\nu^*$ , but also has increased tangency radius of injection  $R_{TAN}$ . As described in more detail in Section 2.3, increased  $R_{TAN}$  is projected to increase the NBI current drive efficiency and also provide for NBI current drive profile control. The layout of the new more tangential 2nd NBI next to the present NBI is shown in Figure 20a. An important aspect of this layout is the sharing of the beam armor [91] by both NBI systems, as this minimizes the in-vessel surface area taken up by NBI. Achieving increased tangency radius of injection also requires a significant modification to the NSTX vacuum vessel with the cutting of a large opening in the vessel wall for the installation of a new NBI port cap as shown in Figure 20b. The NBI port cap required substantial structural analysis and several design iterations to make it compatible with both space constraints and the increased loads on the vessel described in Section 2.2.2. The injection radius of the present NSTX NBI has been left unchanged due to space constraints in the NSTX test cell. The more tangential injection of the 2nd NBI on the horizontal mid-plane on NSTX Upgrade is complementary to the MAST Upgrade [92] approach of adding vertically-shifted co-injection NBI sources [93] to achieve more off-axis current drive. Together, the two upgraded devices will thoroughly test off-axis NBI current drive predictions and will inform the optimal NBI injection geometry for next-step ST devices.

The installation of the 2nd NBI also requires substantial floor space in the NSTX test cell, and a major task of the NSTX upgrade outage involves removing and relocating several diagnostics and associated racks to make room for the 2nd NBI. As shown in Figure 21, once the 2nd NBI is installed next to the present NBI, most of the available floor space within the test cell will be occupied by NSTX Upgrade and NBI systems. It should also be noted that the 2nd NBI to be used on NSTX Upgrade was used during the D-T experiments on TFTR and was contaminated with tritium. The decontamination

of this beam line was successfully completed in 2010 in preparation for usage on NSTX Upgrade, and reassembly of the 2nd NBI was initiated in 2011.

### 2.3. Non-inductive Current Formation and Sustainment

A critical element of ST research in support of steady-state operation is to increase the 65-70% non-inductive fraction sustained in NSTX [50, 63, 51] to full non-inductive sustainment. Future ST-FNSF facilities are projected to rely heavily on NBI current drive (NBICD) to drive as much as 50% of the plasma current with the remainder provided by bootstrap current. NBICD is also presently envisioned to provide the heating and current drive for non-inductive plasma current ramp-up. Reduced collisionality in NSTX Upgrade will help increase the NBI current drive efficiency to increase the non-inductive fraction, but additional current drive is still required. NSTX Upgrade will rely heavily on the 2nd NBI system discussed in Section 2.2.3 (also injecting in the co-plasma-current direction) to increase the externally applied non-inductive current drive. An overview of non-inductive sustainment calculations for NSTX Upgrade is provided in Section 2.3.1, and a comprehensive analysis of NSTX Upgrade equilibrium scenarios using free-boundary TRANSP calculations is provided in Reference [40].

#### 2.3.1. Plasma Sustainment with NBI Heating and Current Drive

The 2nd NBI of NSTX Upgrade not only serves to increase the auxiliary heating power to access reduced  $\nu^*$ , but also has increased tangency radius of injection  $R_{tan}$ . The increased tangency radius of injection increases the NBI current drive efficiency by depositing fast-ions on-average more parallel to the magnetic field since  $v_{||}/v = (R_{TAN}/R)|B_\phi/B|$  [94], but also depends on details of the target plasma and NBI deposition profile. Figure 22 shows TRANSP calculations of the NBI current drive efficiency versus  $R_{TAN}$  for a representative NSTX target plasma with  $A=1.45$ ,  $\kappa = 2.45$ ,  $I_P = 0.82\text{MA}$ ,  $B_T = 0.55\text{T}$ , line-average density  $= 4.4 \times 10^{19}\text{m}^{-3}$ , Greenwald density fraction  $= 0.6$ , line-average  $T_e = 1.2\text{keV}$ , and outboard plasma-limiter gap of 13cm. This reference plasma condition is included in these studies to ensure that the new 2nd NBI will also be effective at heating and driving current for NSTX-like field, current, collisionality, and gap values in support of NSTX Upgrade physics studies that may wish to access plasma parameters similar to those of the original NSTX (except aspect ratio).

Figure 22a shows that the absorbed current drive efficiency  $I_{NBICD}/P_{ABS}$  increases by a factor of 1.65 as the tangency radius is increased from that of the least tangential source ( $R_{TAN} = 50\text{cm}$ ) of the present NBI to the most tangential source ( $R_{TAN} = 130\text{cm}$ ) of the new 2nd NBI. The NBI power loss is also a function of tangency radius, and Figure 22b shows that for small  $R_{TAN}$ , the more perpendicular injection increases

the number of particles that are promptly lost (i.e. bad orbits). Small  $R_{TAN}$  also increases the fraction of particles with orbits that spend time in the gap between the plasma and first-wall and this trend increases charge exchange losses. Figure 22b also shows that large  $R_{TAN}$  can lead to increased power losses due to increased shine-through. This is caused by the decrease in NBI path-length intersecting the plasma when  $R_{TAN}$  is large, and this results in decreased beam ionization and absorption. Thus, while the largest  $R_{TAN}$  has the highest current drive efficiency for power absorbed, the injected power current drive efficiency  $I_{NBICD}/P_{INJ}$  is highest for  $R_{TAN} = 120\text{cm}$  for these equilibrium conditions. Overall, the current drive efficiency for injected power is at least 40% higher for the new 2nd NBI compared to the present NBI.

An additional important capability for optimization of stability and confinement is control of magnetic safety factor profile. Thus, for NBI as the primary external current drive source, variation of the NBICD deposition profile is needed. For the current drive and loss power conditions shown in Figures 22a and b, Figure 22c shows that the NBI current drive profile depends only weakly on  $R_{TAN}$  for the present NBI ( $R_{TAN} = 50, 60, 70\text{cm}$ ). In contrast, for the more tangential injection of the 2nd NBI in the Upgrade,  $R_{TAN} = 110, 120, 130\text{cm}$  can vary the injected NBICD parallel current density from strongly centrally peaked to peaked off-axis, and this capability can potentially be exploited for improved control of the  $q$  profile.

In the NBI current drive analysis shown in Figures 22, 23, and 24, the ion and electron temperature and electron density profiles are simply linearly scaled from the profiles of NSTX shot 116313 which had a high non-inductive current drive fraction of 60 – 70% that was sustained for multiple current redistribution times. This shot was previously investigated using the TSC [95] code to simulate extension of this high non-inductive fraction scenario to a fully non-inductive scenario [96], and the plasma profiles are shown in Reference [96]. This shot was also used for validating the NBI, bootstrap, and ohmic current drive profile models in TRANSP [50] for NSTX conditions. For shot 116313, the profile peaking factors (peak/volume-average) are:  $T_i(0)/\langle T_i \rangle = 1.64$ ,  $T_e(0)/\langle T_e \rangle = 1.66$ ,  $n_e(0)/\langle n_e \rangle = 1.56$ ,  $p_{th}(0)/\langle p_{th} \rangle = 2.15$ ,  $p_{tot}(0)/\langle p_{tot} \rangle = 2.96$ , and the ratio of volume-average  $T_i$  to volume-average  $T_e$  is 1.25. Generally, these peaking factors are somewhat higher than for the TRANSP simulations of NSTX discharges shown in Table 1. The  $Z_{eff}$  profile for shot 116313 is near 2 in the core and edge, is near 1.6 at the mid-radius, and has a volume-average of 1.8. Toroidal rotation is not included in the TRANSP simulations shown in Figures 22, 23, and 24. All TRANSP calculations shown here assume no anomalous diffusion of fast-ions is present, i.e. the slowing-down is classical. Previous NSTX studies have shown that the anomalous fast-ion diffusion can range from being small in the absence of core MHD and Alfvénic instabilities to causing a substantial reduction in fast-ion stored energy and neutron rate and redistributing

the beam-driven current [97, 98, 50, 51]. The effects of anomalous fast-ion diffusion on NSTX Upgrade NBI current drive is discussed in more detail in Reference [40].

It should be noted that the shine-through loss of the largest  $R_{TAN}$  source can be a sensitive function of the line-average density and especially the outboard plasma-limiter gap. For example, Figure 23 shows that for a representative NSTX Upgrade plasma with  $A=1.65$ ,  $\kappa = 2.6$ ,  $I_P = 0.6\text{MA}$ ,  $B_T = 0.9\text{T}$ , line-average density  $= 3.6 \times 10^{19}\text{m}^{-3}$ , Greenwald density fraction  $= 0.6$ , line-average  $T_e = 1.2\text{keV}$ , and reduced outboard plasma-limiter gap of 7.4cm, the  $R_{TAN}=130\text{cm}$  shine-through loss power fraction decreases from 20% to 10% and the injected power CD efficiency becomes the same as the  $R_{TAN}=110$  and 120cm efficiencies. This decrease in shine-through even for lower line-average density implies the decreased outer gap is playing an important role in increasing the absorption efficiency. For these equilibrium conditions, Figure 23b shows that the bad-orbit losses increase to 20 – 25% for the small  $R_{TAN}$  values of present NBI configuration presumably due to lower plasma current and despite the higher toroidal field. Further, the injected power current drive efficiency of the new 2nd NBI becomes a factor of two higher than for the present NBI. Thus, a representative range for the overall increase in current drive efficiency for the new 2nd NBI relative to the present NBI is 1.4 to 2. It is also apparent that the 2nd NBI is much better confined at reduced  $I_P$ , and this improved capability will be important for non-inductive ramp-up studies as described in Section 2.3.7 Additional information on the NSTX Upgrade scenario dependence on outer gap and NBI source can be found in Reference [40].

Next we consider fully non-inductive equilibrium scenarios for NSTX Upgrade with  $A = 1.65\text{-}1.7$ ,  $\kappa = 2.6\text{-}2.7$ , and outer gap  $= 7.5\text{cm}$ . As shown in Figure 24a, using only the existing NBI with the CS upgrade, full-power NBI (7.5MW) + 4MW of high-harmonic fast-wave (HHFW) heating is needed to support 100% non-inductive operation, and the only means of  $q$  control is  $q_{min}$  variation through the plasma density (i.e. CD efficiency). In particular, since the NBI-CD efficiency varies as  $T_e/n_e$ , increased density at fixed confinement multiplier and  $\beta$  quickly reduces the NBI-CD which lowers the total plasma current which increases  $q$  and the bootstrap fraction which in turn elevates  $q_{min}$ . It should be noted that the  $n_e^{0.4}$  dependence of the ITER H-mode confinement scaling tends to increase the projected thermal confinement at higher density which increases the bootstrap current and partially offsets the loss of NBI-CD at higher density. Nevertheless, such scenarios require  $H_{98}=1.2\text{-}1.4$  and would be limited to 1.6s duration by NBI ion dump operating limits as described in Section 2.2.3.  $H_{98}=1.3\text{-}1.7$  has been achieved transiently in NSTX, but sustaining  $H_{98}=1.15\text{-}1.2$  is only now beginning to be achieved with Li conditioning [99] in ELM-free conditions in NSTX with a goal of extending this enhanced confinement to small-ELM regimes. With the addition of the 2nd NBI of the Upgrade, Figure 24b shows that higher NBI power (10MW vs. 7.5MW)

can reduce the required confinement to  $H_{98}=1.2$  for 100% non-inductive scenarios and also enables control of  $q_{min}$  with  $\Delta q_{min} = 0.6$  by varying the NBI source mix at fixed density. Further, scenarios with  $n_e/n_{Greenwald} = 0.7-1$  exist with  $q_{min}$  varying from 1 to above 2 with important implications for stability and transport research. All of the above scenarios operate above the  $n=1$  no-wall stability limit and require stabilization of the resistive wall mode as is common for advanced scenarios on NSTX [28].

Developing a scenario based on simple linear scalings of fixed profile shapes taken from an experiment may be sufficient for computing NBI and bootstrap currents and current-drive fractions, but such scaling can lead to other difficulties in transport analysis and interpretation. In particular, in some high density scenarios, the computed ion thermal diffusivity ( $\chi_i$ ) can become lower than the neoclassical value ( $\chi_{i-nc}$ ) and can even become negative. This typically happens near the plasma edge where the ion-electron collisional heating of electrons is strongest due to the lower plasma temperature near the edge. The simulations shown in Figure 24b all have  $\chi_i/\chi_{i-nc} > 1$ , and only near the edge ( $\rho_{pol} > 0.8$ ) is  $\chi_i/\chi_{i-nc} \approx 1$  for the  $f_{GW} = 0.95$  scenarios. However, for the scenarios using only the existing NBI heating shown in Figure 24a,  $\chi_i/\chi_{i-nc} \approx 1$  for  $f_{GW} \approx 0.8$ , but  $\chi_i$  can become negative for  $f_{GW} \geq 0.85$  for  $\rho_{pol} > 0.7$ .

To avoid unphysical ion thermal diffusivity profiles, and to utilize an ion thermal transport model more directly related to neoclassical transport [13], more recent TRANSP simulations [40] constrain the ion thermal diffusivity to be a multiple of the neoclassical diffusivity thereby removing the possibility of a negative  $\chi_i$ . Such TRANSP calculations have been carried out for 100% non-inductive current drive using all 6 NBI sources at 1MA and 1T and by optimizing the outer gap to optimize the current drive profile. As shown in Figure 25a, 100% non-inductive current drive (indicated by the white line) is possible for a wide range of normalized density values with confinement multiplier  $H_{98} = 1-1.05$  at  $A=1.73$ ,  $\kappa = 2.7$ , and outer gap = 10cm. As shown in Figure 25b,  $q_{min}$  can be varied from values near 1 (indicated by the white line) to above 3 by varying the normalized density. Further, the  $q_{min}$  values can be increased well above 2 by operating at high normalized density with important implications for RWM stability and for avoiding  $m/n = 2/1$  neoclassical tearing modes.

Figure 26 shows several profiles for the  $H_{98} = 1.03$ ,  $f_{GW} = 0.72$  TRANSP equilibrium simulation in Figure 25. This scenario has 100% non-inductive current fraction at  $I_P = 0.975$ MA and has parameters most similar to the NSTX-U 100% NICD scenarios in Table 1. As shown in Figure 26a, the central ion temperature  $T_i(0)$  is projected to be over 2keV and  $T_e(0) = 1.4 - 1.5$ keV. In these simulations, the  $T_e$  and  $n_e$  profiles are scaled from an NSTX plasma (shot 142301) with aspect ratio  $A \geq 1.7$  [41, 40] prototypical of NSTX Upgrade. The impurity species is  $C^{6+}$  and  $Z_{eff}$  is chosen to be a spatially constant value of 2.0. The chosen  $Z_{eff}$  profile together with the  $n_e$  profile



in Figure 26b determine the deuterium density profile  $n_D$ . The  $T_i$  profile is determined by constraining the ion thermal diffusivity profile  $\chi_i$  to be a multiple (factor of 2 in this case) of the TRANSP NCLASS [100] neoclassical thermal diffusivity  $\chi_{i-nc}$  as shown in Figure 26c. The  $T_e$  profile is scaled to match the overall global confinement constraint, in this case  $H_{98} \approx 1$ . As is evident from Figure 26c, the electron thermal diffusivity  $\chi_e$  is comparable to  $\chi_i$  in the edge/pedestal region  $\rho_{pol} \geq 0.9$  but is a factor of  $2 - 10\times$  higher than  $\chi_i$  in the core region consistent with previously reported NSTX thermal diffusivity profile trends [13]. Figure 26d shows the parallel current density profile  $J_{||} \equiv \langle \vec{J} \cdot \vec{B} \rangle / \langle B_\phi R_0 / R \rangle$  including the total (black), NBI current drive (blue), bootstrap current (red), and ohmic/inductive (green) components. Figure 26e shows that this current density profile results in a  $q$  profile with  $q_{min} \approx 1.5$ . The toroidal rotation angular frequency profile used in this simulation is taken from the NSTX experimental profile and is also shown in Figure 26e and has a central maximum value of 17kHz. The rotation scalings discussed in Section 2.1.3 and Table 1 suggest the toroidal rotation could be approximately a factor of two higher in NSTX Upgrade. High rotation values up to 30-40kHz have previously been reported for NSTX [62, 101], and the impact of possible increased toroidal rotation on NSTX Upgrade scenarios is a topic for future research.

### 2.3.2. High Bootstrap Fraction Scenarios

Beyond the potential usage of the ST for an FNSF, an important issue for both the AT and ST as potential Demo candidates is efficient current sustainment - in particular the achievement of scenarios with very high bootstrap fraction. As is well known, high bootstrap fraction combined with high  $\beta$  and confinement can substantially reduce the need for external non-inductive current drive and minimize the cost of electricity in fusion power plants [102, 88, 103]. However, the ability to access and control scenarios with simultaneous high confinement, high  $\beta$ , and high bootstrap fraction remains an important goal in tokamak/ST research. High confinement combined with high bootstrap fraction has been achieved with strongly reversed shear "current hole" scenarios [104] in which an edge transport barrier (H-mode) is combined with an internal transport barrier to achieve  $H_{98} = 1.5 - 2$  including scenarios which do not use the central solenoid [105] and are therefore relevant to STs.

NSTX L-mode plasmas with reversed shear and heated with a combination of NBI and HHFW have produced core electron and ion transport barriers [106] with improved core confinement. However, such scenarios have not yet been combined with H-mode, as inducing H-mode in the presence of an ITB often leads to MHD instabilities (such as double tearing modes) which destroy the core transport barrier. Additional scenario development is needed to achieve combined edge and core transport barriers,

and increasing the safety factor by doubling the toroidal field in NSTX Upgrade could potentially reduce MHD instabilities.

Alternatively, enhanced pedestal confinement scenarios [99] in NSTX have achieved the high confinement ( $H_{98} = 1.7$ ) conducive to high bootstrap fraction, and these scenarios will also be further explored in NSTX-U. Further, it is noted that if the ST-specific confinement scaling predictions are realized at full toroidal field in NSTX-U, this alone may be sufficient to achieve high confinement and bootstrap fraction. In particular, as shown in the right-most orange columns of Table 1, if the NBI power is reduced to 2MW (to minimize NBI-CD while still driving toroidal rotation and  $E \times B$  shear to suppress ion turbulence) and is combined with 2MW of HHFW heating, high bootstrap fractions of 89-97% are projected to be possible for a range of Greenwald fractions = 0.5-1 using this simple 0D analysis. Such scenarios would have high  $H_{98} \approx 2$  and high  $\beta_N > 5$  but low (relative to ST Demo requirements)  $\beta_t \approx 10\%$  due to high  $q^* \approx 7$ . Given that such scenarios are far from those realized thus far on NSTX or MAST, substantial scenario modeling and experimental development will be needed to access very high  $f_{BS}$ . The  $f_{GW} = 0.77 - 1.0$  equilibria of Figure 24a with  $H_{98} = 1.3 - 1.4$  (1.5-1.6 without HHFW),  $I_P = 0.9 - 1\text{MA}$ , and  $f_{BS} = 0.8 - 0.9$  provide example TRANSP calculations of such scenarios. Further, it should be noted that if one assumes an ITER-like confinement scaling and operates with  $H_{98} \approx 1.1$  and  $f_{Greenwald} = 1$ , i.e. in the upper right corner Figure 25b, fully non-inductive scenarios are predicted to be achievable with  $f_{BS} > 75 - 80\%$  [40]. If such scenarios were achieved in NSTX Upgrade, they would provide a good starting point for attempting to extend ST operation to  $f_{BS} = 80 - 95\%$ .

### 2.3.3. High-Harmonic Fast-Wave Heating in NBI H-mode Scenarios

With respect to HHFW heating and current drive in NBI-heated H-mode plasmas, it should be noted that the central electron temperature has been increased by as much as 60% (to  $T_e(0) \approx 1.9\text{keV}$ ) using 1.8MW of HHFW in  $P_{NBI} = 2\text{MW}$  NBI-heated H-mode plasmas [107]. Lithium wall conditioning was an important element in achieving these results by reducing the plasma density in front of the antenna which reduces surface wave excitation losses [107, 108]. Approximately 2/3 of the injected HHFW power was coupled to the core plasma using heating (0- $\pi$ ) phasing of the antenna straps. Thus, coupling 4MW to the plasma core will require operating at an antenna power of 6MW which is near the antenna voltage standoff limits. Operating at high HHFW power also requires a relatively small plasma-antenna gap (3-5cm) to provide sufficient antenna loading, and improved RF limiters will be needed in NSTX Upgrade to dissipate increased limiter heating from higher HHFW and NBI power and increased pulse-length.

While heating an NBI H-mode plasma with HHFW does appear technically feasible,

HHFW current drive is expected to have low efficiency in NSTX Upgrade NBI H-mode plasmas (except possibly close to the magnetic axis) [109]. Specifically, the HHFW current drive efficiency is:  $I_{CD}[kA]/P_{RF}[MW] \approx 1.5 T_e[keV]/n_e[10^{20}m^{-3}]$  obtained from previous NSTX measurements and simulations [110, 109] is relatively low due to strong electron trapping effects and results in small current drive = 2-20kA for 4MW of HHFW heating for the scenarios in Table 1. Absorption of HHFW power by NBI fast-ions [111] further reduces HHFW current drive efficiency, as does the excitation of surface waves with current drive phasing [108]. Thus, it is expected that the only substantial additional bulk current drive in predominantly NBI-heated H-modes in NSTX Upgrade will come from the new 2nd NBI.

#### 2.3.4. Particle Control

As shown in Figures 24 and 25, the electron density is a strong determinant of the expected NBI current drive efficiency, the non-inductive current fraction, and the expected value of minimum q. Thus, density control will be important for optimizing and controlling high non-inductive current-drive fraction scenarios (and other scenarios) in NSTX. Lithium coatings of the internal PFCs have been shown to pump hydrogenic species, improve confinement, and suppress ELMs in NSTX plasmas [112, 83]. Recently, control of the deuterium ion inventory to equivalent Greenwald fraction (ignoring impurities) as low as 0.3 has been achieved and sustained for up to 1.4s (limited by magnet heating) using Li coatings in NSTX. However, with strong lithiumization and in the absence of ELMs, carbon impurity accumulation can occur which increases the total ( $D^+$  and  $C^{6+}$ )  $Z_{eff} \leq 4$  corresponding to a Greenwald fraction of up to 0.8.

The combination of lithium coatings with ELMs triggered by externally applied n=3 non-axisymmetric field pulses [113, 83] has successfully reduced the carbon accumulation and lowered the  $Z_{eff}$  to 3 or below corresponding to a minimum Greenwald fraction of 0.5-0.7. This range of achievable minimum Greenwald fraction is acceptable for optimizing the NBI current drive of NSTX Upgrade scenarios for pulse durations of perhaps 2-3s, but it is unclear if lithiumization combined with triggered ELMs will extrapolate to 5s pulses and higher heating powers of NSTX Upgrade. Measurements of plasma confinement and beta limits and short-pulse assessments of heat flux mitigation techniques could be performed with only 2-3s of particle control duration in NSTX Upgrade. However, if insufficient particle control leads to MHD instabilities and/or density limit disruptions after 2s, several of the scenarios in Table 1 would be adversely affected. In particular, the long-pulse scenario would not exist, the "Max  $I_P$ " scenario would have only 1s of  $I_P$  flat-top and would not achieve current profile equilibration, and the scenarios that assume ST confinement would have current flat-tops of only 1-2 current redistribution times and would not achieve current profile equilibration.

A liquid lithium divertor (LLD) [114, 115, 116, 117] is being tested in NSTX with a goal of assessing the ability of thicker layers of liquid lithium to extend the deuterium pumping duration relative to thin layers of solid lithium, and conceptual designs for divertor cryo-pumping systems will also be pursued for NSTX Upgrade. Such divertor particle pumping systems are not presently included in the scope of the NSTX Upgrade Project and would therefore likely be implemented following completion and initial usage of the new centerstack and second NBI. If particle control is achieved in NSTX Upgrade using lithium coatings, a LLD, paced ELMs, and/or cryo-pumping, improved fueling control will likely be needed. For improved fueling control, supersonic gas injection (SGI) [118] can provide efficient and controllable edge fueling, central fueling with deuterium pellets [119, 120, 121, 122] is an option, and compact toroid (CT) injection has been proposed for NSTX [123] as a means of core particle fueling and momentum injection with application to NSTX Upgrade, ITER, and other next-step facilities.

### *2.3.5. Overview of Non-inductive Current Formation and Ramp-up*

To achieve low aspect ratio and small device size, future ST-FNSF facilities are anticipated to operate without a central solenoid, making non-inductive ramp-up (with reliance on NBI heating and CD) a critical element of ST research. Present NSTX research is pursuing non-inductive formation of plasma current using Coaxial Helicity Injection (CHI) [124] to form a closed-flux plasma of 0.2-0.3MA to be heated and sustained by high-harmonic fast-waves in a high bootstrap-current-fraction H-mode plasma. Promising HHFW heating and current drive results have recently been obtained [108] in low-current ( $I_P = 300\text{kA}$ ) ohmic target plasmas being developed as plasma current ramp-up targets for NBI. In these plasmas, an HHFW-induced H-mode and an electron ITB were achieved simultaneously, and a central electron temperature of 3keV was achieved with 65% non-inductive current drive ( $f_{BS} = 43\%$ ,  $f_{RFCD} = 22\%$ ) with 1.4MW of injected HHFW power. The time evolution and density and temperature profiles for this plasma are shown in Figure 27. These results project to 100% non-inductive current drive at 3-4MW of injected HHFW power and support a major research goal of NSTX Upgrade which is to assess whether plasmas formed with helicity injection (see Section 2.3.6) and heated with HHFW (and possibly ECH/EBW [125, 126]) can form a suitable target for current ramp-up using NBI heating and current drive as described in Section 2.3.7.

### *2.3.6. Coaxial Helicity Injection Plasma Formation*

CHI on NSTX is implemented by injecting current from an external circuit through a plasma arc formed along a combined poloidal and toroidal magnetic field that connects the lower inner and outer divertor plates. NSTX uses the lower divertor plates as

the injector electrodes with the upper divertor plates acting (and referred to) as the absorber. At sufficiently high poloidal CHI injector current, the plasma current self-force accelerates the plasma away from the injector region into the vacuum chamber and toward the absorber region. Figure 28a shows the rapid growth of the CHI plasma emerging from the lower divertor and filling the NSTX vacuum chamber in less than 3ms. As shown in Figure 28b, CHI has been successfully coupled to high-confinement inductively-driven plasmas [127, 128] with an early current savings of 150-200kA relative to OH-only start-up. As shown in Figure 28c, this corresponds to plasma poloidal flux formation by CHI of 50mWb. The plasmas compared in Figure 28 are chosen to have a similar shape and  $l_i$  evolution to illustrate the current and flux savings from CHI.

The initial poloidal field connecting the inner and outer divertor plates in the injector region is produced using the lower divertor coils as shown in Figure 29a. To produce a CHI start-up plasma that is accelerated away from the injector into the main NSTX vacuum chamber, the injector current  $I_{inj}$  must exceed the "bubble burst" threshold current [124]  $I_{bb}$ :

$$I_{inj} \geq I_{bb} = 2\psi_{inj}^2 / (\mu_0^2 d^2 I_{TF}) \quad (1)$$

Here  $\psi_{inj}$  is the poloidal flux at the injector insulating gap,  $I_{TF}$  is the total current in the toroidal field coil, and  $d$  is the width of injector flux footprint on the electrodes. It can also be shown that the toroidal current generated for a given amount of injector current has a limiting value equal to the ratio of the toroidal flux enclosed by the ST limiter boundary  $\Phi_T$  to the injector poloidal flux:

$$I_P / I_{inj} \leq \Phi_T / \psi_{inj} \quad (2)$$

Recent simulations using the TSC code have shown reasonable agreement with these relations and the potential for substantial current generation in NSTX-U [129]. One reason for this can be seen in Figure 29a, which shows the location of the injector coil in relation to the CHI injector gap across which the voltage is applied. This improved current generation potential in NSTX-U is due in part to the improved location of the CHI injector flux coil (lower PF1C coil), which is positioned much closer to the CHI insulating gap. As shown in Figure 29a, the injector coil in NSTX is farther away from the insulating gap, resulting in a 2.5 times smaller flux generated by this coil that connects the inner and outer divertor plates. Quantitatively, the available injector flux in NSTX-U is projected to be approximately 200 mWb compared to less than 80 mWb in NSTX.

In addition to the improved positioning of the lower divertor PF coils in NSTX-U for CHI, Figure 29b shows that the location of the absorber coil (upper PF1C coil) is better positioned in NSTX-U. This coil is used to generate a buffer flux to keep the expanding CHI discharge from contacting the upper absorber gap, as such a condition (known as

an absorber arc) can short-circuit the insulating gap and cause the injected current to flow through this gap instead of through the main plasma. The closer positioning of the PF1C coil to the absorber gap enables the flux generated by this coil to be more efficiently utilized to suppress absorber arcs. Importantly, the kA-turn capability of the absorber coil in NSTX-U is three times that in NSTX (318 kA-turn versus 100 kA-turn in NSTX) and the current slew rate is also substantially higher (40 kA-turn/ms in NSTX-U versus 5 kA-turns/ms in NSTX). The faster slew rates are needed to rapidly turn off the lower divertor PF coils after the CHI plasma formation process is complete and to track the rapid upward motion of the higher- $I_P$  CHI plasma expected in NSTX-U.

Overall, CHI current formation scales favorably with the available injector flux and the enclosed toroidal flux, and CHI is projected to be capable of generating 300-600kA of closed-flux current in NSTX Upgrade by operating at 1T based on scaling the results of Figure 28 and TSC simulations [129]. Using the TSC and NSTX experimental results as a starting point, relatively simple scalings can be used to project to NSTX-U and next-step STs, and the results of such scalings are shown in Table 3. In these scalings it is assumed that the start-up internal inductance  $l_i$  is the same as the NSTX value of 0.35, the flux footprint  $d$  scales as the minor radius  $a$ , and the injector flux  $\psi_{inj}$  scales as  $RI_P$ . Further, it is assumed the injector current  $I_{inj}$  is 1.2 times the bubble burst current  $I_{bb}$  and that the start-up plasma closed poloidal flux  $\psi_p$  achieved is 80% of the injector flux  $\psi_{inj}$ . Lastly, the current multiplication  $I_P/I_{inj}$  is held below the limiting value  $\Phi_T/\psi_{inj}$ . The projected electrode current densities of up to  $63kA/m^2$  in ST-FNSF are significantly lower than those achieved successfully on HIT-II [130] [ $300kA/m^2$ ] which appears favorable, but the optimal electrode design and the required CHI voltage for FNSF/Pilot applications require additional research and development. In summary, these CHI scalings project to 0.4MA of start-up current in NSTX-U, 2MA in ST-FNSF, and 3.6MA in an ST Pilot Plant, and these values correspond to 20% of the nominal maximum plasma current for each device.

As described in Section 2.3.7, 0.4MA is sufficient plasma current in NSTX-U to confine the fast-ions of the new 2nd NBI. However, additional heating of the CHI target plasma by HHFW may be needed to increase the electron temperature to increase the  $L/R$  decay time of the plasma current [129] to provide sufficient time for the NBI ions to slow down to heat the plasma and to drive NBI current. Simulations are underway to assess the needed auxiliary electron heating for CHI-produced plasmas, and studies of this issue will be pursued in NSTX Upgrade to inform the requirements for the heating and non-inductive ramp-up of CHI-produced plasmas in next-step STs.

Lastly, it should be noted that initial CHI experiments in NSTX focused on driving steady-state current [131, 132], but with this technique there was little evidence for the formation of closed poloidal flux, the DC power supply power required was large

( $20\text{kA} \times 500\text{V} = 10\text{MW}$  for  $200\text{kA}$  of plasma current), and coupling to ohmic or NBI-heated plasmas was difficult due to absorber arcs. Further, adding steady-state CHI current drive to other forms of current drive (such as to an inductively-driven LSN plasma) did not drive significant additional current. This result may have been related to the need for (and apparent lack of)  $n = 1$  MHD-driven flux-surface opening at the plasma boundary to achieve 3D-reconnection-driven CHI current drive [133, 134]. In contrast, the transient CHI plasma formation described here involves primarily inductive current drive and axisymmetric reconnection driven by the decay of the open-field-line injector current and the PF coil current variation as simulated with the axisymmetric TSC code. Transient CHI has exhibited formation of closed poloidal flux plasma current [135] with good coupling to ohmic current drive and NBI H-mode, and extrapolates favorably to next-step STs. For these reasons, it is likely that NSTX Upgrade will continue to focus primarily on transient/axisymmetric CHI plasma current formation rather than steady-state/3D-reconnection-driven CHI current sustainment.

### 2.3.7. Non-inductive Current Ramp-up

Moving to the consideration of non-inductive current ramp-up for NSTX-U, a very important benefit of more tangential NBI is the ability to heat and drive current in low current target plasmas. As shown in Figure 30a, the injected current drive efficiency of the more tangential 2nd NBI ( $60 - 65\text{kA/MW}$ ) is a factor of  $3 - 4$  times higher than the present NBI ( $15 - 20\text{kA/MA}$ ) for low  $I_p = 0.4\text{MA}$  target plasmas. As shown in Figure 30b, this is because of the much lower bad-orbit losses (due to more parallel injection) of the new NBI sources at low plasma current. As is also evident from Figure 30a and b, the tangency radii of the 2nd NBI are close to the optimal values (by design) for maximizing the NBICD by minimizing the power loss at low plasma current. This prediction of good absorption and current drive efficiency at low  $I_p$  opens the possibility of non-inductive ramp-up studies in NSTX Upgrade to prototype non-solenoidal ramp-up in an ST-FNSF.

Free-boundary TSC simulations have been carried out to further assess solenoid-free current-ramp for NSTX Upgrade using early HHFW heating to pre-heat a low- $I_p$  target to high non-inductive fraction followed by NBI heating and current drive. The TSC simulations of non-solenoidal ramp-up described here will be coupled to TSC simulations of CHI start-up [129] in future work. Figure 31a shows the simulated evolution of the auxiliary heating from HHFW (green) and NBI (red) used in TSC. Figure 31b shows the plasma current components in these simulations. TSC does not explicitly deal with the fast-ion component of the stored energy, and uses fixed profile shapes and efficiencies for the NBI CD chosen to be similar to those shown in Figure 22. In these TSC calculations, a limited,  $I_p = 150\text{kA}$ , low density L-mode target plasma with  $T_e(0) = 0.5\text{keV}$  is provided as an initial condition to simulate the conditions of an HHFW-heated CHI plasma that

remains to be developed in future experiments on NSTX Upgrade. As described in Section 2.3.6, closed-flux plasma currents of 150-200kA have already been produced with CHI start-up, HHFW has successfully heated inductive plasmas initiated with CHI [107], and HHFW has heated 300kA ohmic target plasmas to 3keV as shown in Figure 27.

Figure 31a shows the HHFW power is ramped linearly to 4MW over 200ms, and this increases the projected bootstrap current to 300-350kA as shown in Figure 31b and consistent with extrapolations from the data in Figure 27. For times after 0.2s, the bootstrap + NBI currents exceed the equilibrium plasma current, and the plasma current is over-driven. In the over-driven state, a negative loop voltage (back-EMF) occurs inside the plasma in response to the non-inductive current over-drive, and the net current (i.e. the plasma current) increases on a slower global inductive time-scale.

Once the plasma current exceeds 300-350kA, the new 2nd NBI will be absorbed at the 70-80% level, and the simulated NBI power is increased in three 1.65MW increments to 5MW as shown in Figure 31b. This further increases the bootstrap current and drives 250-300kA of NBI current which increases the plasma current to 500-550kA. At this time ( $t=0.85s$ ), the HHFW is turned off and replaced with an additional 5MW of NBI power simulating usage of the original NSTX NBI. This increase in NBI power increases the bootstrap + NBI non-inductive current drive to 1.2-1.3MA, and this current drive decreases to 1-1.1MA by  $t=1.5s$  as the density increases for fixed Greenwald fraction and increasing plasma current. As shown in Figure 31b, the bootstrap and NBI currents reach steady values of 0.6MA and 0.4MA respectively for  $t > 2.5s$ , and the plasma current asymptotically approaches 1MA by  $t=4.5s$ . During this time, the internal inductance slowly rises from 0.35 to 0.6 by  $t=4.9s$  as shown in Figure 31c, and the shot-average  $\kappa \approx 3$  (not shown).

The stability, confinement, and temperature information for the TSC simulations in Figure 31 are shown in Figure 32. Figure 32a shows the thermal  $\beta_N$  remains below 2.5 for the entire duration of the simulation. Figure 32b shows the normalized density value increases to 0.65 by  $t=0.2s$ , decreases, and then is nearly constant at 0.5 after  $t=1s$ . Based on the scalings of the fast-ion stored energy and results from Table 1, the fast-ion stored energy fraction is approximately 50% for such plasmas, so the estimated total  $\beta_N \approx 5$ . The Coppi-Tang L-mode transport model [136] is used in the initial L-mode phase, and this transport model is augmented with a reduced thermal diffusivity in the pedestal region to simulate an H-mode and give the profile shape observed in the high bootstrap-fraction phase of the H-mode. In the simulations, the H-mode phase begins at  $t=0.12s$ , and in both the L and H-mode phases, the density profile shape is prescribed and has a peaking factor of approximately 1.1 (see Figure 33). The  $Z_{eff}$  value of 3.5 is also prescribed and is constant in time and space.



Using these assumptions, Figure 32c shows the  $H_{98}$  evolution. While there are some oscillations in the  $H_{98}$  value between 0.7 and 1.3 in the first 1s of the simulation, the  $H_{98}$  has a slowly varying value decreasing from 1 to 0.85 after  $t=1s$ , and on-average is at or below 1. The resulting central and pedestal temperatures are shown in Figures 32d and 32e, and have values of 1.7keV and 0.4keV, respectively, after  $t=1s$ . As shown in Figures 32 and 33,  $T_e$  is significantly higher than  $T_i$  during the HHFW heating phase, and the temperatures become similar during the NBI heating phase is also observed in NSTX experiments. One important difference between the NSTX experiments and the TSC simulations is that in the experiments,  $\chi_e$  is generally greater than  $\chi_i$ , and  $\chi_i$  is approximately neoclassical, whereas the Coppi-Tang model (with H-mode added) predicts  $\chi_i > \chi_e$  as shown in Figure 33. The impact of the transport model on the TSC ramp-up simulations is a topic for future research. Lastly, Figure 33 also shows the  $q$  profiles early and late in the non-inductive ramp-up simulations. The initial  $q$  profile has weakly reversed shear in the plasma core, and the later  $q$  profile is monotonic with weak shear in the plasma core. At  $t = 4.5s$ , the central  $q$  has a value of 1.3-1.4 and is slowly decreasing. Based on these simulations, by operating at 1T and combining CHI current formation of 300-400kA with NBI current ramp-up using the 2nd more tangential NBI, NSTX Upgrade appears well equipped to study non-inductive current formation and ramp-up as needed for an ST-FNSF.

## 2.4. Disruption Forces

### 2.4.1. Overview

Just as the equilibrium electromagnetic forces on the structure will increase by up to a factor of 4 in NSTX Upgrade, the forces during plasma disruptions are expected to increase by a similar factor. The projections for NSTX Upgrade rely heavily on the previous characterization of vertical displacement events (VDEs) and plasma current quenches (CQs) from NSTX [137]. Based on NSTX data and scalings, 3D electromagnetic models of the vacuum vessel and passive conducting structures of NSTX have been utilized to predict the induced currents, fields, and forces for 2MA, 1T plasma disruptions in NSTX Upgrade [138].

The disruption modeling utilizes a range of disruption scenarios and time-scales based on NSTX data and experience. Table 4 summarizes the 5 types of disruption categories analyzed, namely: radially centered (black/grey), inward drift to centerstack (purple), VDE to inboard divertor (green), VDE to middle/outer divertor (blue), and VDE to outboard to passive plates (yellow). Each of these disruption categories has additional variations of VDE drift time, current quench time, and halo current magnitude to span the range of typical NSTX disruption characteristics but scaled and analyzed for 2MA disruptions in NSTX Upgrade. The circles in Figure 34a indicate

the positions and sizes of the disrupting plasma current channels for each of the 5 disruption categories of Table 4. The plasma current density is assumed to be spatially uniform inside each circle, and the total current in each circle is varied linearly in time depending on the details of each scenario. Circles that represent current channels that have drifted to the location shown have square symbols at the center of each circle and two square symbols on the limiter boundary. The symbols on the limiter boundary indicate the assumed locations for halo current strikes for halo currents driven during the plasma current quench. Figure 34b shows the time evolution of disrupting plasma currents for a representative VDE to the inboard divertor with medium quench rate and including halo currents. In this model, the vertically centered current (black circle in Figure 34a) is ramped from 2MA to 0MA (blue curve in Figure 34b) while the vertically displaced current (green circle in Figure 34a) is ramped from 0MA to 2MA (red curve in Figure 34b) during the same interval. Ramping the currents in this way simulates the downward vertical motion of plasma over a typical drift period of 10ms. After the drift phase, the vertically displaced current is ramped from 2MA to 0MA for a range of current quench durations, in this case 4ms for the scenario shown. During the current quench, the halo current is typically small at the beginning of the quench, reaches a maximum value approximately half way through the quench, and becomes small again near the end of the quench [139]. This evolution is modeled as a triangular current waveform as shown by the green curve in Figure 34b, and the maximum value of the halo current is set by the assumed halo current fraction relative to the pre-quench current. In this case the halo current fraction  $f_{halo} = 35\%$ , so the maximum  $I_{halo} = 0.7\text{MA}$ .

For each of the NSTX Upgrade structures analyzed for disruption loads, the plasma-induced inductively-driven voltages from inward or vertical plasma motion and from the current quench are treated as axisymmetric, i.e. any 3D distortions of the plasma current channel are ignored. However, these 2D applied voltages can induce 3D currents in the conducting structures including the passive conducting plates, divertor plates, vacuum vessel, and center-stack casing. Additionally, halo currents are modeled as a current source with the current entry and exit points as shown in Figure 34a with a prescribed toroidal peaking factor of 2 and halo current fractions chosen based on NSTX data. Specifically,  $f_{halo} = 0.2$  for inboard/CS disruptions and 0.35 for VDE disruptions. This product of peaking factor and  $f_{halo}$  is consistent with the upper-bound observed in available NSTX data.

The combined currents from plasma motion, current quench, and halo currents are then used to compute the total currents and forces on the conducting structures, and the NSTX Upgrade components are then designed/modified (if needed) to withstand these loads. Overall, the disruption analysis indicates that forces on the vessel are generally reduced by shielding from the passive conducting plates, and that the Lorentz

forces on the passive plates from the quenching of a VDE displaced plasma sitting near the plates dominates over halo current effects. Further, the centerstack casing and divertor conducting structures are sufficiently strong to withstand axisymmetric loads from plasma motion and current quench, but halo currents in the centerstack introduce lateral forces and displacements that must be supported. Additional details for these most important disruption effects are provided below, i.e. the forces on the passive plates from VDE drift and current quench and the effects of halo currents on the centerstack casing.

#### *2.4.2. VDE and Current-quench Analysis for Passive Plates*

As described above, an important consideration for NSTX Upgrade disruption VDE motion and current quench is the stress applied to the passive plates. Of particular concern is the possibility of radial plate displacements and permanent deformation (and possibly tile cracking) caused by Lorentz forces resulting from toroidal currents circulating in the plate crossed with the (coil plus plasma) poloidal magnetic field. Since the passive plates play an important role in vertical stability and resistive wall mode stabilization in NSTX and NSTX Upgrade, using higher strength but more resistive plate material (such as stainless steel) is likely not an acceptable option.

Using the simplified plasma vertical displacement model for NSTX Upgrade [138] from Table 4 and Figure 34, Figure 35a shows the lower passive plate current density induced by the downward vertical drift of a 2MA plasma with a drift duration of 10ms. These simulations using Opera and ANSYS analysis software find that VDE drift durations in this range maximize the induced circulating currents and radial forces on the passive plates. Figure 35b shows that the peak plate deflection is approximately 1mm as indicated by the orange and red contours near the top and bottom of the passive plate at the plate toroidal mid-point between the plate supports. The corresponding peak membrane plus bending stress is 60MPa which is a factor of 3 below the yield stress. This stress level found at the mid-point between the plate supports is acceptable for NSTX Upgrade. However, the stresses near the bolt heads attaching the plates to the supports are above allowable limits, and at a minimum, enhancements such as higher-strength bolts and/or larger bolt-head slots and washers will be required to withstand the increased disruption loads of NSTX Upgrade.

If plate attachment enhancements were found to be insufficient or infeasible, or if it is desired in the future to increase the maximum plasma current to above 2MA in NSTX Upgrade, one possible means of reducing the peak stress and radial displacement during disruptions is to use thicker passive plates. For fixed applied load, the plate displacement scales as the inverse of the thickness cubed, so doubling the CuCrZr plate thickness from 0.5 inches to 1 inch could substantially reduce the plate deflection under

disruption loads. However, the increased conductance of the thicker plate could increase the induced current, which could reduce the effectiveness of thicker plates, and would also increase the penetration time of fields normal to the passive plates.

In addition to the 3D modeling, the LRDFIT [140] axisymmetric-equivalent circuit model of the coils and passive conducting regions has been developed, benchmarked, and extensively used for NSTX and is used here to assess the impact of thicker plates. Figure 36 shows the LRDFIT-reconstructed plasma and plate current evolution for a representative VDE disruption in NSTX. As seen in Figure 36a for a downward VDE, the chosen plasma drifts from nearly vertically centered to being limited on the lower divertor plate in 5-10ms which is comparable to the drift duration of the simulated case of Figure 35. As shown in Figure 36b, during this drift phase, the plasma cross-section is reduced while the plasma current is maintained. As is evident from Figures 36c and d, the net toroidal plate current induced by the plasma motion is negative as the plate currents act to oppose the downward vertical plasma motion. Then, as the current quench occurs over the subsequent 2-3ms, the net toroidal plate current induced by the quench is reversed and becomes positive in response to the loss of positive plasma current and poloidal magnetic energy.

An important aspect of the NSTX passive structure design is that the stainless steel supports connecting the plates to the vessel wall are several orders of magnitude more resistive than the CuCrZr passive plates, and therefore the net toroidal current is effectively unchanged by increasing the plate thickness. For this reason, Figures 36c and d only plot the net toroidal current for the present 0.5in thick passive plates, since the currents are nearly identical for the two plate thicknesses. In contrast, the circulating current magnitudes do increase with plate thickness since the plate resistance is reduced. The maximum circulating currents in Figure 36c and d are approximately 1.5 times higher for the 1.0 inch thick plates versus the present 0.5 inch plates. Also, after the end of the CQ, the circulating currents in the thicker plates are approximately a factor of 2 times higher and decay away more slowly due to the lower plate resistance and longer L/R time. It is noted however that these increased currents occur after the CQ, so there is little impact of these currents on the plasma current flat-top phase. Further, modeling of the plasma current ramp-up finds that these currents are sufficiently small that they would not significantly impact normal plasma operations.

In the analysis described above and shown in Figures 36 and 37, the circulating current is defined as  $I_{circ} = \frac{1}{2} \sum_j |I_j - I_{avg}|$  where  $I_j$  is the toroidal current in conducting element  $i$  of a conducting region, each conducting element cross-sectional area is identical in a given region, and  $I_{avg}$  is the average value of  $I_j$ . Thus, if the current density in a region is constant,  $I_j$  will be , and  $I_{circ} = 0$ . Correspondingly, if the net toroidal current is zero,  $I_{avg} = 0$ , and  $I_{circ}$  is equivalent to the total positive toroidal current flowing in

the region.

To further analyze the distribution of current in the passive plates, Figure 37 plots the plate toroidal current density for the shot in Figure 36 at  $t=403\text{ms}$  at the time of peak net toroidal current and Lorentz pressure which is just after the time of peak circulating current magnitude. As shown in Figures 37a and b the maximum current density occurs near the top end of each plate where the net toroidal and circulating components are additive in the positive (co-plasma current) direction, while the negative current density occurs on the bottom of each plate with a magnitude typically less than the peak positive value. At this time during the disruption evolution, Figures 37a and b show that some of the negative current density is carried on the back each plate, and similar skin effects are observed in the Opera electromagnetic simulations of Figure 35a. These results highlight the importance of using models that include finite conductor thickness to accurately assess VDE induced currents in passive conducting structures, in particular for the fastest disruptions with the shallowest skin-depths. Further, Figures 37b shows that the peak positive current density of the thicker plate is 15-22% lower than for the thinner plate. This reduction likely contributes to the peak circulating current magnitude in the thicker plate being less than a factor of two higher than in the thinner plate.

The peak plate toroidal current density during the disruption evolution of Figure 36 is  $\approx 33\text{MA/m}^2$  which scaled (by a factor of 1.6) to the worst-case net toroidal current for 0.7MA NSTX plasmas [137] and then scaled (by a factor of 3) to 2MA plasmas projects to  $160\text{MA/m}^2$  in NSTX Upgrade. This value is in good quantitative agreement with 3D predictions of the peak plate current density of  $120\text{-}160\text{MA/m}^2$  for the simulated plasma vertical drift scenario shown in Figure 35a. This analysis indicates that a doubling of plate thickness would result in an increase in plate circulating current by a factor of 1.5-2 and result in an estimated net 4-5 fold reduction in plate displacement, i.e. plate displacement comparable to present NSTX values and therefore capable of handling 2MA disruptions with an expectation of no plate damage over the lifetime of the Upgrade.

In summary, the passive plate analysis indicates that higher-strength bolts and larger bolt-head slots and washers can withstand the increased loading of NSTX Upgrade 2MA disruptions, and this remains true when the effects of halo currents are also included. Another option is to use thicker passive plate material to reduce plate deflection, and this may be required if operation at higher plasma current ( $> 2\text{MA}$ ) is to be pursued in NSTX Upgrade. However, the fabrication of new passive plates is of higher cost than modifying the existing plates, and would also require modifications to the PFCs attached to the existing passive plates (or possibly new PFCs). Since modifying the existing passive plates appears sufficient to withstand 2MA disruptions

in NSTX Upgrade, the present plan is to enhance the plate attachments rather than fabricate new thicker plates.

### 2.4.3. Halo Current Analysis for the Centerstack Casing

Structural analysis of the centerstack casing indicates that any induced currents from drift and/or current quench induce primarily compressive or hoop stresses that are well below structural limits. However, the non-axisymmetry of halo currents can potentially induce net lateral forces on the centerstack that must be countered through the supports attaching the centerstack to the test-cell floor at the bottom of the machine and by the bellows (or other structure) at the top of the centerstack. In particular, it is expected that such loads will be highest shortly after a halo current strike (i.e. with the inductive current density distribution) before the halo currents have time to redistribute resistively through the casing.

Vertically centered disruptions in NSTX are most commonly inboard-limited on the centerstack as a result of some event that causes a rapid loss of some fraction of the plasma current or  $\beta$  such that the radial position control cannot respond sufficiently fast, and the applied vertical field pushes the plasma onto the centerstack. If the plasma is pushed sufficiently hard against the centerstack, it also shrinks, increases in aspect ratio, and becomes more circular. The simplified model of this process is represented by category 2 disruptions in Table 4 and by the translation from the black to purple plasma boundary and associated current shown in Figure 34a. For this vertically-centered inboard-limited quenching plasma model, the halo current strike locations are shown by the purple squares in Figure 34a at  $Z = \pm 0.6m$  on the CS limiter boundary.

Figure 38a shows the radial current vectors of the injected current used to simulate the entry and exit of the halo current strike with a toroidal peaking factor of 2 as described in Section 2.4.1. For the purpose of identifying the characteristic time-scales of the CS halo current evolution, Figures 38b-d show the response to a step increase of the halo current from 0kA to a constant 400kA at  $t=0ms$ . Figure 38b shows the current distribution along the CS casing immediately after the model halo current strike and represents the inductive response. Figure 38c shows the current distribution along the CS casing 10ms after the halo current strike and represents the resistive response since the current in the casing has stopped evolving and is resistively distributed. Figure 38d shows the time evolution of the maximum current density ( $J_{max}$ ) and minimum current density ( $J_{min}$ ) at the vertical mid-plane. Both the maximum and minimum  $J$  can be well fit by an exponential function that decays to the resistive value with a 1.3ms time-constant, and these simulations illustrate that the current at the midplane relaxes to the resistive distribution with significantly reduced toroidal peaking in approximately 4ms.

As discussed in Section 2.4.1, rather than having a step-wise increase, the halo current begins increasing after the beginning of the current quench, typically reaches maximum value roughly half-way through the current quench, and then decreases to a small value near the end of the quench. Figure 39 shows the calculated net force on the CS for fast, medium, and slow current quenches and the associated halo currents. As is evident from the figure, the fastest quenches have the highest forces, and is due to the fastest scenario having a quench time-scale (1ms) faster than the time-scale for resistive redistribution (1.3ms) of current through the CS casing. This results in increased toroidal peaking of the CS halo current which increases the lateral forces. The pedestal that supports the CS casing and other CS components is designed to withstand these lateral loads. However, the stresses and displacements (0.5-1mm) of the bellows on the top of the machine are sufficiently large that a set of shims will be required to be installed to restrain the CS lateral motion while accommodating the vertical thermal expansion of the CS.

### 2.5. Resistive Wall Mode Stability

The ability to withstand disruptions of the highest performance plasmas of the Upgrade maintains a vital capability, namely the ability to access and study high beta plasmas at the highest possible plasma temperature and lowest collisionality without risking machine integrity. As described in Section 2.2.2, several structure enhancements are included of the Upgrade design to support high  $\beta$  operation at full field and current. As described in Section 2.2.3, the 2nd NBI will introduce another large vessel penetration as shown in Figure 20b. Since this penetration will no longer have a metal port cover, the area of the conducting wall will be reduced, and this could adversely impact resistive wall mode (RWM) stability [28] during operation above the no-wall stability limit. However, in NSTX, by design, the CuCrZr passive conducting plates provide much of the stabilization of the RWM. To assess the impact of the 2nd NBI port, the VALEN code [141] has been utilized to analyze n=1 RWM stability for NSTX Upgrade. Figure 40a shows the VALEN model for the passive conducting structure of the Upgrade including both the present and 2nd NBI ports. Figure 40b shows the calculated n=1 RWM growth rates as a function of  $\beta_N$  and number of NBI ports for a representative 2MA equilibrium (equilibrium "R" in Figure 6) with  $A=1.7$ ,  $\kappa=2.6$ ,  $\delta = 0.6$ ,  $l_i=0.6$ , and  $q_{min}=1.9$ . As is evident from Figure 40b, the addition of the 2nd NBI results in only a small  $\beta_N$  decrement of  $\Delta\beta_N = -0.07$  from 5.79 to 5.72 indicating that the 2nd NBI port will have negligible impact on RWM stability limits in NSTX Upgrade.

The n=1 kink with-wall stability limit shown in Figure 40b is for an equilibrium using scaled pressure and parallel current density profiles taken from an MHD-stable NSTX experimental plasma (shot 1163136) operating at  $\beta_N = 5.5$  above the no-wall limit

and near the with-wall limit [50]. In using these profiles from NSTX for NSTX Upgrade free-boundary equilibrium calculations, the profiles have not been further optimized to increase stability limits. It should be noted that the NSTX Upgrade with-wall limit shown in Figure 40b extrapolates to  $\beta_N \approx 5.9$  in the absence of NBI port penetrations. This  $\beta_N$  value is approximately 15% lower than computed in the original NSTX RWM control system design using VALEN [142] (also ignoring port penetrations) for lower aspect ratio NSTX plasmas. Previous numerical studies have shown that both no-wall and with-wall stability limits are projected to decrease 10-20% as the aspect ratio is increased from  $A=1.45$  to  $1.7$  [79, 37]. Thus, the decrease in kink stability limits from NSTX to NSTX Upgrade can be attributed in large part to increased aspect ratio.

## 2.6. Divertor Power Handling

### 2.6.1. Overview

While the compactness of the ST is beneficial for achieving high neutron wall loading for FNS, the ST divertor heat fluxes can also be high and challenge PFC power handling capabilities. The width of the heat-flux profile in the SOL is a critical parameter in projecting the peak divertor heat flux, since the peak heat flux varies inversely with this width. Multi-machine databases and scalings exhibit a wide variation in predicted outboard midplane SOL heat flux width  $\lambda_q$  and this variation represents a substantial uncertainty in projecting to future devices including ITER [143]. Recent dedicated multi-machine studies in the U.S. [144, 145, 146] have explored the  $\lambda_q$  scaling further and find a strong inverse dependence on plasma current but a weak dependence on magnetic field and power into the SOL. Using this mid-plane heat-flux width parameter, the peak heat flux to the divertor target plate can be derived from power conservation and can be expressed as [147]:

$$Q_{out}^{peak} = \frac{P_{heat}^{SOL}(1 - f_{rad})f_{div} \sin(\theta_{plate})}{2\pi R_{strike} f_{exp} \lambda_q} \quad (3)$$

where  $P_{heat}^{SOL}$  is the heating power to the SOL in the absence of radiative losses,  $f_{rad}$  is the assumed fraction of radiation,  $f_{div}$  is the fraction of SOL power to divertor leg in question,  $\theta_{plate}$  is the poloidal angle of inclination between the divertor plate and divertor magnetic field lines,  $R_{strike}$  is the major radius of the divertor strike-point, and  $f_{exp}$  is the poloidal flux expansion  $= |\nabla\psi|_{midplane}/|\nabla\psi|_{strike}$ .

Of particular importance for NSTX Upgrade are high current (2MA) plasmas which are projected to have SOL heat-flux widths as narrow as 3mm if the  $\lambda_q \propto I_P^{-1.6}$  scaling observed in NSTX is also observed in NSTX Upgrade. As shown in Figure 41, the peak heat flux must be limited to 10MW/m<sup>2</sup> to enable 5s operation with the inertially/radiatively cooled ATJ graphite PFCs planned for the Upgrade. Recent assessments of the divertor heat flux scaling in NSTX project to peak divertor heat fluxes



over 20MW/m<sup>2</sup> in the Upgrade even assuming high poloidal flux expansions of 30 [146]. As indicated in Figure 41, utilizing upper/lower power-splitting (i.e.  $f_{div} = 0.5$ ) but not accounting for any radiation/detachment (i.e.  $f_{rad} = 0.0$ ), divertor plate inclination (i.e.  $\theta_{plate} = 90^\circ$ ), or strike-point sweeping (i.e.  $R_{strike}$  is held constant at 0.5m), poloidal flux expansions of 60 are required to achieve peak heat-flux near 10MW/m<sup>2</sup> for  $P_{heat} = 12$ MW in 2MA plasmas. Increased radiation, inclination, or sweeping could reduce the required flux expansion or increase the allowable power or pulse-length. Also, the  $\lambda_q$  scaling with plasma current is closer to  $1/I_P$  in Alcator C-Mod [144] and DIII-D [145], so if a similar scaling was observed in NSTX Upgrade at high  $I_P$ , this would reduce the projected peak heat flux by a factor of 1.5 for 2MA plasmas.

It is important to note that the analysis here focuses only on the outboard divertor leg, since previous NSTX experiments with LSN plasmas find an outboard to inboard power split ratio of approximately 3:1 [148] which is higher than observed at conventional aspect ratio (1.3:1) [149]. Further, measurements at both conventional [149] and low aspect ratio [150, 148, 151] indicate that the ratio of outboard to inboard peak heat flux is typically 3:1 to 4:1 for LSN discharges and up to 9:1 for DND low-A discharges [150, 151]. The low inboard peak heat flux in the NSTX is attributed to the inboard divertor leg typically being detached [152] while the outer leg can be either attached or (partially) detached [153, 154].

Retaining the divertor assumptions described above, i.e.  $f_{div} = 0.5$ ,  $f_{rad} = 0.0$ ,  $\theta_{plate} = 90^\circ$ ,  $R_{strike} = 0.5$ m, and  $\lambda_q = 0.9\text{cm}/I_P^{1.6}[MA]$ , Table 1 shows the projected peak heat flux and pulse duration allowed before reaching a divertor graphite PFC surface temperature of 1200°C assuming that the total heating power is applied during the entire discharge (i.e. ramp-up and flat-top). This surface temperature limit is consistent with avoiding/minimizing self-sputtering and radiation-enhanced sublimation [155] for an estimated typical separatrix electron temperature  $T_{e-sep}$  of 85eV in NSTX Upgrade assuming the power into the SOL is increased up to a factor of 3 (6MW to 19MW), assuming  $T_{e-sep} \propto P_{SOL}^{2/7}$  [147], and that the average  $T_{e-sep}$  in NSTX is 60eV [156, 153]. As is evident from Table 1, the 100% non-inductive, long-pulse, and high  $f_{BS}$  scenarios operating near 1MA are projected to remain well below 1200°C surface temperature using a flux expansion of 22 typical of high-triangularity double-null plasmas. In contrast, the max- $I_P = 2MA$  scenarios require high flux expansions of 40-60 to achieve the respective scenario pulse-length goals while staying at or below the PFC surface temperature limit if no other heat flux mitigation techniques are utilized. At the highest heating powers approaching 20MW expected to be achievable in NSTX Upgrade (red columns in Table 1), the pulse duration (ramp-up + flat-top) at full power could be as short as 1.3s even if high flux expansion of 62 is utilized. Pulse durations much longer than this are not feasible for this scenario in any case, since as shown in

Figure 19, the NBI pulse duration for 15MW total NBI power will be limited to 1.6s.

Another important divertor issue is the effect of transient heat loads from ELMs [157, 158, 159, 160, 161, 143] and disruptions [162, 163, 164, 165, 166]. Recent high-speed IR camera measurements in NSTX during Type-III ELM activity [167] in  $I_P = 0.8\text{MA}$ ,  $P_{NBI}=4\text{MW}$  plasmas find peak heat flux values can transiently increase up to an order of magnitude. In these discharges, a low elongation  $\kappa = 1.8 - 2$  shape with large strike-point radius  $R_{strike} = 0.7 - 0.8\text{m}$  and low flux expansion  $= 2 - 6$  was used to increase the peak heat flux to enable time-resolved measurements (0.16 – 0.63 ms time resolution) of divertor surface temperature and inferred heat-flux during and between individual ELMs. During individual ELMs, peak heat flux values of 40 – 70 MW/m<sup>2</sup>, e-folding lengths of 3 – 4cm, and time-scale of 0.6 ms were observed compared with 4 – 6 MW/m<sup>2</sup> peak heat flux and 1 – 1.5 cm e-folding length for the inter-ELM period. The ELM energy loss from the pedestal region corresponds to 3%–5% of the total stored energy ( $W_{TOT} = 120\text{kJ}$ ) and causes divertor surface temperature increases of 50 – 150°C near the outer strike-point. Since the peak inter-ELM heat flux could increase as much as a factor of 5 – 10 at higher  $I_P$  and heating power in NSTX Upgrade, and since the plasma stored energy is anticipated to increase to the  $MJ$  range, an increase in the flux expansion by an order of magnitude to 20 – 60 may be required to mitigate not only the inter-ELM heat flux, but also to limit the PFC surface temperature excursions during ELM events. Further analysis of the projected effects of ELMs and disruptions on NSTX Upgrade divertor operation (including possible lithium-based divertor systems [168, 169]) is a topic for future research.

### 2.6.2. Snowflake Divertor

As discussed in Section 2.6.1, high flux expansion could play a critical role in the achievement of acceptable divertor heat fluxes during and between ELMs at high current and heating power in NSTX Upgrade. Very high flux expansions of 40-60 have recently been demonstrated in NSTX utilizing a "snowflake" [170] divertor as shown in Figure 42a. In order to support this and other future high-flux-expansion divertors such as the "Super-X" [171] (possible with additional in-vessel PF coils not part of the present Upgrade), additional divertor PF coils have been incorporated into the Upgrade CS design as shown in Figure 13. In particular, a third divertor PF coil (PF1C) will be added to the CS as shown in Figure 42b to support the snowflake and to improve control of flux expansion and strike-point location generally.

The snowflake divertor does have the additional challenge of control of multiple nearby x-points, and the configuration may also be more sensitive to changes in the plasma profiles and/or boundary magnetic topology. For example, for the highest heat flux high- $I_P=2\text{MA}$  scenarios of NSTX-U that will likely require long-pulse sustainment

of the snowflake configuration, the time-evolving OH solenoid current will introduce a time-varying leakage flux in the divertor region. Figure 43a shows the snowflake poloidal flux contours in the divertor region for the reference snowflake configuration of Figure 42b for three different OH solenoid current states, i.e. the minimum, zero, and maximum OH current utilizing all the divertor PF coils to produce the equilibrium. In this equilibrium calculation the strike-point and x-point locations, the inner and outer gap, and the boundary squareness can be held nearly fixed and the flux expansion is computed to vary less than 5% over the full range of OH currents.

To illustrate the effect of not utilizing all the divertor PF coils, Figure 43b shows the same OH current scan without including the PF1BL coil (i.e.  $I_{PF1BL} = 0$ ). For inductive operation with high  $I_P$ ,  $I_{OH}$  will start positive and swing through zero to negative values at the end of the  $I_P$  flat-top as shown in Figure 11. As seen in Figure 43b for positive  $I_{OH}$ , the outer-most strike-point of the snowflake increases in major radius as the x-points approach each other forming a nearly pure snowflake configuration [170] (i.e. overlapping x-points). This configuration reduces the wetted area for incident heat flux and has flux expansion 2 – 3 times lower than the reference configuration of Figure 43a. However, as the OH current passes through zero and becomes negative in the  $I_P$  flat-top, the reference snowflake configuration is largely recovered. Nevertheless, it is clear that having all three PF1A,B,C divertor coils is important for maintaining the snowflake configuration for a range of equilibrium states.

Importantly, the snowflake divertor (SFD) has recently demonstrated large (factor of 3 or more) reductions in peak heat flux and also up to a 50% reduction in carbon impurity production [172, 173]. Figure 44 shows an example of divertor heat flux reduction using a snowflake divertor in a 0.9MA flat-top plasma with  $\kappa = 2.4$ ,  $\beta_N = 4.5$ ,  $\beta_T = 16\%$  and  $P_{NBI} = 4\text{MW}$  [173]. The black curve in Figure 44 shows the divertor heat flux prior to snowflake formation in a standard NSTX high-triangularity lower-single-null configuration with outboard strike-point radius near  $R=0.3\text{-}0.35\text{m}$ . At this time in the discharge, the peak heat flux is  $4\text{-}7\text{MW/m}^2$ . The transition from standard LSN divertor to SFD occurs between  $t=0.35\text{s}$  and  $0.55\text{s}$ , and the SFD was fully formed by  $t=0.60\text{-}0.65\text{s}$ . The red ( $t=0.57\text{s}$ ) and blue ( $t=0.7\text{s}$ ) curves in Figure 44 show the divertor heat-flux is reduced by a factor of 2 – 3 shortly after the SFD is fully formed. Analysis indicates that most of this heat flux reduction is due to increased wetted area from high flux expansion of the SFD [173] rather than from strong changes in the SOL transport and/or radiation properties. At this time in the discharge, the SFD heat flux profiles still exhibit some peaking in the separatrix region near  $R = 0.30 - 0.35\text{m}$  and in the low flux expansion region near  $R = 0.55 - 0.65\text{m}$ . This variation of heat flux with flux expansion is consistent with previous results from NSTX[146] in which the peak divertor heat flux is found to vary inversely with flux expansion with only small changes

in the up-stream SOL power width.

Still later in the discharge at  $t=0.895s$ , the green curve in Figure 44 shows a further reduction in peak heat flux to values of  $0.5 - 1MW/m^2$ . At this time and beginning shortly after the formation of the SFD, the divertor radiated power is observed to increase, as is the C-II brightness. The C-III and C-IV brightness profiles showed broadening during the SFD formation, and their total brightness was increased by up to 50-100%. Using the brightness increase of the Balmer B6 line (measured in the outer strike point region) as an indication of the volumetric recombination onset, it appears that the partial detachment is likely occurring after  $t=650-700$  ms and results from increased divertor radiation and cooling from intrinsic C impurities [173]. Increased divertor radiation and partial detachment [174] has been achieved previously in NSTX [153] for standard divertor configurations using either extrinsic  $D_2$  or  $CD_4$  puffing. Thus, the results of Figure 44 indicate it is likely possible to combine the effects of increased wetted area (from increased flux expansion) and partial detachment (from either intrinsic or extrinsic impurities) to significantly reduce the peak divertor heat flux beyond what can be achieved with either method alone.

Overall, the snowflake divertor projects favorably to mitigating the stationary-plasma (and possibly ELM transient) high divertor heat fluxes in NSTX Upgrade and for supporting flat-top durations up to 5s at a plasma current of 2MA. Combining snowflake operation with a partially detached divertor appears particularly attractive, and would increase the heat-flux margin for operation at high current and power. Strike-point sweeping is another option that could provide additional heat-flux margin and is a topic for future analysis and research. Larger normalized strike-point radius ( $R_{strike}/R_0$ ) and the effects of very large parallel connection length will also be extensively investigated in MAST Upgrade which is designed specifically to incorporate a cryo-pumped "Super-X" divertor [171]. NSTX Upgrade (and MAST Upgrade) with increased current, field, and power will not only substantially extend and improve the understanding of the scaling of SOL heat flux width with plasma parameters, but will also contribute to the development of novel means of mitigating high heat fluxes during both stationary and transient plasma conditions for FNSF and for Demo.

### 3. Summary

Scoping studies for a range of ST energy confinement assumptions have been performed for NSTX Upgrade with a goal of determining the performance requirements to achieve a factor of 3-6 reduction in collisionality, support tests of 100% non-inductive current ramp-up and sustainment, and assess confinement, stability, and heat-flux scaling and mitigation at increased magnetic field and plasma current while also providing sufficient

flat-top duration for profile equilibration. The scoping studies indicate that a factor of two increase in plasma current, toroidal field, and NBI auxiliary heating power, a factor of 3 increase in ohmic solenoid flux, and a quintupling of the flat-top duration are sufficient to achieve the Upgrade goals. These performance objectives can be achieved with the combination of a new center-stack and a 2nd more tangentially injecting NBI.

Systematic free-boundary equilibrium calculations have been performed to assess the poloidal field coil current requirements to support the higher plasma current and access to high beta, and substantial engineering analysis and design has been performed for the structural reinforcements needed to handle the increased electromagnetic loads. In addition to the ex-vessel structural enhancements, the new CS incorporates numerous design improvements, including more robust flexible TF connections from the inner to outer TF legs, and a bottom-fed coaxial lead for the OH coil designed to substantially reduce the present NSTX  $n=1$  error field induced by an OH-TF electromagnetic interaction.

The 2nd neutral beam injector included in the Upgrade is designed to inject much more tangentially than the present NBI, and this injection geometry is predicted to increase the NBI CD efficiency by up to a factor of 2 enabling 100% non-inductive current drive at the 1MA level and control of the core safety factor profile. Importantly, the 2nd NBI is also computed to have 2 times higher fast-ion confinement (due to reduced bad orbit loss) at low plasma current as needed for non-inductive ramp-up studies. Also in support of non-inductive current ramp-up studies, the new CS incorporates additional poloidal field coils in the divertor to increase Coaxial Helicity Injection (CHI) injector flux by a factor of 2.5, increase the absorber coil current a factor of 3, and increase the absorber coil slew rate by a factor of 8. The higher TF and enhanced CS PF coil and CHI capability combined with the 2nd NBI are projected to be capable of non-inductive start-up of at least 300kA and ramp-up to the 1MA level. The more tangential NBI requires a significant modification to the NSTX vacuum vessel through the addition of a radially offset port cap. Further, the 2nd NBI requires considerable test-cell floor space and relocation of numerous diagnostics and associated racks and equipment.

Just as the equilibrium electromagnetic forces are expected to increase by up to a factor of four, disruption loads are anticipated to increase by a similar factor. The disruption forces from induced currents in the passive conducting plates are sufficiently high that additional plate re-enforcements at the plate attachment points are required. Halo current forces on the passive plates can also be withstood with the same plate attachment enhancements. If thicker plates are someday utilized to access  $I_P > 2\text{MA}$ , the plate circulating current (but not the net toroidal current) is predicted to increase due to decreased plate resistance. However, despite the increased plate circulating current, it is expected that the plate displacement/deformation could be significantly

reduced by the increased passive plate thickness. Halo currents on the centerstack would apply a lateral load that requires improved support structure on the bottom of the CS and shims at the top of the CS. With respect to the achievable beta in the Upgrade, the structural enhancements support operation at high  $\beta_N$  up to 8 at full current and field at low  $l_i$ . The addition of a 2nd NBI port and associated reduction in conducting wall area is computed to produce only a small reduction on the ideal-wall limit.

Finally, the divertor heat flux width is observed to scale inversely with plasma current in NSTX and could lead to very high heat fluxes in the NSTX Upgrade divertor at maximum current and heating power. The high-flux-expansion "snowflake" divertor has demonstrated considerable heat flux reduction in NSTX, and the incorporation of additional PF coils in the new CS enables operation with upper and lower snowflake divertors. Up/down power splitting using upper and lower snowflake divertors is projected to reduce the peak divertor heat flux to 10MW/m<sup>2</sup> and inertially maintain divertor tile temperature below sublimation damage limits for 5s pulses at full current and high heating power. Divertor radiation/detachment and possibly strike-point sweeping are additional methods that could be utilized for mitigation of high heat flux.

In summary, the new capabilities of the NSTX Upgrade are anticipated to greatly enhance ST research in support of assessing the ST as a potential Fusion Nuclear Science Facility (FNSF). The NSTX Upgrade project is presently scheduled to be completed in 2014.

## **Acknowledgments**

This work was supported in part by the U.S. DOE Contract Number DE-AC02-09CH11466.

Prepared by LLNL under Contract DE-AC52-07NA27344.

## References

- [1] PENG, Y.-K. M. and STRICKLER, D. J., Nucl. Fus. **26** (1986) 769.
- [2] PENG, Y.-K. M., GALAMBOS, J. D., and SHIPE, P. C., Fus. Technol. **21** (1992) 1729.
- [3] PENG, Y.-K. M., FOGARTY, P. J., BURGESS, T. W., STRICKLER, D. J., NELSON, B. E., et al., Plasma Phys. and Contr. Fus. **47** (2005) B263.
- [4] PENG, Y.-K. M., BURGESS, T. W., CARROLL, A. J., NEUMEYER, C. L., CANIK, J. M., et al., Fusion Sci. Technol. **56** (2009) 957.
- [5] KAYE, S. M., ONO, M., PENG, Y.-K., BATCHELOR, D. B., CARTER, M. D., et al., Fus. Technol. **36** (1999) 16.
- [6] ONO, M., KAYE, S. M., PENG, Y.-K. M., BARNES, G., BLANCHARD, W., et al., Nucl. Fus. **40** (2000) 557.
- [7] KAYE, S. M., LEVINTON, F. M., STUTMAN, D., TRITZ, K., YUH, H., et al., Nucl. Fus. **47** (2007) 499.
- [8] VALOVIC, M., AKERS, R., CUNNINGHAM, G., GARZOTTI, L., LLOYD, B., et al., Nucl. Fus. **49** (2009) 075016.
- [9] VALOVIC, M., AKERS, R., DE BOCK, M., MCCONE, J., GARZOTTI, L., et al., Nucl. Fus. **51** (2011) 073045.
- [10] LUCE, T. C., PETTY, C. C., and CORDEY, J. G., Plasma Phys. and Contr. Fus. **50** (2008) 043001.
- [11] ITER Physics Expert Groups on Confinement and Transport and Confinement Modelling and Database and ITER Physics Basis Editors, Nucl. Fus. **39** (1999) 2175.
- [12] DOYLE, E., HOULBERG, W., KAMADA, Y., MUKHOVATOV, V., OSBORNE, T., et al., Nucl. Fus. **47** (2007) S18.
- [13] KAYE, S. M., BELL, R. E., GATES, D., LeBlanc, B. P., LEVINTON, F. M., et al., Phys. Rev. Lett. **98** (2007) 175002.
- [14] MAZZUCATO, E., SMITH, D. R., BELL, R. E., KAYE, S. M., HOSEA, J. C., et al., Phys. Rev. Lett. **101** (2008) 075001.
- [15] MAZZUCATO, E., BELL, R. E., ETHIER, S., HOSEA, J. C., KAYE, S. M., et al., Nucl. Fus. **49** (2009) 055001.
- [16] SMITH, D. R., KAYE, S. M., LEE, W., MAZZUCATO, E., PARK, H. K., et al., Phys. Rev. Lett. **102** (2009) 225005.
- [17] YUH, H. Y., KAYE, S. M., LEVINTON, F. M., MAZZUCATO, E., MIKKELSEN, D. R., et al., Phys. Rev. Lett. **106** (2011) 055003.
- [18] REN, Y., KAYE, S. M., MAZZUCATO, E., GUTTENFELDER, W., BELL, R. E., et al., Phys. Rev. Lett. **106** (2011) 165005.
- [19] STUTMAN, D., Delgado-Aparicio, L., GORELENKOV, N., FINKENTHAL, M., FREDRICKSON, E., et al., Phys. Rev. Lett. **102** (2009) 115002.
- [20] GORELENKOV, N. N., STUTMAN, D., TRITZ, K., BOOZER, A., Delgado-Aparicio, L., et al., Nucl. Fus. **50** (2010) 084012.
- [21] WONG, K. L., KAYE, S., MIKKELSEN, D. R., KROMMES, J. A., HILL, K., et al., Phys. Rev. Lett. **99** (2007) 135003.
- [22] WONG, K. L., KAYE, S., MIKKELSEN, D. R., KROMMES, J. A., HILL, K., et al., Phys. Plasmas **15** (2008) 056108.
- [23] SMITH, D. R., GUTTENFELDER, W., LeBlanc, B., and MIKKELSEN, D., Plasma Phys. and Contr. Fus. **53** (2011) 035013.
- [24] GUTTENFELDER, W., CANDY, J., KAYE, S. M., NEVINS, W. M., WANG, E., et al., Phys.

- Rev. Lett. **106** (2011) 155004.
- [25] HORTON, W., ZHU, P., HOANG, G. T., ANIEL, T., OTTAVIANI, M., et al., Phys. Plasmas **7** (2000) 1494.
  - [26] ZHU, W., SABBAGH, S. A., BELL, R. E., BIALEK, J. M., BELL, M. G., et al., Phys. Rev. Lett. **96** (2006) 225002.
  - [27] PARK, J. K., BOOZER, A. H., and MENARD, J. E., Phys. Rev. Lett. **102** (2009) 065002.
  - [28] SABBAGH, S. A., BERKERY, J. W., BELL, R. E., BIALEK, J. M., GERHARDT, S. P., et al., Nucl. Fus. **50** (2010) 025020.
  - [29] BERKERY, J. W., SABBAGH, S. A., BETTI, R., BELL, R. E., GERHARDT, S. P., et al., Phys. Rev. Lett. **106** (2011) 075004.
  - [30] MENARD, J. E., BELL, R. E., GATES, D. A., GERHARDT, S. P., PARK, J.-K., et al., Nucl. Fus. **50** (2010) 045008.
  - [31] GERHARDT, S. P., MENARD, J. E., PARK, J.-K., BELL, R., GATES, D. A., et al., Plasma Phys. and Contr. Fus. **52** (2010) 104003.
  - [32] MAINGI, R., HUBBARD, A. E., MEYER, H., HUGHES, J. W., KIRK, A., et al., Nucl. Fus. **51** (2011) 063036.
  - [33] SAUTER, O., ANGIONI, C., and LIN-LIU, Y. R., Phys. Plasmas **6** (1999) 2834.
  - [34] TROYON, F., GRUBER, R., SAURENMANN, H., SEMENZATO, S., and SUCCI, S., Plasma Phys. and Contr. Fus. **26** (1984) 209.
  - [35] TROYON, F. and GRUBER, R., Phys. Lett. A **110** (1985) 29.
  - [36] STRAIT, E., Phys. Plasmas **1** (1994) 1415.
  - [37] MENARD, J. E., BELL, M. G., BELL, R. E., GATES, D. A., KAYE, S. M., et al., Phys. Plasmas **11** (2004) 639.
  - [38] GREENWALD, M., TERRY, J. L., WOLFE, S. M., EJIMA, S., BELL, M. G., et al., Nucl. Fus. **28** (1988) 2199.
  - [39] GREENWALD, M., Plasma Phys. and Contr. Fus. **44** (2002) R27.
  - [40] GERHARDT, S. P., ANDRE, R., and MENARD, J. E., "Exploration of the equilibrium operating space for NSTX-Upgrade", submitted to Nuclear Fusion, December 2011.
  - [41] GERHARDT, S. P., GATES, D. A., KAYE, S. M., MAINGI, R., MENARD, J. E., et al., Nucl. Fus. **51** (2011) 073031.
  - [42] GRUBER, O., ARSLANBEKOV, R., ATANASIU, C., BARD, A., BECKER, G., et al., Nuclear Fusion **41** (2001) 1369.
  - [43] ONGENA, J., MONIER-GARBET, P., SUTTROP, W., ANDREW, P., BÉCOULET, M., et al., Nucl. Fus. **44** (2004) 124.
  - [44] GATES, D. A., MAINGI, R., MENARD, J., KAYE, S., SABBAGH, S. A., et al., Phys. Plasmas **13** (2006) 056122.
  - [45] STIX, T. H., Plasma Phys. **14** (1972) 367.
  - [46] MEDLEY, S. S., GORELENKOV, N. N., ANDRE, R., BELL, R. E., DARROW, D. S., et al., Nucl. Fus. **44** (2004) 1158.
  - [47] START, D. F. H., CORDEY, J. G., and JONES, E. M., Plasma Physics **22** (1980) 303.
  - [48] CORDEY, J. G., Plasma Phys. and Contr. Fus. **26** (1984) 123.
  - [49] FISCH, N. J., Rev. Mod. Phys. **59** (1987) 175.
  - [50] MENARD, J. E., BELL, R. E., GATES, D. A., KAYE, S. M., LEBLANC, B. P., et al., Phys. Rev. Lett. **97** (2006) 095002.
  - [51] GERHARDT, S. P., FREDRICKSON, E., GATES, D., KAYE, S., MENARD, J., et al., Nucl. Fus. **51** (2011) 033004.
  - [52] BICKERTON, R. J., CONNOR, J. W., and TAYLOR, J. B., Nature Phys. Sci. **229** (1971) 110.



- [53] ZARNSTORFF, M. C., BELL, M. G., BITTER, M., GOLDSTON, R. J., GREK, B., et al., Phys. Rev. Lett. **60** (1988) 1306.
- [54] WILSON, H. R., Nucl. Fus. **32** (1992) 257.
- [55] KAYE, S. M., BELL, M. G., BELL, R. E., FREDRICKSON, E. D., LEBLANC, B. P., et al., Nucl. Fus. **46** (2006) 848.
- [56] HAHM, T. S. and BURRELL, K. H., Phys. Plasmas **2** (1995) 1648.
- [57] WALTZ, R. E. and MILLER, R. L., Phys. Plasmas **6** (1999) 4265.
- [58] KAYE, S. M., SOLOMON, W., BELL, R. E., LEBLANC, B. P., LEVINTON, F., et al., Nucl. Fus. **49** (2009) 045010.
- [59] PEETERS, A. G., ANGIONI, C., and STRINTZI, D., Phys. Rev. Lett. **98** (2007) 265003.
- [60] MIKKELSEN, D. R., Phys. Fluids B **1** (1989) 333.
- [61] LLOYD, B., JACKSON, G., TAYLOR, T., LAZARUS, E., LUCE, T., et al., Nucl. Fus. **31** (1991) 2031.
- [62] MENARD, J. E., BELL, R. E., FREDRICKSON, E. D., GATES, D. A., KAYE, S. M., et al., Nucl. Fus. **45** (2005) 539.
- [63] GATES, D. A., KESSEL, C., MENARD, J., TAYLOR, G., WILSON, J., et al., Nucl. Fus. **46** (2006) S22.
- [64] EJIMA, S., CALLIS, R. W., LUXON, J. L., STAMBAUGH, R. D., TAYLOR, T. S., et al., Nucl. Fus. **22** (1982) 1313.
- [65] MENARD, J. E., LEBLANC, B. P., SABBAGH, S. A., BELL, M. G., BELL, R. E., et al., Nucl. Fus. **41** (2001) 1197.
- [66] WESLEY, J., BELJAKOV, V., BULMER, R., HOGAN, J., KAISER, T., et al., The ITER poloidal field system, in *Plasma Physics and Controlled Nuclear Fusion Research 1990*, volume 3 of *Thirteenth conference proceedings*, p. 421, Washington, DC, 1991, International Atomic Energy Association, Vienna.
- [67] RAMAKRISHNAN, S., NEUMEYER, C., LAWSON, J., MOZULAY, R., BAKER, E., et al., Power system for NSTX Upgrade, 2011, 24th IEEE Symposium on Fusion Engineering, 2011, Chicago IL.
- [68] FERRON, J. R., WALKER, M. L., LAO, L. L., St. John, H. E., HUMPHREYS, D. A., et al., Nucl. Fus. **38** (1998) 1055.
- [69] GATES, D. A., FERRON, J. R., BELL, M., GIBNEY, T., JOHNSON, R., et al., Nucl. Fus. **46** (2006) 17.
- [70] HUMPHREYS, D. A., CASPER, T. A., EIDIETIS, N., FERRARA, M., GATES, D. A., et al., Nucl. Fus. **49** (2009) 115003.
- [71] KOLEMEN, E., GATES, D. A., ROWLEY, C. W., KASDIN, N. J., KALLMAN, J., et al., Nucl. Fus. **50** (2010) 105010.
- [72] KOLEMEN, E., GATES, D. A., GERHARDT, S., KAITA, R., KUGEL, H., et al., Nucl. Fus. **51** (2011) 113024.
- [73] LAVAL, G., PELLAT, R., and SOULE, J. S., Phys. Fluids **17** (1974) 835.
- [74] HAAS, F. A., Nucl. Fus. **15** (1975) 407.
- [75] LAZARUS, E. A., LISTER, J. B., and NEILSON, G. H., Nucl. Fus. **30** (1990) 111.
- [76] WARD, D. J., BONDESON, A., and HOFMANN, F., Nucl. Fus. **33** (1993) 821.
- [77] WARD, D. J. and HOFMANN, F., Nucl. Fus. **34** (1994) 401.
- [78] ROBERTO, M., Nucl. Fus. **32** (1992) 1666.
- [79] MENARD, J. E., JARDIN, S. C., KAYE, S. M., KESSEL, C. E., and MANICKAM, J., Nucl. Fus. **37** (1997) 595.
- [80] ANGIONI, C., PEETERS, A. G., PEREVERZEV, G. V., RYTER, F., TARDINI, G., et al.,

- Phys. Rev. Lett. **90** (2003) 205003.
- [81] ANGIONI, C., WEISEN, H., KARDAUN, O. J. W. F., MASLOV, M., ZABOLOTSKY, A., et al., Nucl. Fus. **47** (2007) 1326.
- [82] HIRSHMAN, S. P. and SIGMAR, D. J., Nucl. Fus. **21** (1981) 1079.
- [83] BELL, M. G., KUGEL, H. W., KAITA, R., ZAKHAROV, L. E., SCHNEIDER, H., et al., Plasma Phys. and Contr. Fus. **51** (2009) 124054.
- [84] ZHANG, H., SMITH, M., TITUS, P., ROGOFF, P., ZOLFAGHARI, A., et al., Fusion Sci. Technol. **60** (2011) 664.
- [85] ZOLFAGHARI, A., WILLARD, T., and SMITH, M., Coupled multiphysics analysis of the TF coil structure in the NSTX Upgrade, 2011, PPPL Report 4680.
- [86] ZOLFAGHARI, A., TITUS, P., CHRZANOWSKI, J., SALEHZADEH, A., and DAHLGREN, F., Fusion Sci. Technol. **60** (2011) 658.
- [87] MENARD, J. E., BROMBERG, L., BROWN, T., BURGESS, T., DIX, D., et al., Nucl. Fus. **51** (2011) 103014.
- [88] NAJMABADI, F. and The ARIES Team, Fus. Engin. and Design **65** (2003) 143.
- [89] STEVENSON, T., MCCORMACK, B., LOESSER, G. D., KALISH, M., RAMAKRISHNAN, S., et al., A neutral beam injector upgrade for NSTX, 2002, PPPL Report 3651.
- [90] DAHLGREN, F., WRIGHT, K., KAMPERSCHROER, J., GRISHAM, L., LONTAI, L., et al., TPX/TFTR neutral beam energy absorbers, in *Proceedings of the 15th IEEE/NPSS Symposium on Fusion Engineering*, volume 1, pp. 455–461, 1993.
- [91] TRESEMER, K., STEVENSON, T., PRINISKI, C., WINKELMAN, J., BRYANT, L., et al., Fusion Sci. Technol. (2011) 303.
- [92] STORK, D., MEYER, H., AKERS, R., BICKLEY, A. J., BUTTERY, R. J., et al., The upgrade to the Mega Amp Spherical Tokamak, 2010, Paper ICC/P5-06 in Fusion Energy 2010 (Proc. 23rd Int. Conf. Daejeon, 2010).
- [93] BARRETT, T. R., JONES, C., BLATCHFORD, P., SMITH, B., MCADAMS, R., et al., Fus. Engin. and Design **86** (2011) 789.
- [94] MIKKELSEN, D. R., WHITE, R. B., AKERS, R. J., KAYE, S. M., MCCUNE, D. C., et al., Phys. Plasmas **4** (1997) 3668.
- [95] JARDIN, S. C., POMPHREY, N., and DELUCIA, J., J. Comput. Phys. **66** (1986) 481.
- [96] KESSEL, C. E., BELL, R. E., BELL, M. G., GATES, D. A., KAYE, S. M., et al., Phys. Plasmas **13** (2006) 056108.
- [97] FREDRICKSON, E. D., CHENG, C. Z., DARROW, D., FU, G., GORELENKOV, N. N., et al., Phys. Plasmas **10** (2003) 2852.
- [98] FREDRICKSON, E. D., BELL, R. E., DARROW, D. S., FU, G. Y., GORELENKOV, N. N., et al., Phys. Plasmas **13** (2006) 056109.
- [99] MAINGI, R., BELL, R. E., CANIK, J. M., GERHARDT, S. P., KAYE, S. M., et al., Phys. Rev. Lett. **25** (2010) 135004.
- [100] HOULBERG, W. A., SHAIN, K. C., HIRSHMAN, S. P., and ZARNSTORFF, M. C., Phys. Plasmas **4** (1997) 3230.
- [101] SABBAGH, S. A., SONTAG, A. C., BIALEK, J. M., GATES, D. A., GLASSER, A. H., et al., Nucl. Fus. **46** (2006) 635.
- [102] NAJMABADI, F. and The ARIES Team, Fus. Engin. and Design **41** (1998) 365.
- [103] NAJMABADI, F., ABDOU, A., BROMBERG, L., BROWN, T., CHAN, V. C., et al., Fus. Engin. and Design **80** (2006) 3.
- [104] FUJITA, T., IDE, S., KAMADA, Y., SUZUKI, T., OIKAWA, T., et al., Phys. Rev. Lett. **87** (2001) 085001.

- [105] SHIRAIWA, S., IDE, S., ITOH, S., MITARAI, O., NAITO, O., et al., Phys. Rev. Lett. **92** (2004) 035001.
- [106] YUH, H. Y., LEVINTON, F. M., BELL, R. E., HOSEA, J. C., KAYE, S. M., et al., Phys. Plasmas **16** (2009) 056120.
- [107] TAYLOR, G., BELL, R. E., HOSEA, J. C., LEBLANC, B. P., PHILLIPS, C. K., et al., Phys. Plasmas **17** (2010) 056114.
- [108] TAYLOR, G., BONOLI, P. T., GREENC, D. L., HARVEY, R. W., HOSEA, J. C., et al., HHFW heating and current drive studies of NSTX H-mode plasmas, 2011, PPPL Report 4634.
- [109] PHILLIPS, C. K., BELL, R. E., BERRY, L. A., BONOLI, P. T., HARVEY, R. W., et al., Nucl. Fus. **49** (2009) 075015.
- [110] HOSEA, J., BELL, R. E., LEBLANC, B. P., PHILLIPS, C. K., TAYLOR, G., et al., Phys. Plasmas **15** (2008) 056104.
- [111] LIU, D., HEIDBRINK, W. W., PODESTA, M., BELL, R. E., FREDRICKSON, E. D., et al., Plasma Phys. and Contr. Fus. **52** (2010) 025006.
- [112] KUGEL, H. W., MANSFIELD, D., MAINGI, R., BELL, M. G., BELL, R. E., et al., J. Nucl. Mater. **390-391** (2009) 1000.
- [113] CANIK, J. M., MAINGI, R., EVANS, T. E., GERHARDT, R. E. B. S. P., LEBLANC, B. P., et al., Phys. Rev. Lett. **104** (2010) 045001.
- [114] KUGEL, H. W., BELL, M., BERZAK, L., BROOKS, A., ELLIS, R., et al., Fus. Engin. and Design **84** (2009) 1125.
- [115] ELLIS, R., KAITA, R., KUGEL, H., PALUZZI, G., VIOLA, M., et al., Mechanical design of the NSTX liquid lithium divertor, 2009, 23rd IEEE/NPSS Symposium on Fusion Engineering, 2009, San Diego, CA.
- [116] NYGREN, R. E., HARJES, H. C., WAKELAND, P., ELLIS, R., KUGEL, H. W., et al., Fus. Engin. and Design **84** (2009) 1438.
- [117] ALLAIN, J. P. and BROOKS, J. N., Nucl. Fus. **51** (2011) 023002.
- [118] SOUKHANOVSKII, V. A., BELL, M. G., BLANCHARD, W. R., DONG, J. K., GERNHARDT, R. C., et al., High Pressure Supersonic Gas Jet Fueling on NSTX, in *2007 IEEE 22nd Symposium on Fusion Engineering*, pp. 1-4, IEEE, 2007.
- [119] SENGOKU, S., NAGAMI, M., ABE, M., HOSHINO, K., KAMEARI, A., et al., Nucl. Fus. **25** (1985) 1475.
- [120] KAUFMANN, M., BÜCHL, K., FUSSMANN, G., GEHRE, O., GRASSIE, K., et al., Nucl. Fus. **28** (1988) 827.
- [121] RIBEIRO, C., AKERS, R., ALLADIO, F., AXON, K., BAYLOR, L., et al., Fus. Engin. and Design **58-59** (2001) 319.
- [122] BAYLOR, L., JERNIGAN, T., PARKS, P., ANTAR, G., BROOKS, N., et al., Nucl. Fus. **47** (2007) 1598.
- [123] RAMAN, R., Fus. Engin. and Design **83** (2008) 1368.
- [124] JARBOE, T. R., Fus. Technol. **15** (1989) 7.
- [125] TAYLOR, G., EFTHIMION, P. C., KESSEL, C. E., HARVEY, R. W., SMIRNOV, A. P., et al., Phys. Plasmas **11** (2004) 4733.
- [126] DIEM, S. J., TAYLOR, G., CAUGHMAN, J. B., EFTHIMION, P. C., KUGEL, H., et al., Nucl. Fus. **49** (2009) 095027.
- [127] RAMAN, R., MUELLER, D., NELSON, B. A., JARBOE, T. R., GERHARDT, S., et al., Phys. Rev. Lett. **104** (2010) 095003.
- [128] NELSON, B. A., JARBOE, T. R., MUELLER, D., RAMAN, R., BELL, M., et al., Nucl. Fus. **51** (2011) 063008.

- [129] RAMAN, R., JARDIN, S. C., MENARD, J., and JARBOE, T. R., Nucl. Fus. **51** (2011) 113018.
- [130] RAMAN, R., JARBOE, T., O'NEILL, R., HAMP, W., NELSON, B., et al., Nucl. Fus. **45** (2005) L15.
- [131] RAMAN, R., JARBOE, T. R., MUELLER, D., SCHAFFER, M. J., MAQUEDA, R., et al., Plasma Phys. and Contr. Fus. **43** (2001) 305.
- [132] RAMAN, R., JARBOE, T., MUELLER, D., SCHAFFER, M., MAQUEDA, R., et al., Nucl. Fus. **41** (2001) 1081.
- [133] NELSON, B., JARBOE, T., ORVIS, D., MCCULLOUGH, L., XIE, J., et al., Phys. Rev. Lett. **72** (1994) 3666.
- [134] NELSON, B. A., JARBOE, T. R., MARTIN, A. K., ORVIS, D. J., XIE, J., et al., Phys. Plasmas **2** (1995) 2337.
- [135] RAMAN, R., NELSON, B. A., BELL, M. G., JARBOE, T. R., MUELLER, D., et al., Phys. Rev. Lett. **97** (2006) 175002.
- [136] JARDIN, S., BELL, M., and POMPHREY, N., Nucl. Fus. **33** (1993) 371.
- [137] GERHARDT, S. P., MENARD, J. E., and the NSTX Team, Nucl. Fus. **49** (2009) 025005.
- [138] TITUS, P. H., AVASARALLA, S., BROOKS, A., and HATCHER, R., Fus. Engin. and Design (2011), in press.
- [139] GERHARDT, S. P., FREDRICKSON, E., GUTTADORA, L., KAITA, R., KUGEL, H., et al., Rev. Sci. Instrum. **82** (2011) 103502.
- [140] MENARD, J. E., <http://w3.pppl.gov/jmenard/software/lrdfit/lrdfit-index.htm>.
- [141] BIALEK, J., BOOZER, A. H., MAUEL, M. E., and NAVRATIL, G. A., Phys. Plasmas **8** (2001) 2170.
- [142] SABBAGH, S. A., BIALEK, J. M., BELL, R. E., GLASSER, A. H., LEBLANC, B. P., et al., Nucl. Fus. **44** (2004) 560.
- [143] LOARTE, A., LIPSCHULTZ, B., KUKUSHKIN, A., MATTHEWS, G., STANGEBY, P., et al., Nucl. Fus. **47** (2007) S203.
- [144] LABOMBARD, B., TERRY, J. L., HUGHES, J. W., BRUNNER, D., PAYNE, J., et al., Phys. Plasmas **18** (2011) 056104.
- [145] LASNIER, C. J., MAKOWSKI, M. A., BOEDO, J. A., ALLEN, S. L., BROOKS, N. H., et al., J. Nucl. Mater. (2011), in press.
- [146] GRAY, T. K., MAINGI, R., SOUKHANOVSKII, V. A., SURANY, J. E., AHN, J.-W., et al., J. Nucl. Mater. **415** (2011) S360.
- [147] STANGEBY, P. C., *The plasma boundary of magnetic fusion devices*, Institute of Physics Publishing, 2000.
- [148] MAINGI, R., BELL, M., BELL, R., BUSH, C., FREDRICKSON, E., et al., Nucl. Fus. **43** (2003) 969.
- [149] LEONARD, A., LASNIER, C., CUTHBERTSON, J., EVANS, T., FENSTERMACHER, M., et al., J. Nucl. Mater. **220-222** (1995) 325.
- [150] AHN, J.-W. and COUNSELL, G., J. Nucl. Mater. **290-293** (2001) 820.
- [151] PAUL, S., MAINGI, R., SOUKHANOVSKII, V., KAYE, S., and KUGEL, H., J. Nucl. Mater. **337-339** (2005) 251.
- [152] SOUKHANOVSKII, V. A., MAINGI, R., ROQUEMORE, A. L., BOEDO, J., BUSH, C., et al., J. Nucl. Mater. **337-339** (2005) 475.
- [153] SOUKHANOVSKII, V. A., MAINGI, R., GATES, D. A., MENARD, J. E., RAMAN, S. F. P. R., et al., Nucl. Fus. **49** (2009) 095025.
- [154] SOUKHANOVSKII, V. A., MAINGI, R., GATES, D. A., MENARD, J. E., PAUL, S. F., et al., Phys. Plasmas **16** (2009) 022501.

- [155] BROOKS, J., J. Nucl. Mater. **170** (1990) 164.
- [156] KELLY, F., MAINGI, R., MAQUEDA, R., MENARD, J., and PAUL, S., J. Nucl. Mater. **390-391** (2009) 436.
- [157] ITAMI, K., HOSOGANE, N., ASAKURA, N., KUBO, H., TSUJI, S., et al., J. Nucl. Mater. .
- [158] LEONARD, A., SUTTROP, W., OSBORNE, T., EVANS, T., HILL, D., et al., Journal of Nuclear Materials **241-243** (1997) 628.
- [159] LEONARD, A., HERRMANN, A., ITAMI, K., LINGERTAT, J., LOARTE, A., et al., J. Nucl. Mater. **266-269** (1999) 109.
- [160] HERRMANN, A., EICH, T., JACHMICH, S., LAUX, M., ANDREW, P., et al., J. Nucl. Mater. **313-316** (2003) 759.
- [161] FEDERICI, G., LOARTE, A., and STROHMAYER, G., Plasma Phys. and Contr. Fus. **45** (2003) 1523.
- [162] RICCARDO, V., ANDREW, P., INGESSON, L. C., and MADDALUNO, G., Plasma Phys. and Contr. Fus. **44** (2002) 919.
- [163] RICCARDO, V., LOARTE, A., and CONTRIBUTORS, T. J. E., Nucl. Fus. **45** (2005) 1427.
- [164] HOLLMANN, E., JERNIGAN, T., GROTH, M., WHYTE, D., GRAY, D., et al., Nucl. Fus. **45** (2005) 1046.
- [165] GRANETZ, R., WHYTE, D., IZZO, V., BIEWER, T., REINKE, M., et al., Nucl. Fus. **46** (2006) 1001.
- [166] ARNOUX, G., LOARTE, A., RICCARDO, V., FUNDAMENSKI, W., and HUBER, A., Nucl. Fus. **49** (2009) 085038.
- [167] AHN, J.-W., MAINGI, R., MASTROVITO, D., and ROQUEMORE, A. L., Rev. Sci. Instrum. **81** (2010) 023501.
- [168] ABDOU, M., Fus. Engin. and Design **54** (2001) 181.
- [169] SIZYUK, V. and HASSANEIN, A., J. Nucl. Mater. **415** (2011) S881.
- [170] RYUTOV, D. D., Phys. Plasmas **14** (2007) 064502.
- [171] VALANJU, P. M., KOTSCHENREUTHER, M., MAHAJAN, S. M., and CANIK, J., Phys. Plasmas **16** (2009) 056110.
- [172] SOUKHANOVSKII, V. A., AHN, J.-W., BELL, R. E., GATES, D. A., GERHARDT, S., et al., Nucl. Fus. **51** (2011) 012001.
- [173] SOUKHANOVSKII, V. A., AHN, J.-W., BATTAGLIA, D., BELL, R. E., DIALLO, A., et al., The snowflake divertor: a game-changer for magnetic fusion devices?, in *38th EPS conference on Plasma Physics*, European Physical Society, 2011, Paper O3.109.
- [174] PETRIE, T., HILL, D., ALLEN, S., BROOKS, N., BUCHENAUER, D., et al., Nucl. Fus. **37** (1997) 321.

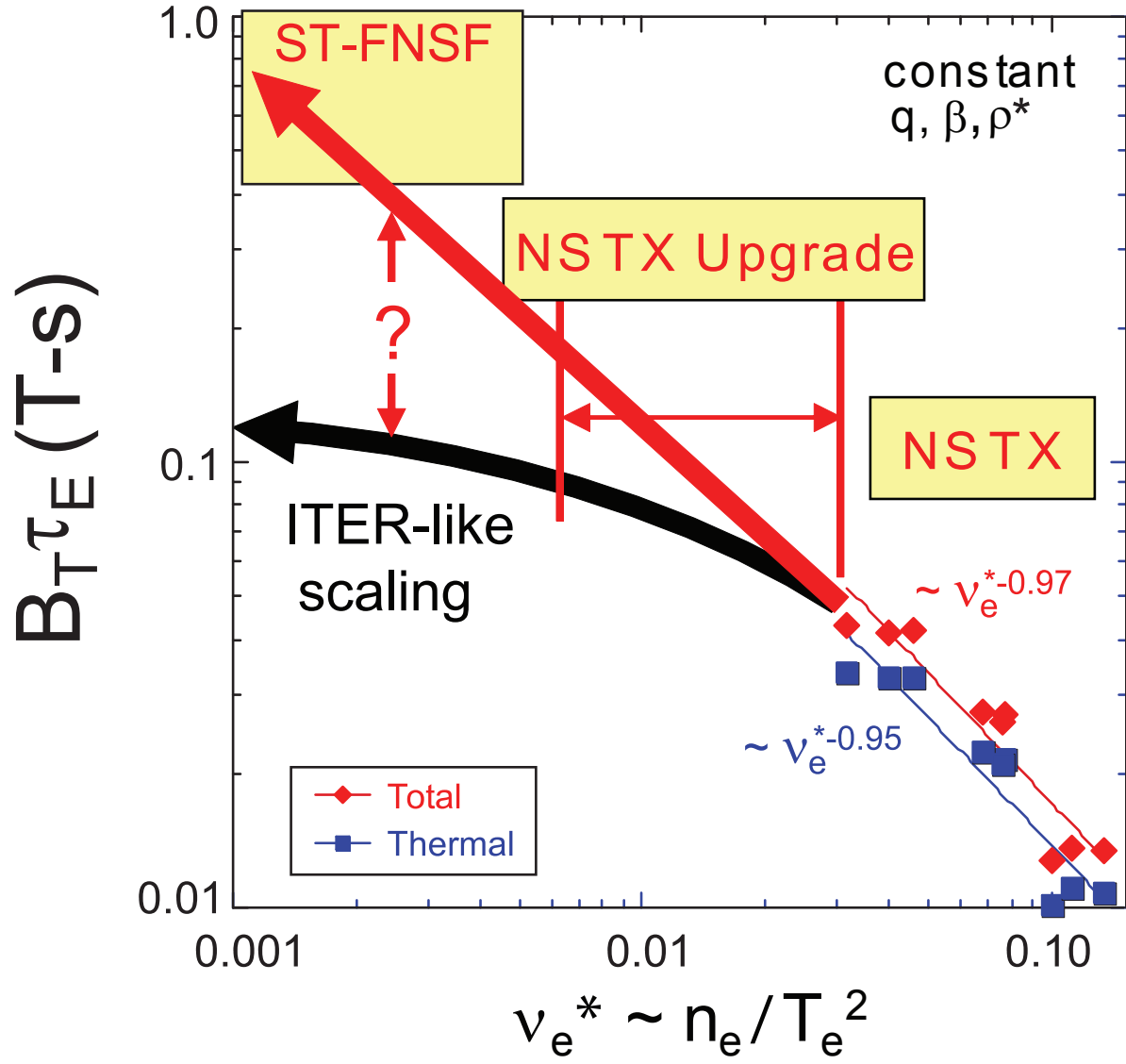


**Figure 1.** Product of toroidal field ( $B_T$ ) and energy confinement time ( $\tau_E$ ) versus  $\nu_e^*$  for NSTX and projections for NSTX Upgrade and ST-FNSF for ITER H-mode and ST confinement scalings.

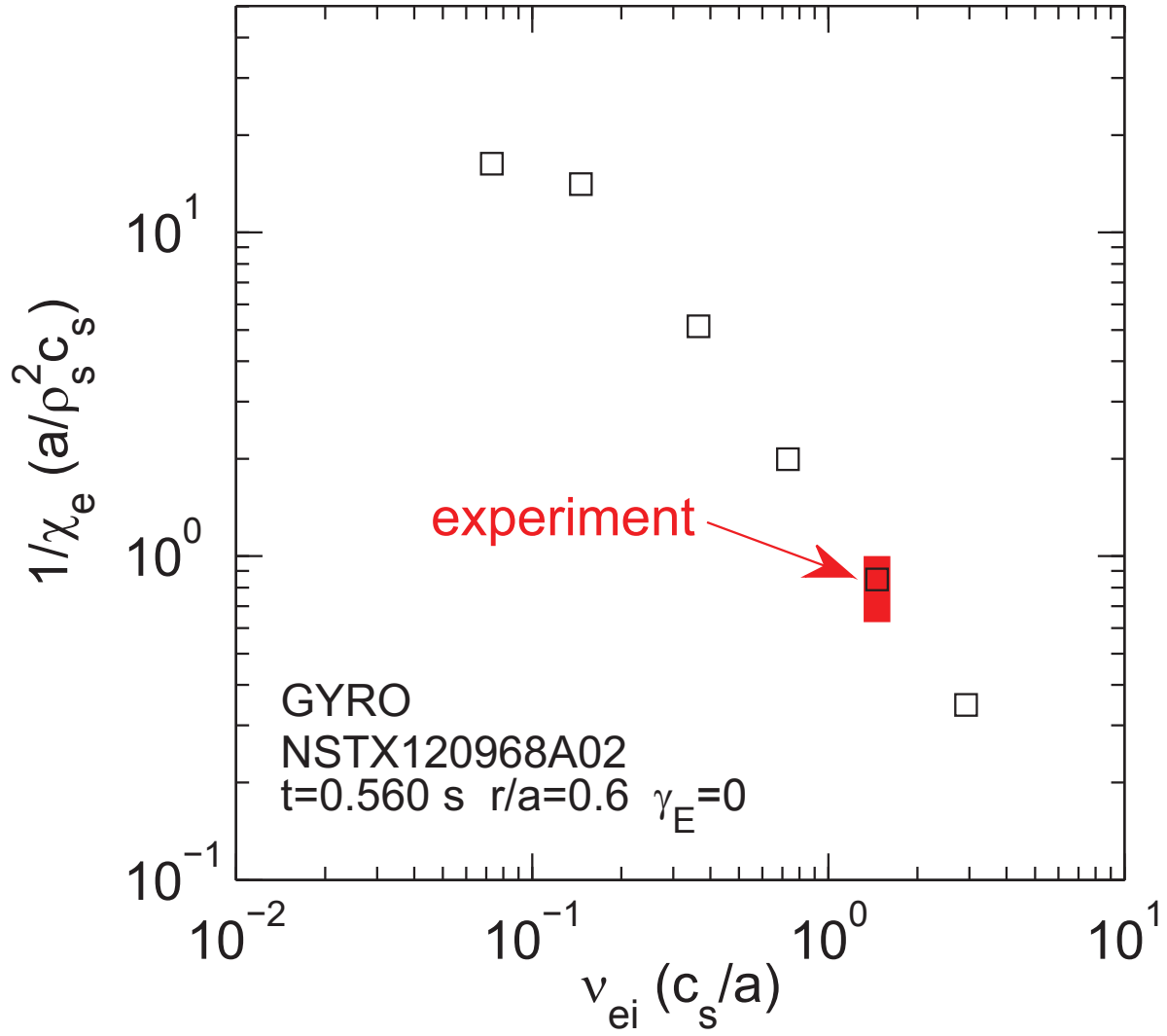


**Figure 2.** Nonlinear gyrokinetic simulations of the normalized inverse anomalous electron thermal diffusivity  $\chi_e$  versus normalized collisionality for microtearing instabilities in NSTX.

NSTX 0D scaling vs TRANSP							NSTX Upgrade Scenarios													
Device and scenario	NSTX 0.7MA $f_{GW}=0.6, H_{98}=1$		NSTX 0.9MA $f_{GW}=0.95, H_{98}=1$		NSTX 1.3MA $f_{GW}=0.73, H_{98}=1$		NSTX Reference	NSTX-U	NSTX-U	NSTX-U	NSTX-U	NSTX-U	NSTX-U	NSTX-U	NSTX-U	NSTX-U				
	100% NCD	Long-pulse	Max $I_p$	Max $I_p, P_{heat}$	100% NCD	Max $I_p$		High $f_{SS}$												
Confinement scaling	0D scaling model	TRANSP 135440 S04	0D scaling model	TRANSP 133078 A01	0D scaling model	TRANSP 132911 A01	0D scaling model	H98y2	H98y2	H98y2	H98y2	H98y2	H98y2	ST	ST	ST	ST			
$I_p$ [MA]	0.71	0.71	0.92	0.92	1.30	1.30	1.0	1.0	1.10	1.02	0.90	0.90	2.00	2.00	2.00	2.00	1.11	1.16		
$B_T$ [Tesla]	0.42	0.42	0.44	0.44	0.49	0.49	0.45	0.45	1.00	1.00	0.75	0.75	1.00	1.00	1.00	1.00	1.00	1.00		
Aspect ratio A	1.49	1.49	1.50	1.50	1.45	1.45	1.5	1.5	1.7	1.7	1.7	1.7	1.7	1.7	1.7	1.7	1.7	1.7		
$R_0$ [m]	0.83	0.83	0.86	0.86	0.86	0.86	0.86	0.86	0.93	0.93	0.93	0.93	0.93	0.93	0.93	0.93	0.93	0.93		
Elongation $\kappa$	2.60	2.60	2.45	2.45	2.55	2.55	2.60	2.60	2.75	2.75	2.75	2.75	2.75	2.75	2.75	2.75	2.75	2.75		
$P_{NBI}$ [MW]	4.90	4.90	5.90	5.90	6.30	6.30	6.0	6.0	10.0	10.0	5.0	5.0	10.0	10.0	15.0	15.0	6.0	6.0		
$P_{RF}$ [MW]	0.00	0.00	0.00	0.00	0.00	0.00	0.0	0.0	0.0	0.0	0.0	0.0	0.0	0.0	4.0	4.0	0.0	0.0		
$P_{ind}$ [MW]	0.15	0.15	0.25	0.25	0.47	0.47	0.15	0.24	0.00	0.00	0.05	0.08	0.23	0.37	0.10	0.18	0.00	0.00		
$P_{heat}$ [MW]	5.05	5.05	6.15	6.15	6.77	6.77	6.15	6.24	10.0	10.0	5.05	5.08	10.2	10.4	19.1	19.2	6.00	6.00		
Greenwald fraction	0.61	0.61	0.95	0.95	0.73	0.73	0.5	1.0	0.50	1.00	0.50	1.00	0.50	1.00	0.50	1.00	0.50	1.00		
$n_e$ -bar [ $10^{20} m^{-3}$ ]	0.44	0.44	0.85	0.85	0.85	0.85	0.52	1.03	0.54	1.00	0.44	0.88	0.98	1.96	0.98	1.96	0.73	1.43		
Volume avg. $T_e$ [keV]	0.62	0.61	0.62	0.57	0.84	0.85	0.96	0.67	1.50	1.01	1.09	0.75	1.80	1.25	2.19	1.51	2.63	1.59		
Volume avg. $T_i$ [keV]	0.68	0.67	0.64	0.59	0.90	0.90	1.08	0.68	1.68	1.03	1.22	0.77	2.02	1.27	2.45	1.54	2.94	1.62		
$T_i$ peaking factor	1.47	1.46	1.47	1.55	1.47	1.38	1.47	1.47	1.47	1.47	1.47	1.47	1.47	1.47	1.47	1.47	1.47	1.47		
$T_e$ peaking factor	1.44	1.42	1.44	1.46	1.44	1.43	1.44	1.44	1.44	1.44	1.44	1.44	1.44	1.44	1.44	1.44	1.44	1.44		
$n_e$ peaking factor	1.35	1.26	1.35	1.48	1.35	1.31	1.35	1.35	1.35	1.35	1.35	1.35	1.35	1.35	1.35	1.35	1.35	1.35		
$P_{thermal}$ peaking factor	1.83	1.70	1.83	2.08	1.83	1.72	1.83	1.83	1.83	1.83	1.83	1.83	1.83	1.83	1.83	1.83	1.83	1.83		
$p_{fast}$ peaking factor	4.57	4.82	4.57	4.40	4.57	4.49	4.57	4.57	4.57	4.57	4.57	4.57	4.57	4.57	4.57	4.57	4.57	4.57		
$p_{total}$ peaking factor	2.69	2.65	2.20	2.40	2.22	2.17	2.93	2.25	3.18	2.49	3.02	2.30	2.43	2.03	2.72	2.15	2.41	2.05		
Normalized toroidal rotation	1.14	1.14	0.62	0.59	1.53	1.53	1.00	1.00	2.32	2.29	0.99	0.99	2.55	2.55	4.22	4.21	1.85	1.72		
$I_p$ flat-top time [s]	1.32	1.32	1.00	1.00	0.39	0.39	1.0	1.0	5.0	5.0	10.0	10.0	5.0	5.0	0.3	0.3	5.0	5.0		
$\tau_{current-redistribution}$ [s]	0.26	0.26	0.28	0.24	0.47	0.48	0.51	0.29	1.04	0.57	0.65	0.37	1.37	0.79	1.83	1.05	2.41	1.13		
# redistribution times	5.1	5.1	3.5	4.1	0.8	0.8	2.0	3.4	4.8	8.7	15	27	3.6	6.3	0.2	0.3	2.1	4.4		
Stored energy [MJ]	0.19	0.19	0.28	0.27	0.39	0.41	0.36	0.33	0.68	0.54	0.36	0.33	0.96	1.08	1.35	1.37	1.04	1.00		
$\beta_N$ [%mT/MA]	4.8	4.9	5.5	5.3	4.9	5.1	6.0	5.6	5.4	4.6	4.7	4.2	4.2	4.7	5.9	5.9	6.0	6.0		
$\beta_T$ [%]	14.5	14.9	20.1	19.7	22.0	22.9	21.6	20.2	10.3	8.2	9.8	8.8	14.7	16.4	20.5	20.8	15.8	15.3		
$q^*$	4.3	4.3	3.2	3.2	2.9	2.9	3.5	3.5	6.8	7.3	6.2	6.2	3.7	3.7	3.7	3.7	5.0	5.1		
Fast-ion $\beta$ fraction	0.31	0.30	0.14	0.14	0.14	0.16	0.40	0.15	0.49	0.24	0.43	0.17	0.22	0.07	0.32	0.12	0.21	0.08		
$v_e^* [\times 10^{12}]$ ( $q=2, \epsilon=A^{-1}$ )	6.4	6.5	10.7	13.0	7.7	7.4	2.8	11.6	1.4	5.7	2.1	9.0	1.7	7.3	1.2	5.0	0.6	3.3		
$v_e^* [\times 10^{12}]$ ( $q=q^*, \epsilon=A^{-1}$ )	13.6	13.8	17.0	20.7	11.1	10.7	4.8	20.1	4.7	20.9	6.7	28.0	3.3	13.6	2.2	9.3	1.5	8.5		
Bootstrap fraction $f_{BS}$	0.44	0.41	0.48	0.50	0.38	0.37	0.40	0.53	0.61	0.85	0.55	0.72	0.41	0.54	0.49	0.65	0.79	0.94		
NBI CD fraction $f_{NBI-CD}$	0.16	0.17	0.07	0.06	0.08	0.07	0.17	0.06	0.38	0.15	0.21	0.07	0.14	0.05	0.25	0.09	0.21	0.07		
Non-inductive fraction $f_{NCD}$	0.60	0.59	0.55	0.56	0.47	0.44	0.57	0.59	0.99	1.00	0.75	0.79	0.54	0.59	0.74	0.74	1.00	1.00		
$I_p$ ramp-up time [s]	0.16	0.15	0.20	0.21	0.29	0.34	0.2	0.2	0.55	0.51	0.45	0.45	1.00	1.00	1.00	1.00	0.75	0.73		
$I_p$ ramp-down time [s]	0.08	0.04	0.10	0.02	0.14	0.09	0.1	0.1	0.28	0.26	0.23	0.23	0.50	0.50	0.50	0.50	0.38	0.37		
Total $I_p$ duration [s]	1.56	1.51	1.31	1.23	0.82	0.82	1.3	1.3	5.8	5.8	10.7	10.7	6.5	6.5	1.8	1.8	6.1	6.1		
Max. TF flat-top time [s]	1.60	1.60	1.48	1.48	1.17	1.17	1.1	1.1	6.6	6.6	11.7	11.7	6.6	6.6	6.6	6.6	6.6	6.6		
Fraction TF flat-top used	0.97	0.94	0.88	0.83	0.70	0.70	1.23	1.23	0.88	0.87	0.91	0.91	0.98	0.98	0.27	0.27	0.93	0.92		
Total OH flux available [Wb]	0.75	0.75	0.75	0.75	0.75	0.75	0.75	0.75	2.10	2.10	2.10	2.10	2.10	2.10	2.10	2.10	2.10	2.10		
$I_p$ ramp-up flux [Wb]	0.25	0.25	0.34	0.34	0.48	0.48	0.37	0.37	0.44	0.41	0.36	0.36	0.80	0.80	0.80	0.80	0.60	0.58		
Surface voltage [V]	0.21	0.23	0.28	0.31	0.36	0.37	0.15	0.24	0.00	0.00	0.06	0.09	0.12	0.18	0.05	0.09	0.00	0.00		
Total flat-top flux [Wb]	0.50	0.50	0.41	0.41	0.27	0.27	0.38	0.38	1.66	1.69	1.74	1.74	1.30	1.30	1.30	1.30	1.50	1.52		
Flat-top flux used [Wb]	0.28	0.32	0.28	0.31	0.14	0.14	0.15	0.24	0.0	0.0	0.60	0.88	0.58	0.92	0.01	0.03	0.0	0.0		
Fraction OH flux used	0.72	0.76	0.82	0.87	0.83	0.83	0.69	0.81	0.21	0.19	0.46	0.59	0.66	0.82	0.39	0.39	0.28	0.28		
Power fraction to divertor	0.50	0.50	0.50	0.50	0.50	0.50	0.5	0.5	0.50	0.50	0.50	0.50	0.50	0.50	0.50	0.50	0.50	0.50		
$R_{strike-point}$ [m]	0.40	0.40	0.40	0.40	0.40	0.40	0.40	0.40	0.50	0.50	0.50	0.50	0.50	0.50	0.50	0.50	0.50	0.50		
SOL heat-flux width [mm]	15.9	15.9	10.5	10.5	6.0	6.0	9.2	9.2	7.9	8.9	10.9	10.9	3.0	3.0	3.0	3.0	4.8	5.0		
Poloidal flux expansion	22	22	22	22	22	22	22	22	22	22	22	22	62	62	62	62	22	22		
Peak heat flux [MW/m <sup>2</sup> ]	2.9	2.9	5.3	5.3	10.1	10.1	6.0	6.1	9.1	8.1	3.4	3.4	8.7	8.8	16.2	16.2	9.0	8.6		
Time to $T_{PFC} = 1200^\circ C$ [s]	61	61	18	18	4.9	4.9	13.7	13.3	6.1	7.6	44	44	6.7	6.5	1.9	1.9	6.1	6.7		
Fraction of $T_{PFC}$ limit	0.03	0.02	0.07	0.07	0.17	0.17	0.10	0.10	0.96	0.76	0.24	0.24	0.97	1.00	0.94	0.95	1.00	0.91		

**Table 1.** (Left) Comparison between NSTX 0-D scaling model and TRANSP analysis of representative NSTX experimental discharges, (middle white columns) parameters for NSTX Reference scenario at two density values, and (right) projected parameters for NSTX Upgrade scenarios.



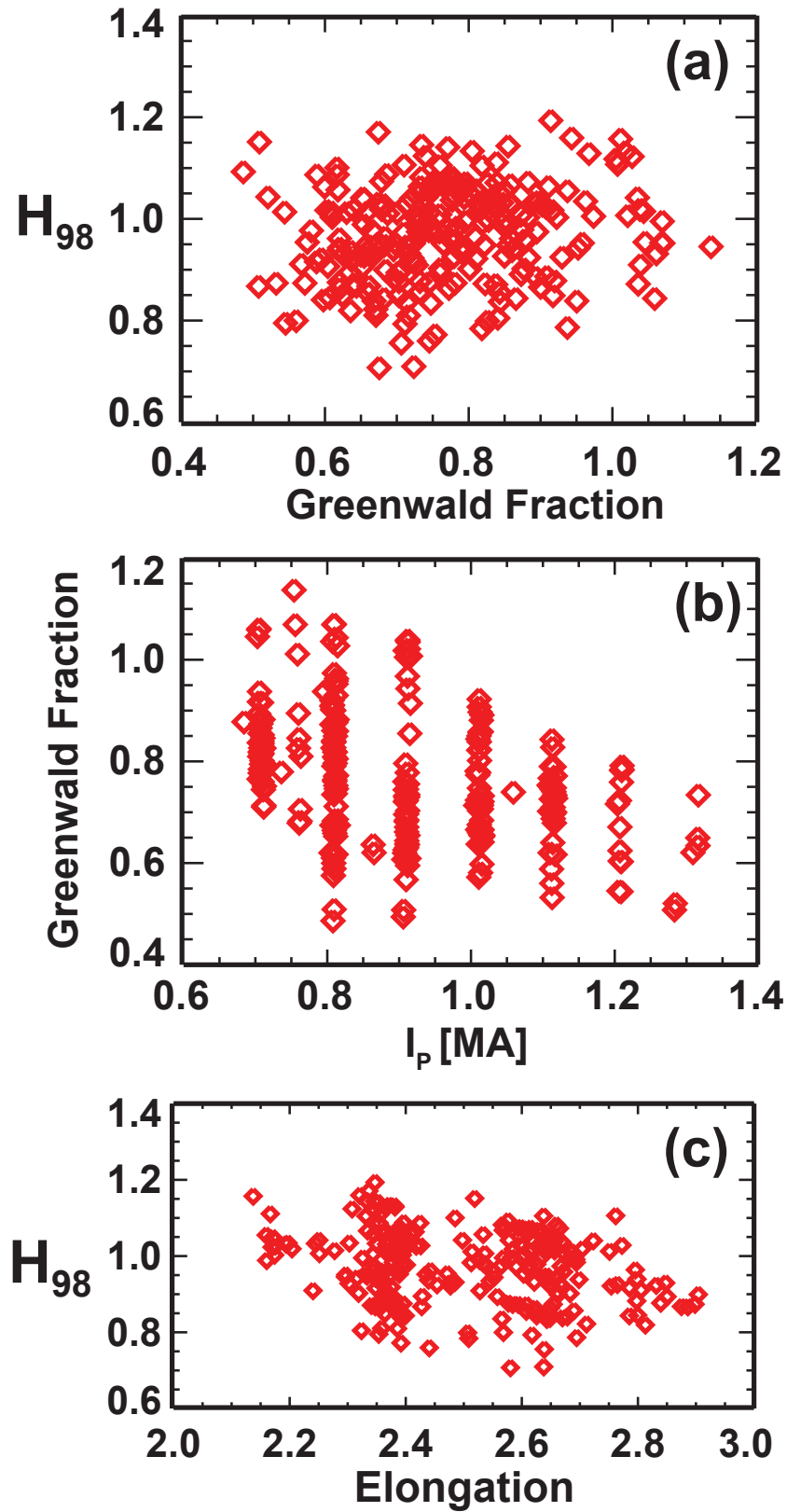


**Figure 3.** (a) NSTX H-mode thermal confinement multiplier  $H_{98}$  relative to the ITER H-98(y,2) confinement scaling versus Greenwald density fraction, (b) Greenwald fraction versus plasma current, and (c)  $H_{98}$  versus elongation.

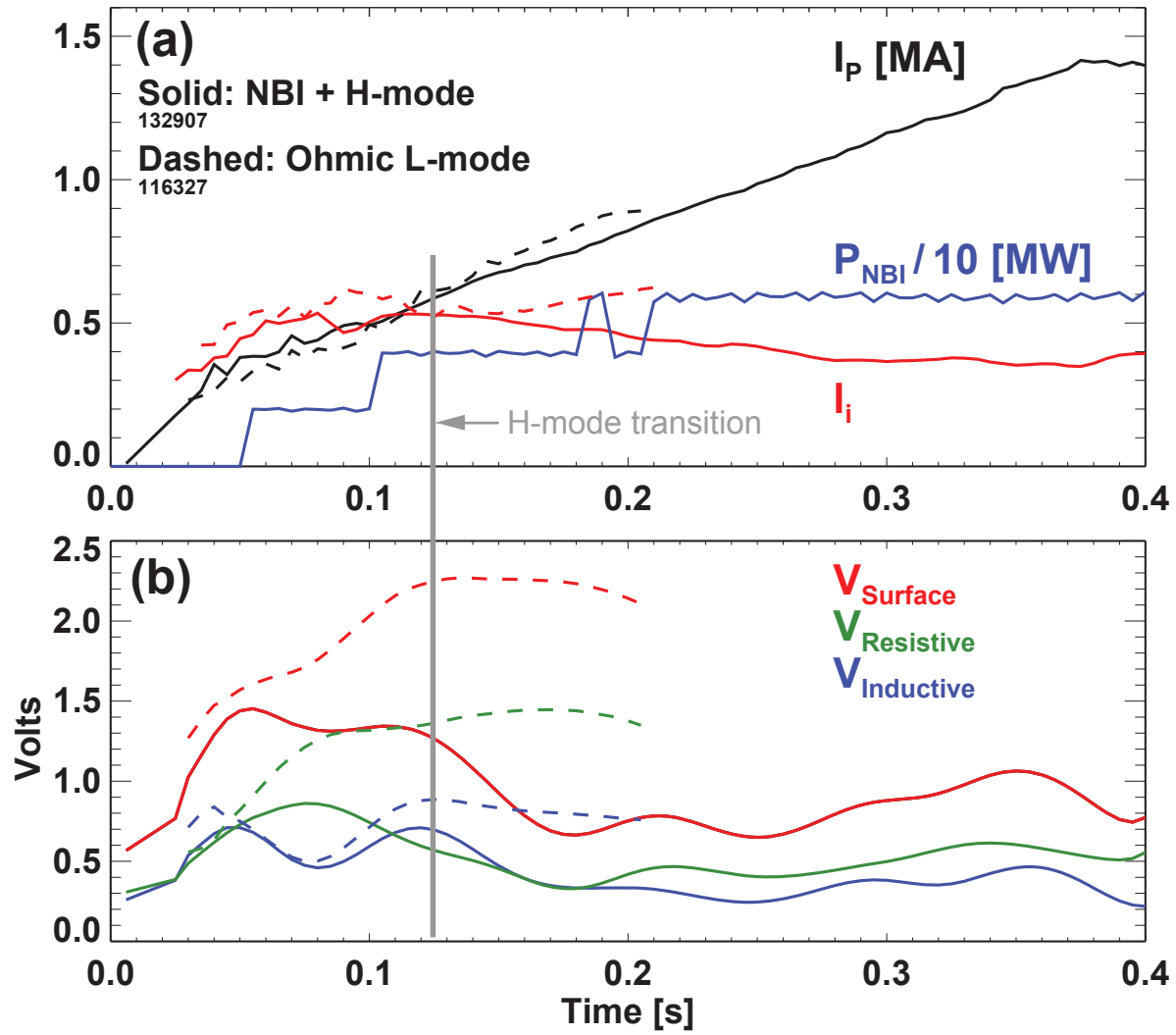


**Figure 4.** Comparison of plasma current ramp-up evolution for NSTX ohmic plasmas (dashed) versus early-NBI-heated H-mode plasmas (solid) including: (a) plasma current (black), neutral beam injection power (blue), and internal inductance (red), and (b) surface voltage evolution (red) including the resistive (green) and inductive (blue) contributions.

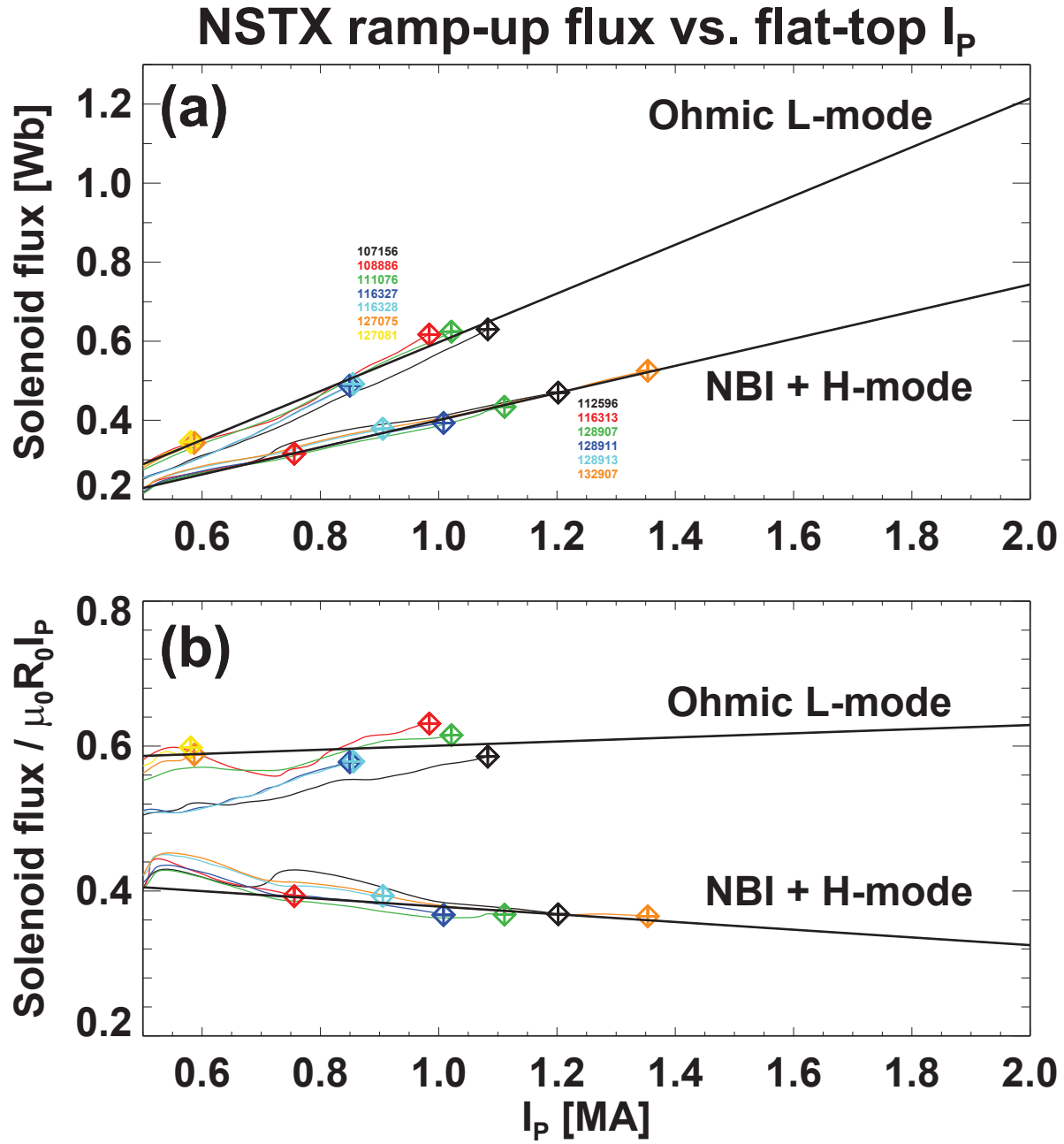


**Figure 5.** (a) Solenoid flux consumed for break-down and ramp-up vs. plasma current flat-top value, and (b) normalized solenoid flux consumed vs. current flat-top value for NSTX ohmic and early-NBI-heated H-mode plasmas.

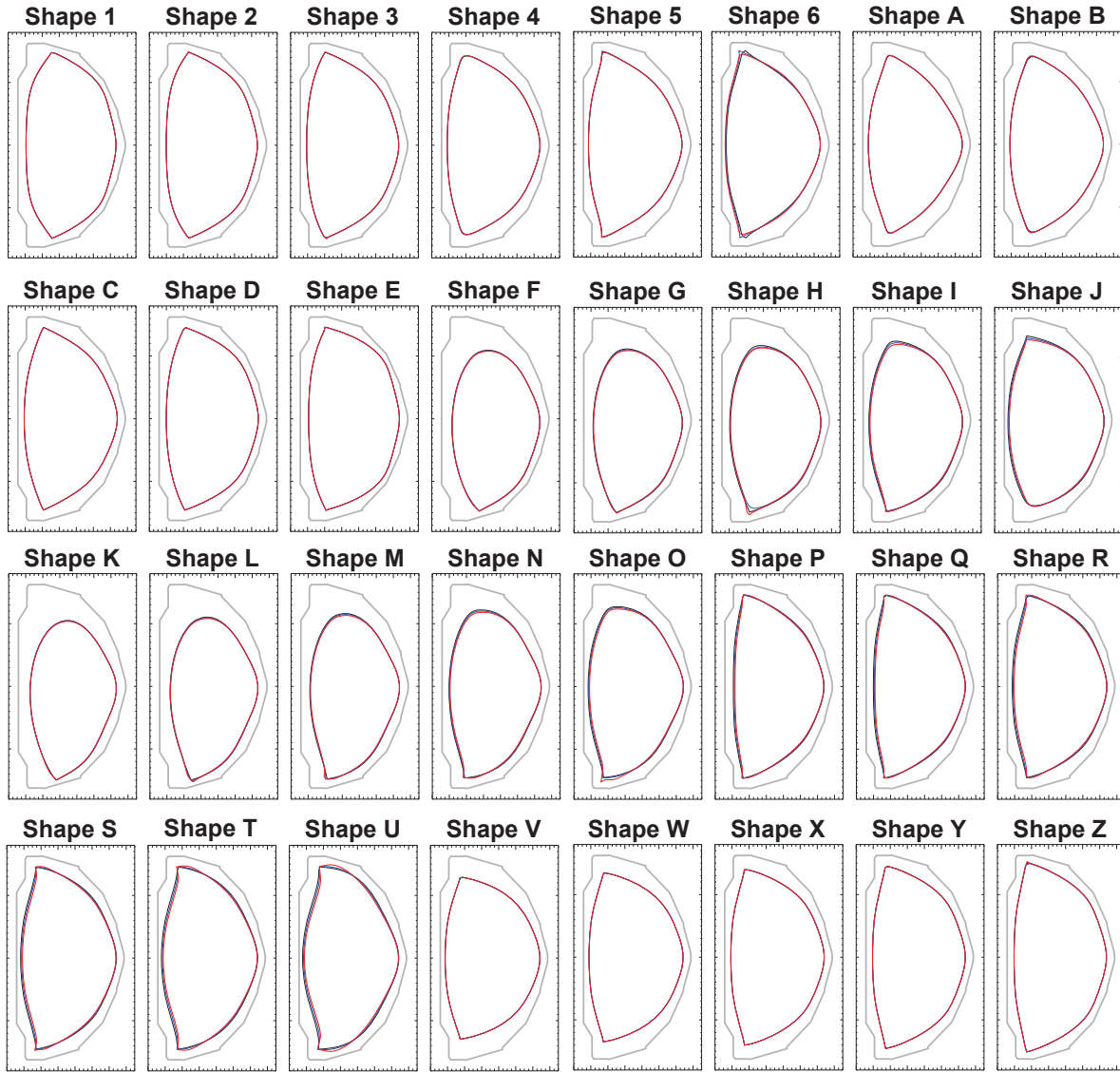


**Figure 6.** Plasma boundaries of free-boundary equilibria used for assessing PF coil current requirements in NSTX Upgrade. Each plot is a superposition of three boundary plots, i.e. one for each OH power supply current state assessed: 0kA and  $\pm 24$ kA.

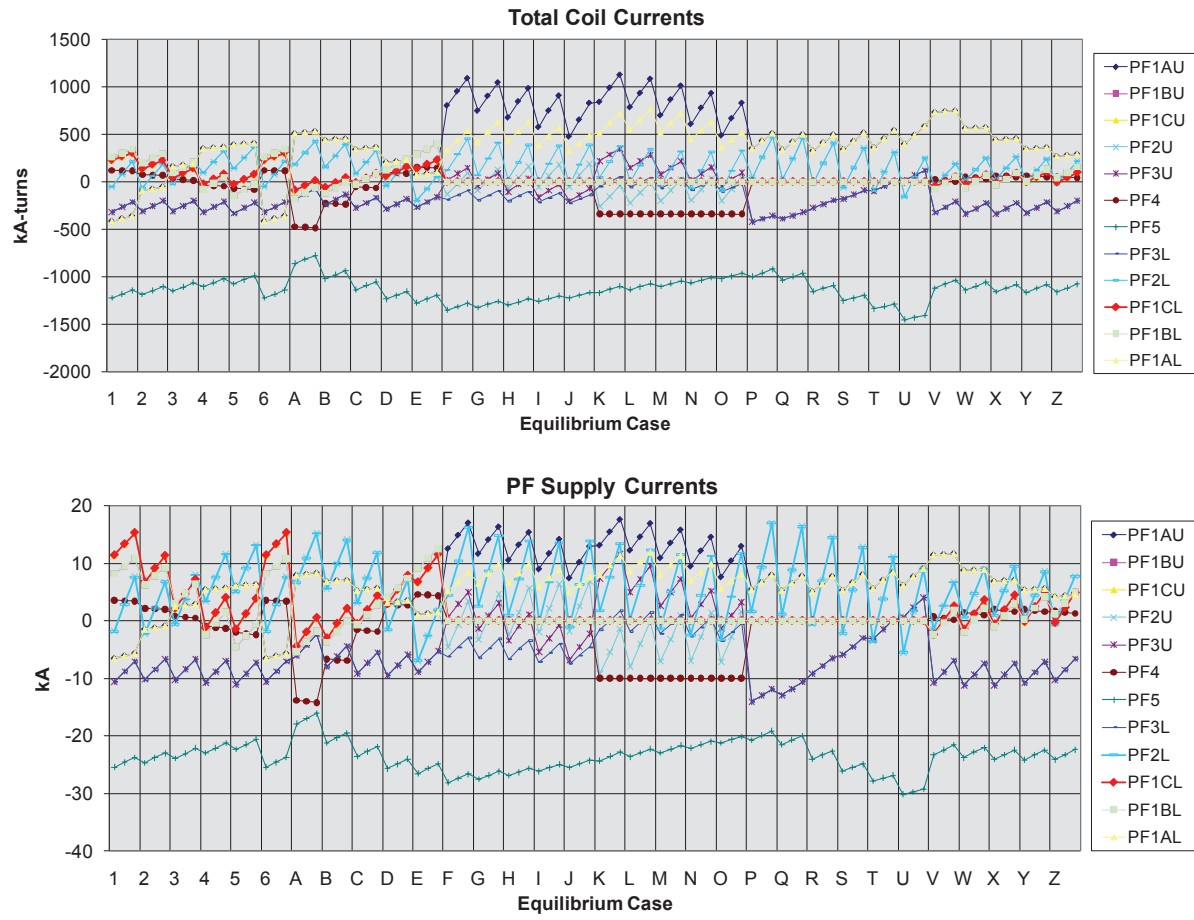


**Figure 7.** Total coil current (top) and power supply current (bottom) required for each of the 96 reference 2MA Upgrade equilibria.

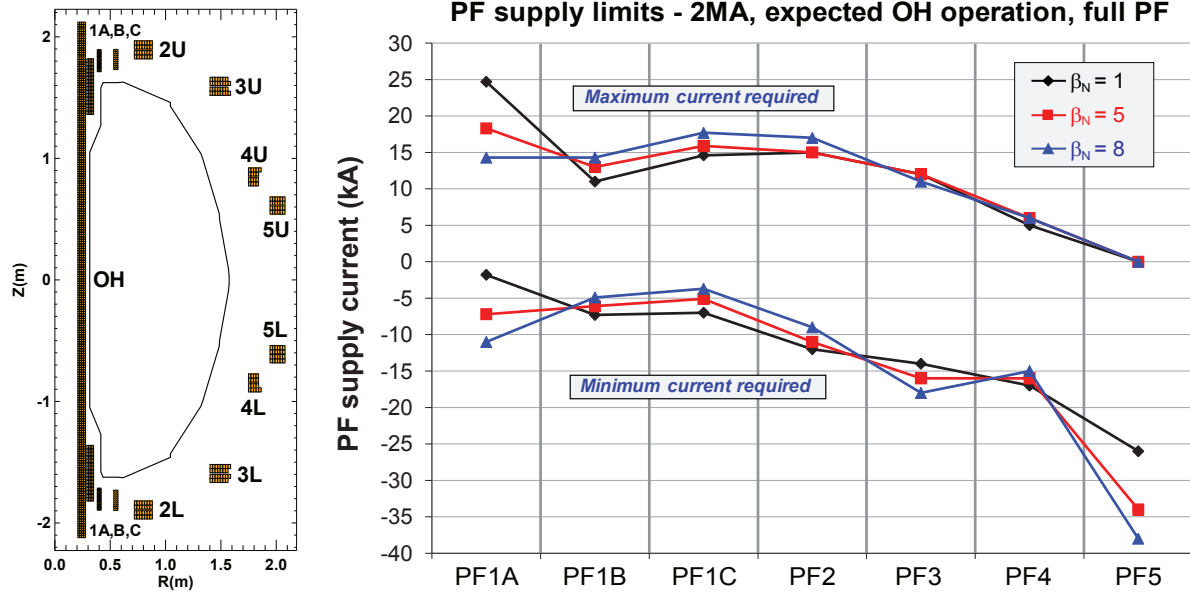


**Figure 8.** (Left) PF and OH coil current locations, sizes, and limiter boundary and (right) minimum and maximum PF coil current vs  $\beta_N$ .

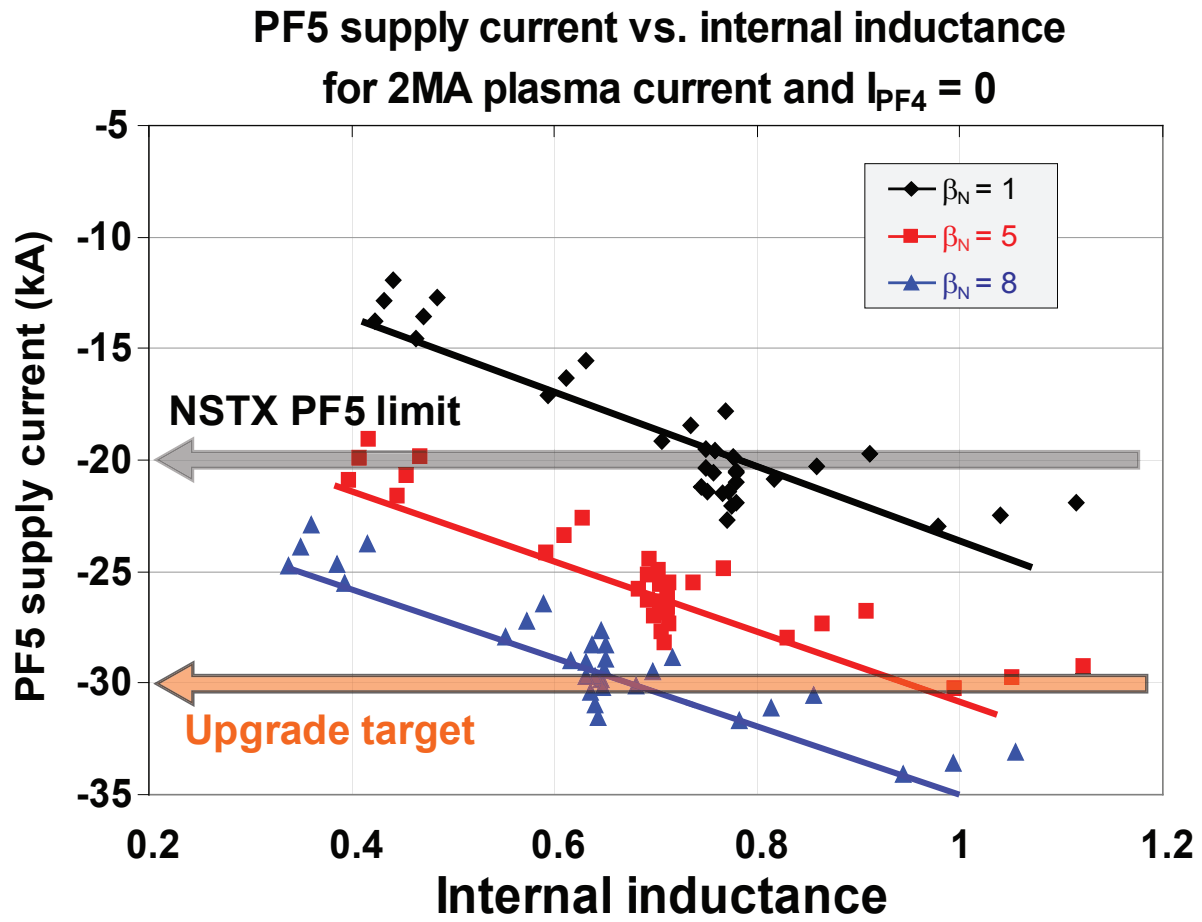
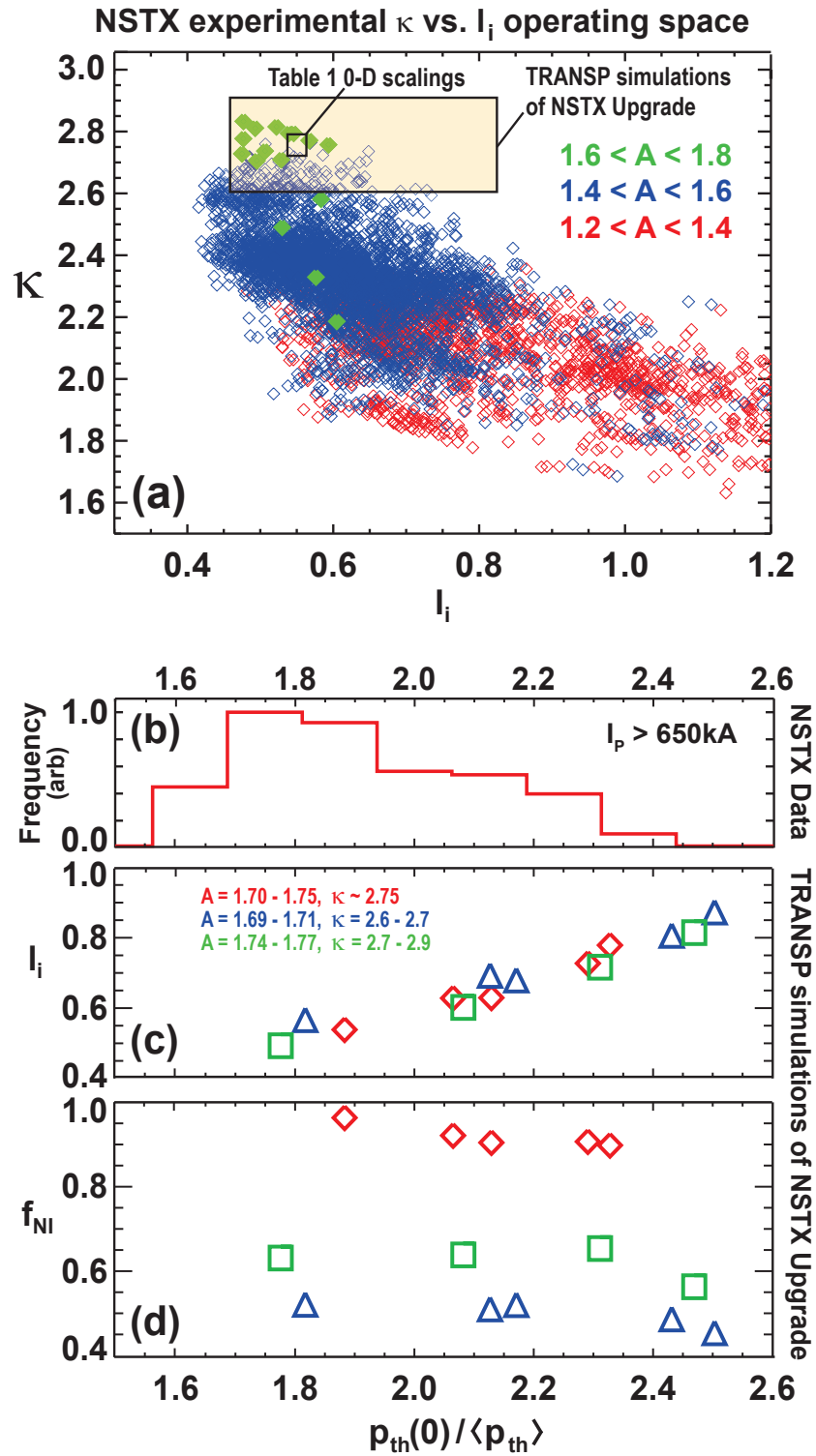


**Figure 9.** PF5 vertical field coil current required to support 2MA plasmas as a function of internal inductance and normalized beta.

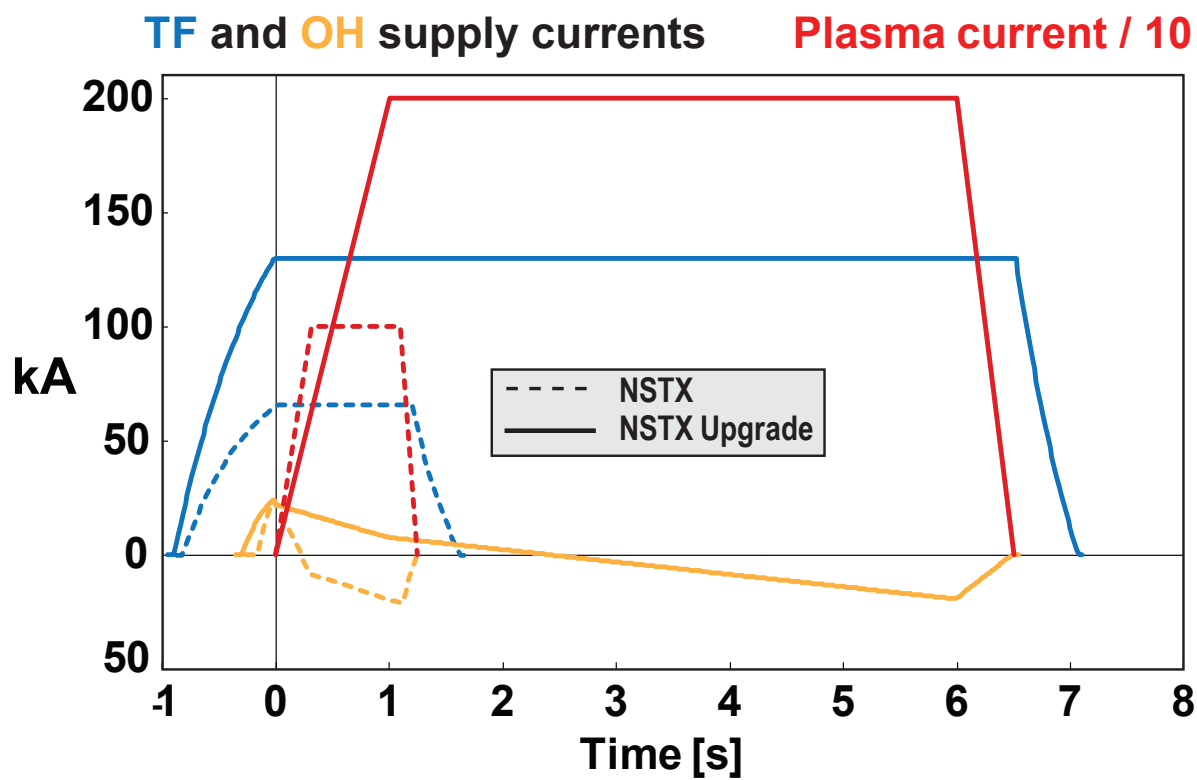
Coil	NR	NZ	Turns	Equilibrium multiplier	Min power supply kA	Max power supply kA	Min coil MA turns	Max coil MA turns
OH	4.0	221	884	1.0	-24.0	24.0	-21.2	21.2
PF1AU,L	4.0	16	64	1.1	-7.2	18.3	-0.46	1.17
PF1BU,L	2.0	16	32	1.1	-6.0	13.0	-0.19	0.42
PF1CU,L	2.0	10	20	1.1	-5.0	15.9	-0.10	0.32
PF2U,L	7.0	4	28	1.1	-11.0	15.0	-0.31	0.42
PF3U,L	7.5	4	30	1.1	-16.0	12.0	-0.48	0.36
PF4	8.5	4	34	1.1	-16.0	6.0	-0.54	0.20
PF5	6.0	8	48	1.1	-34.0	0.0	-1.63	0.00

**Table 2.** NSTX Upgrade OH and PF coil number of radial layers (NR), vertical layers (NZ), total turns-count, power supply current multiplier with respect to the required equilibrium current, and minimum and maximum power supply and total coil currents.

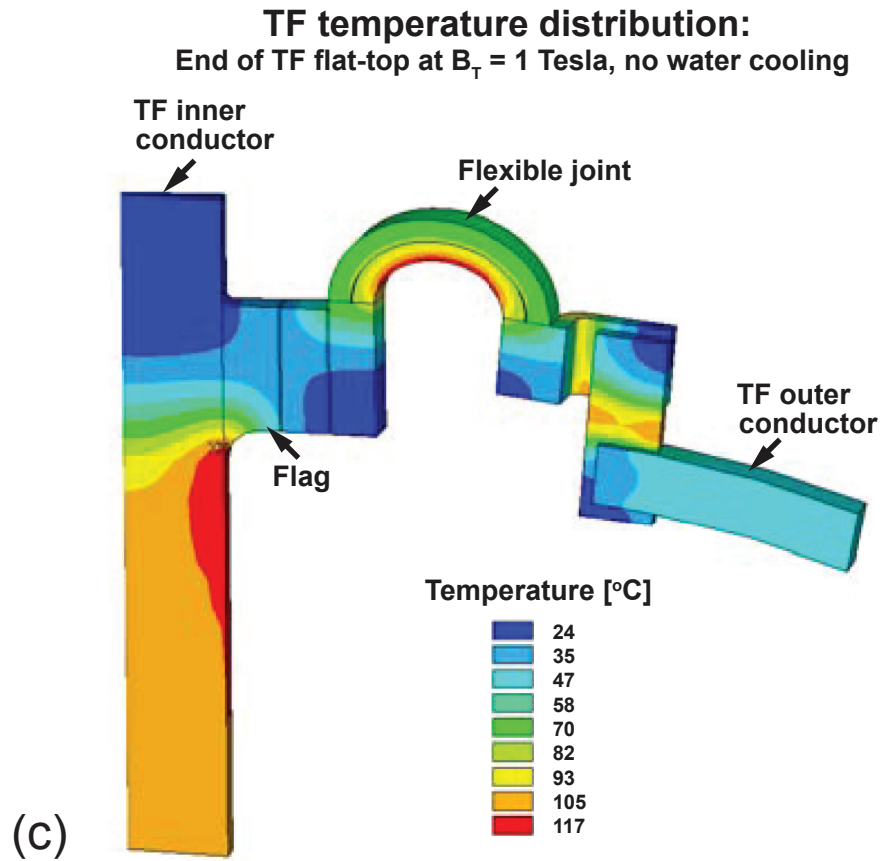
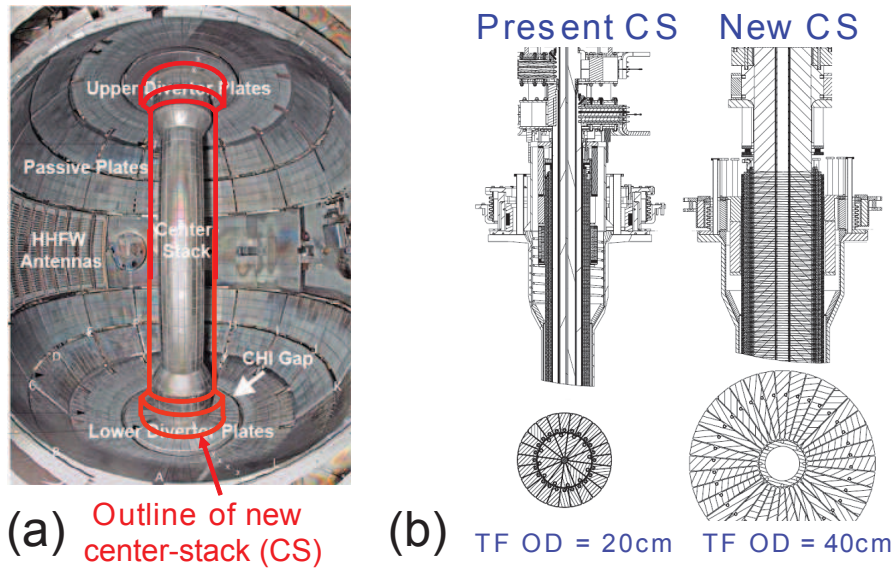




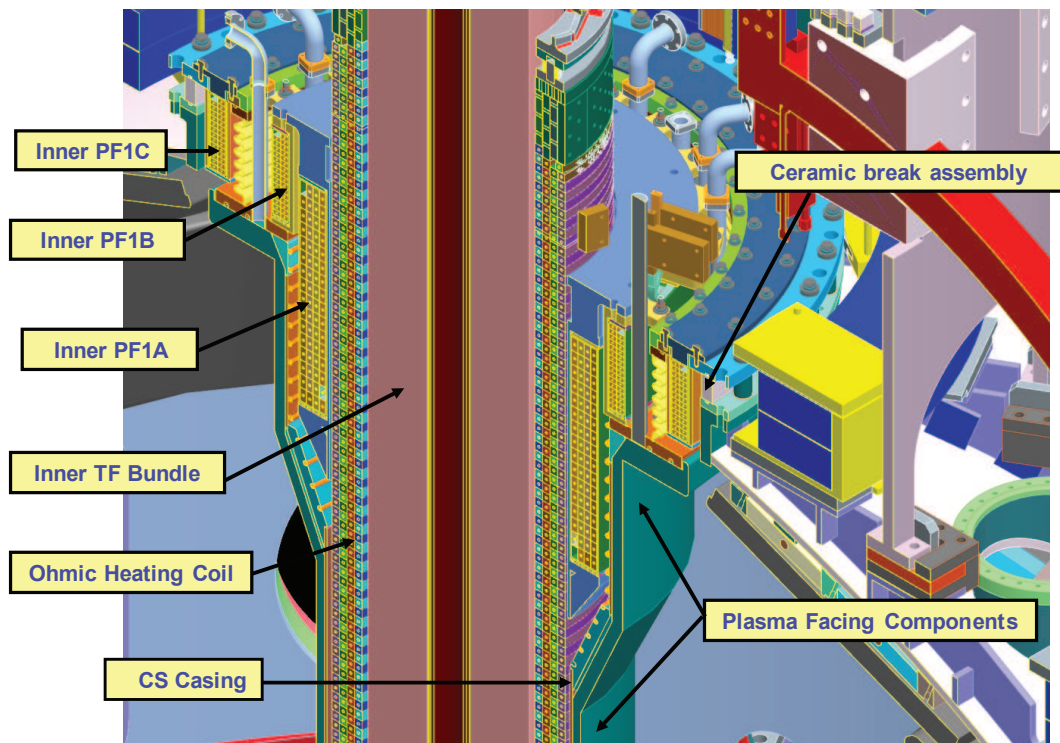
**Figure 10.** (a) NSTX experimental  $\kappa$  versus  $l_i$  operating space sorted by aspect ratio, (b) histogram of thermal pressure profile peaking factor in NSTX, (c)  $l_i$  and (d) non-inductive current drive fraction  $f_{NI}$  versus thermal pressure profile peaking factor for TRANSF simulations of NSTX Upgrade. The yellow shaded rectangle in (a) indicates the approximate range of  $\kappa$  and  $l_i$  values for the TRANSF simulations of NSTX Upgrade.



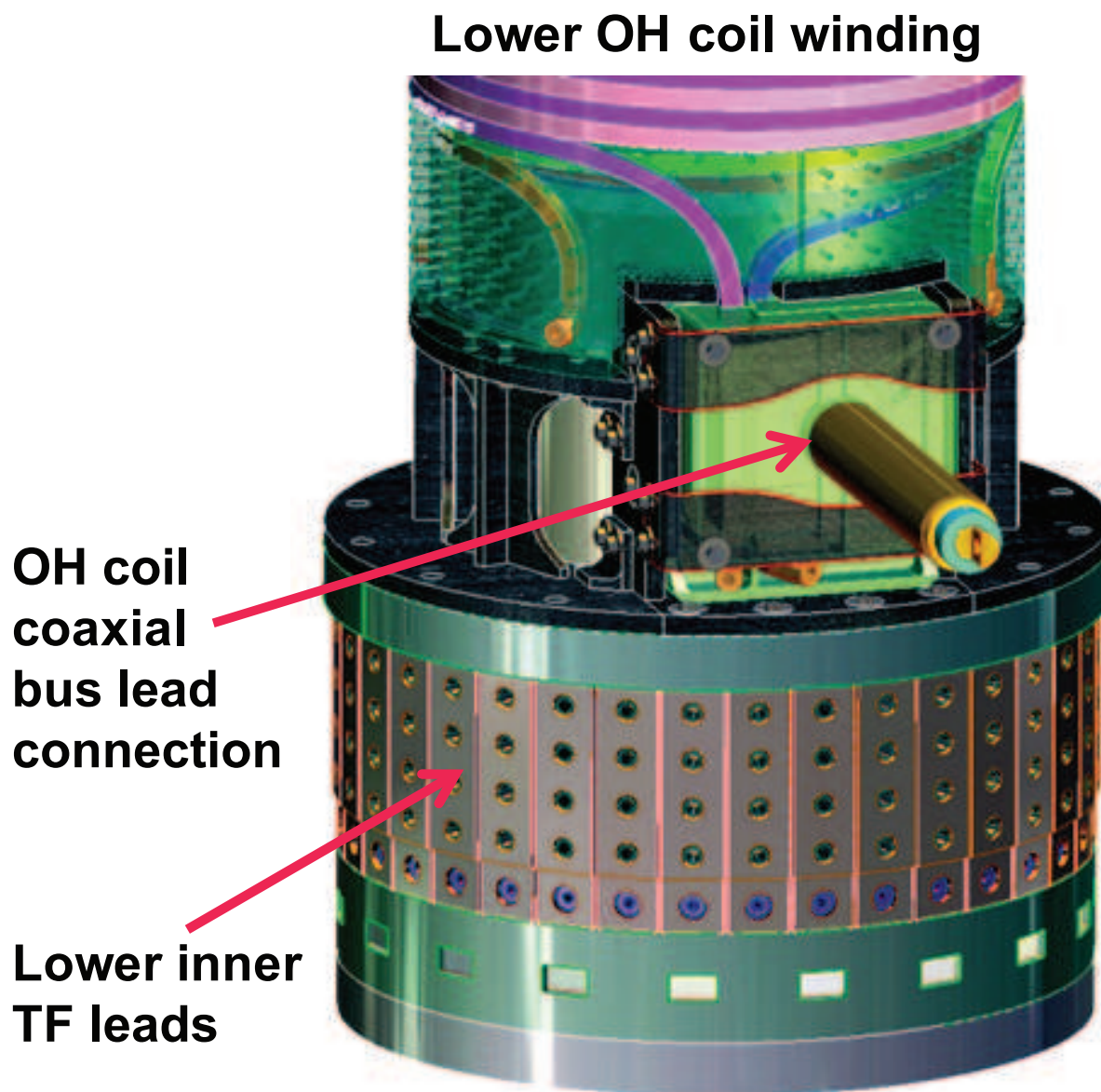
**Figure 11.** Comparison of toroidal field (TF), ohmic heating (OH), and plasma current waveforms for plasmas operated at the maximum toroidal field capabilities of NSTX (0.55T) and NSTX Upgrade (1T).



**Figure 12.** (a) Outlines and (b) cross-sections of the present and new center-stack for comparing the TF conductor diameters, and (c) temperature distribution at end of TF flat-top for  $B_T = 1$ T operation and no TF conductor cooling during the pulse.

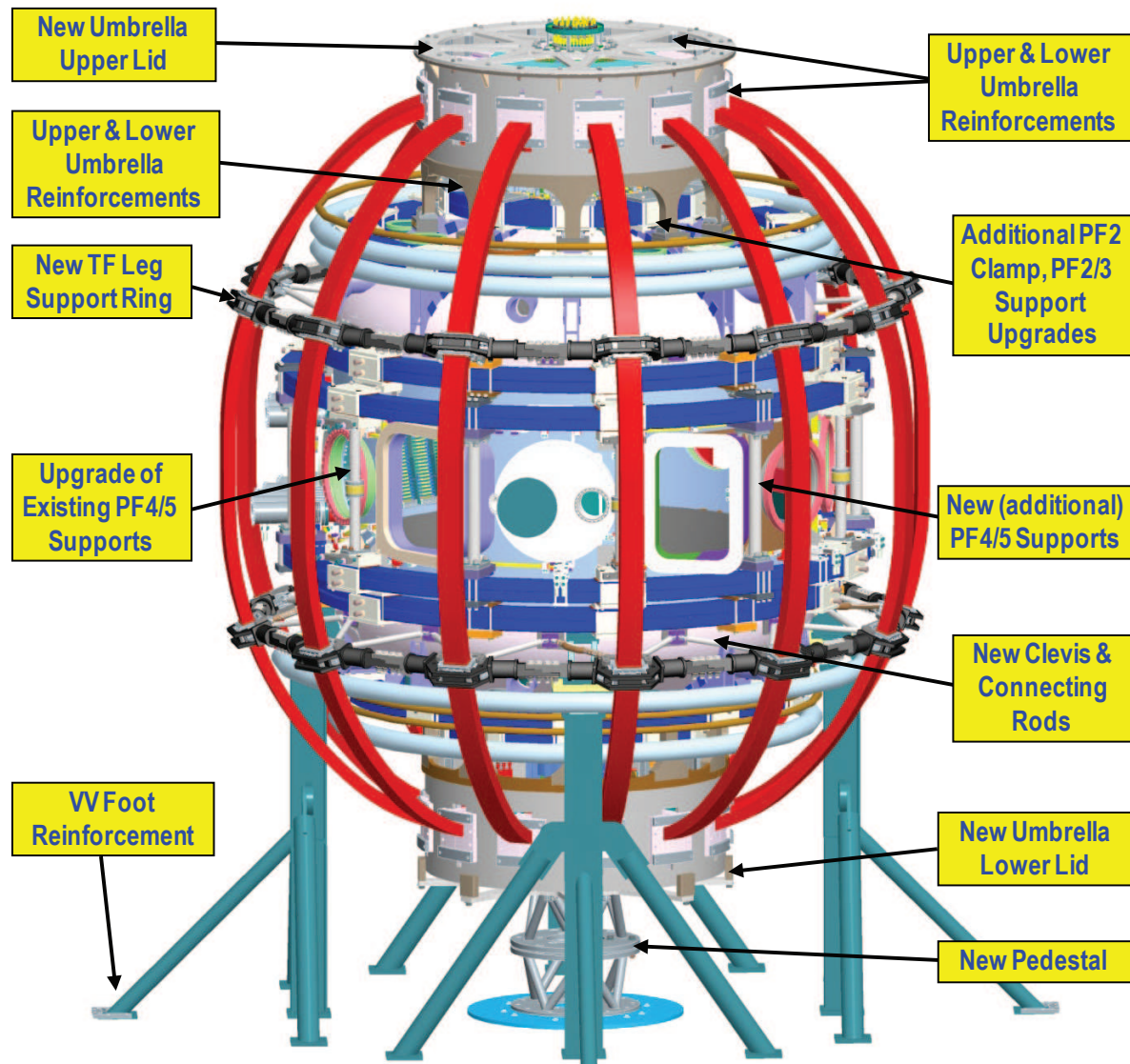


**Figure 13.** Detailed cross-section of the Upgrade center-stack showing the TF, OH, and divertor PF coils, and the CHI insulator and PFC boundaries.

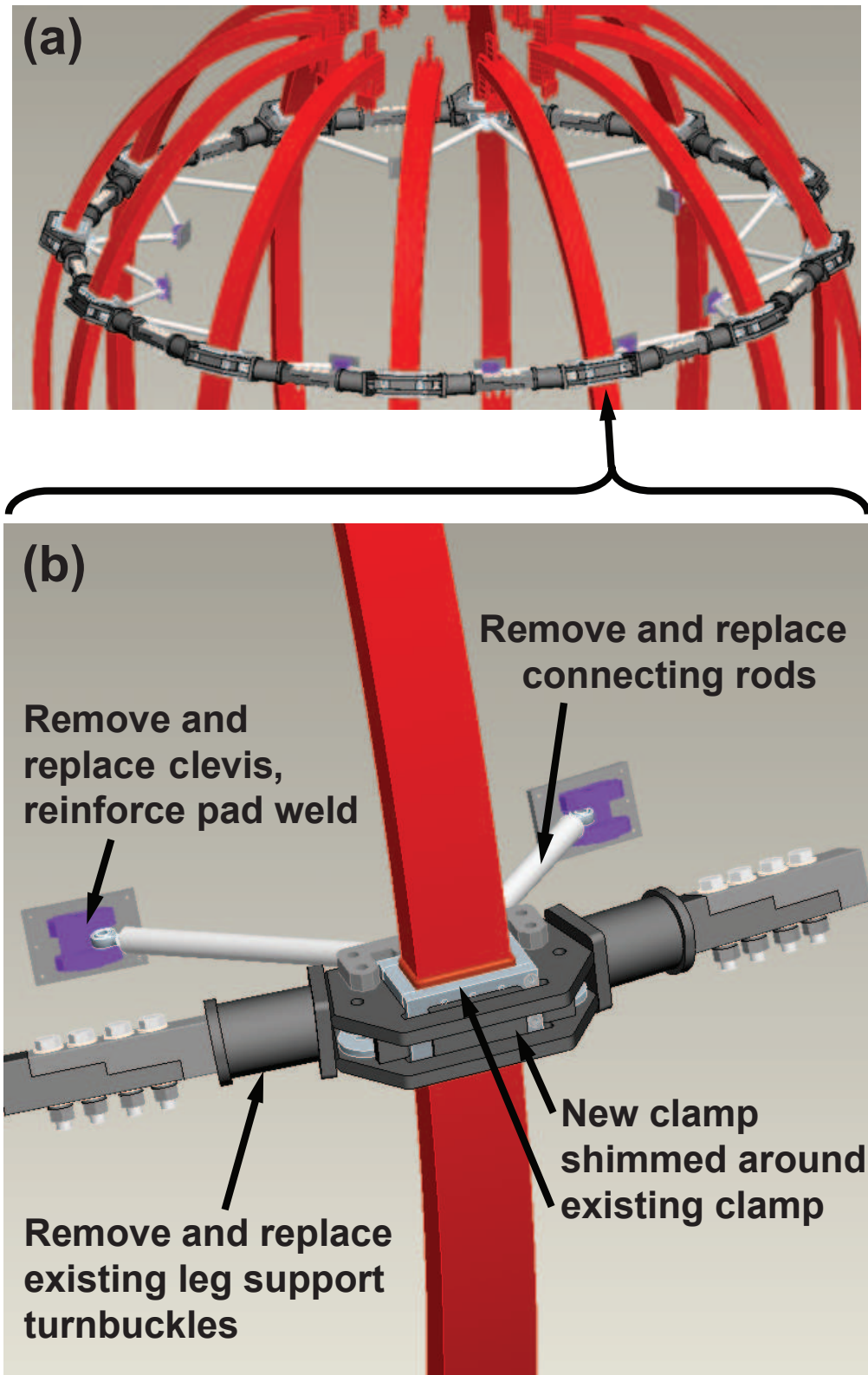


**Figure 14.** Design drawing of the lower OH coil winding area including the coaxial bus lead connection and lower inner TF leads.

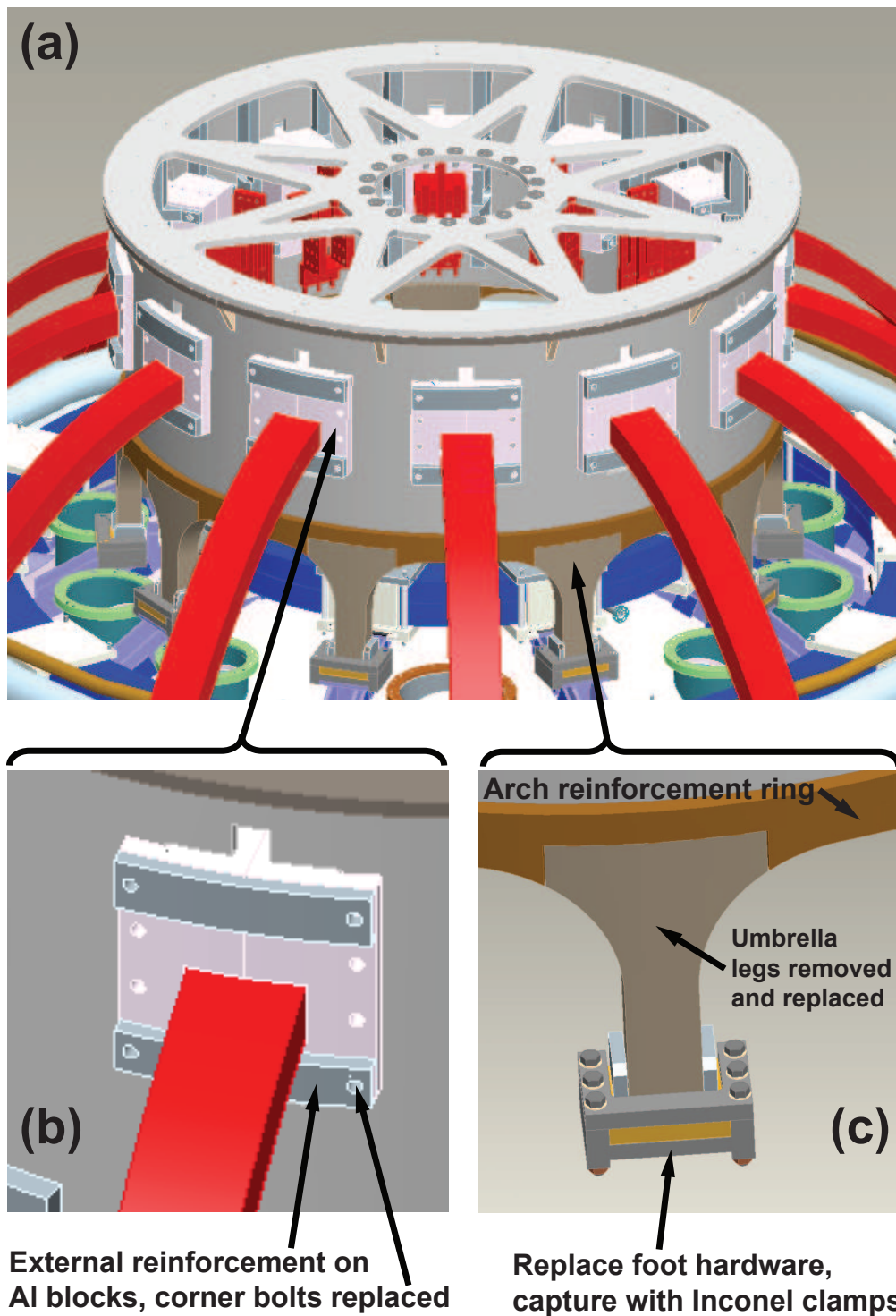




**Figure 15.** Vessel reinforcements and other modifications required for handling the increased forces associated with higher field and current of NSTX Upgrade.

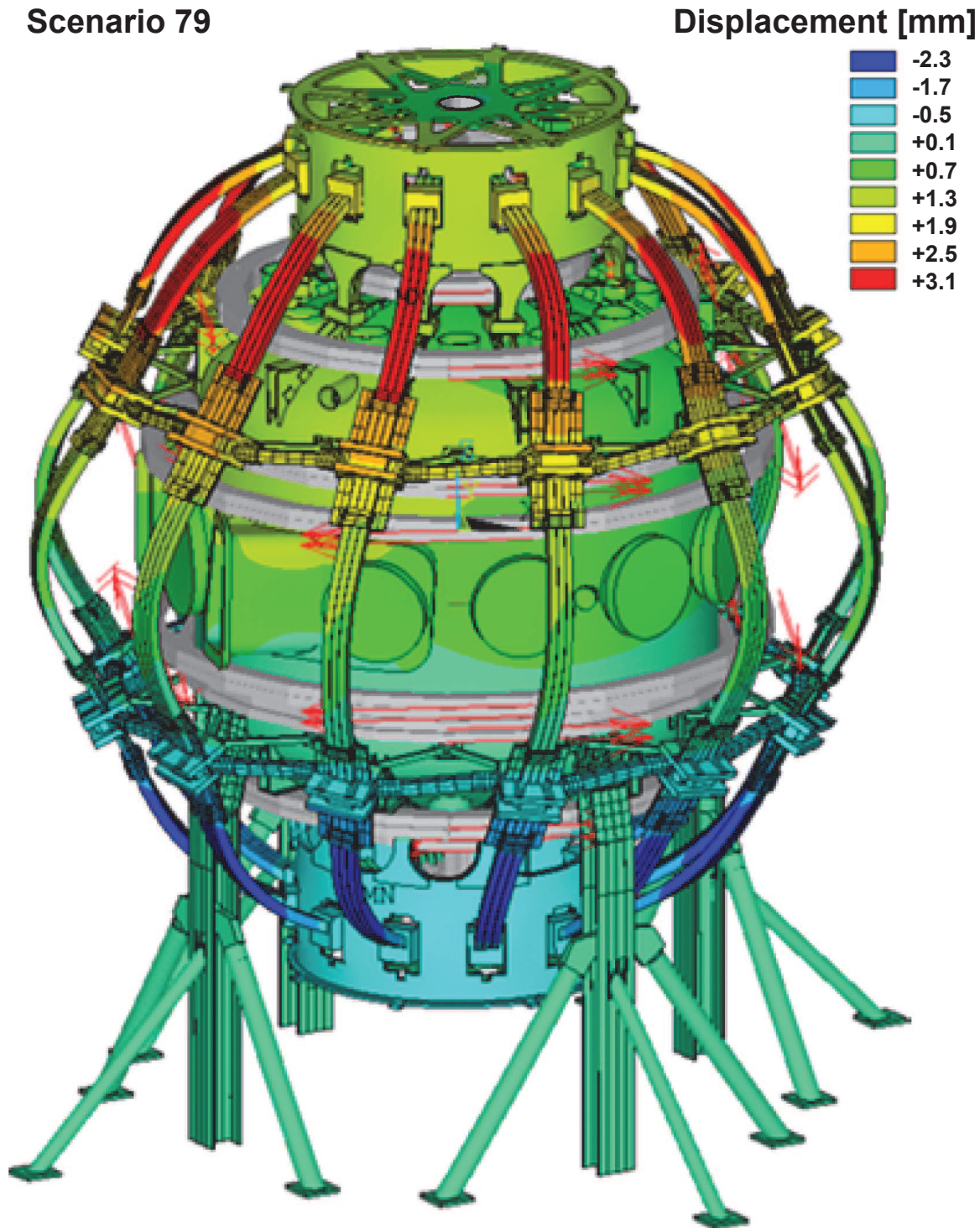


**Figure 16.** (a) Outer TF coils (red) and new upper attachment hardware (gray, silver, purple), and (b) new clevises, clevis pads, connecting rods, clamps, and turnbuckle replacements used to strengthen the inter-coil support structure and the attachment of the outer TF coils to the NSTX Upgrade vacuum vessel.



**Figure 17.** (a) Top of NSTX Upgrade showing the cylindrical "umbrella" structure where the outer TF coils (red) connect to the top of the vacuum vessel, (b) reinforcement strips to be attached to the aluminum blocks which connect the TF coils to the umbrella cylinder, and (c) the new umbrella arch reinforcement ring, new umbrella legs to be welded in place, and new attachments for connecting the umbrella feet to the vacuum vessel.



**Scenario 79**

**Figure 18.** Exaggerated displacement of the outer TF coils, vacuum vessel, umbrella structure, and other components of NSTX Upgrade resulting from the highest force and torque equilibrium (scenario 79) of the 96 equilibria used for designing the enhancements of the support structures. The color key in the upper right-hand corner of the figure indicates the displacement in millimeters, and the red arrows on the PF coils indicate the direction of current in the coil.

Acceleration Voltage [kV]	MW per Source	MW per Beamline	Pulse Length [s]
65	1.1	3.2	8
70	1.3	3.8	7
75	1.5	4.5	6
80	1.7	5.1	5
85	1.9	5.8	4
90	2.1	6.4	3
95	2.4	7.1	2
100	2.6	7.7	1.5
105	2.8	8.4	1.25
110	3.0	9.0	1

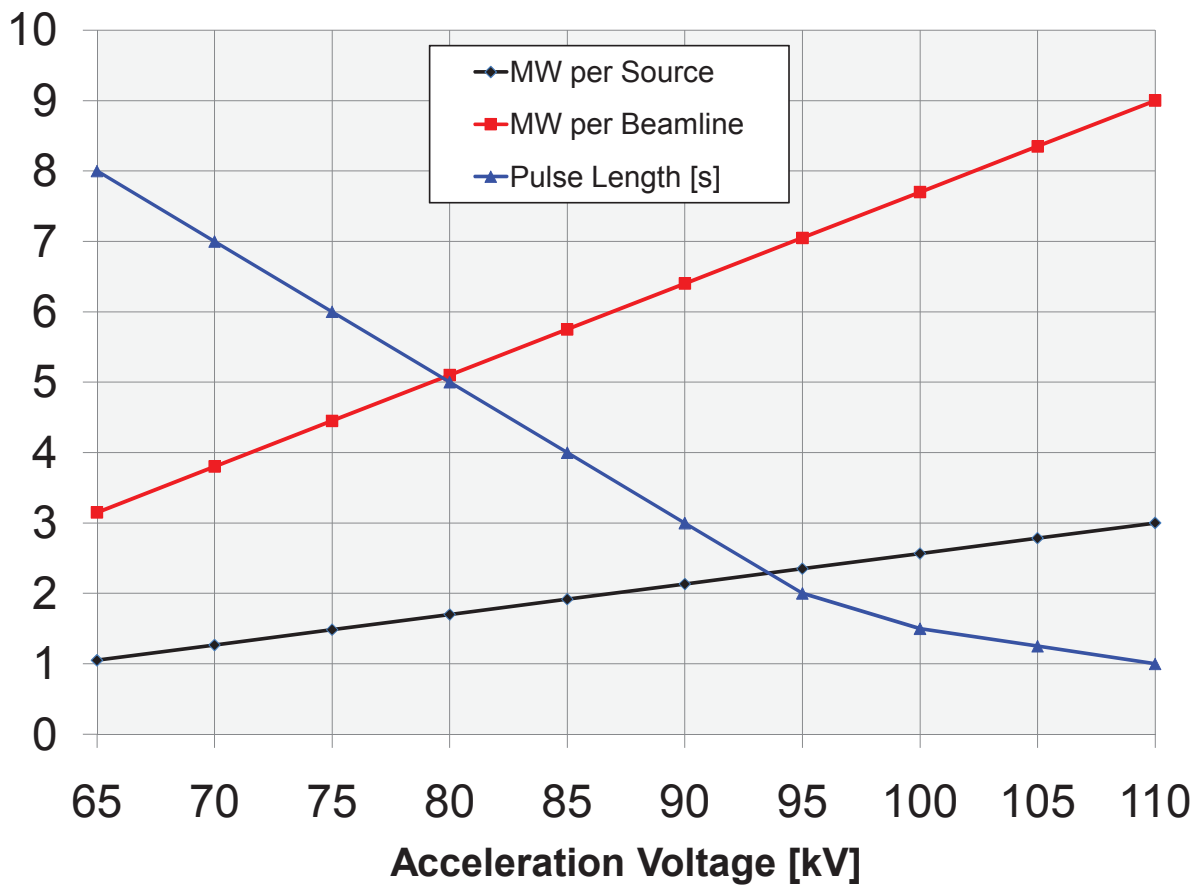
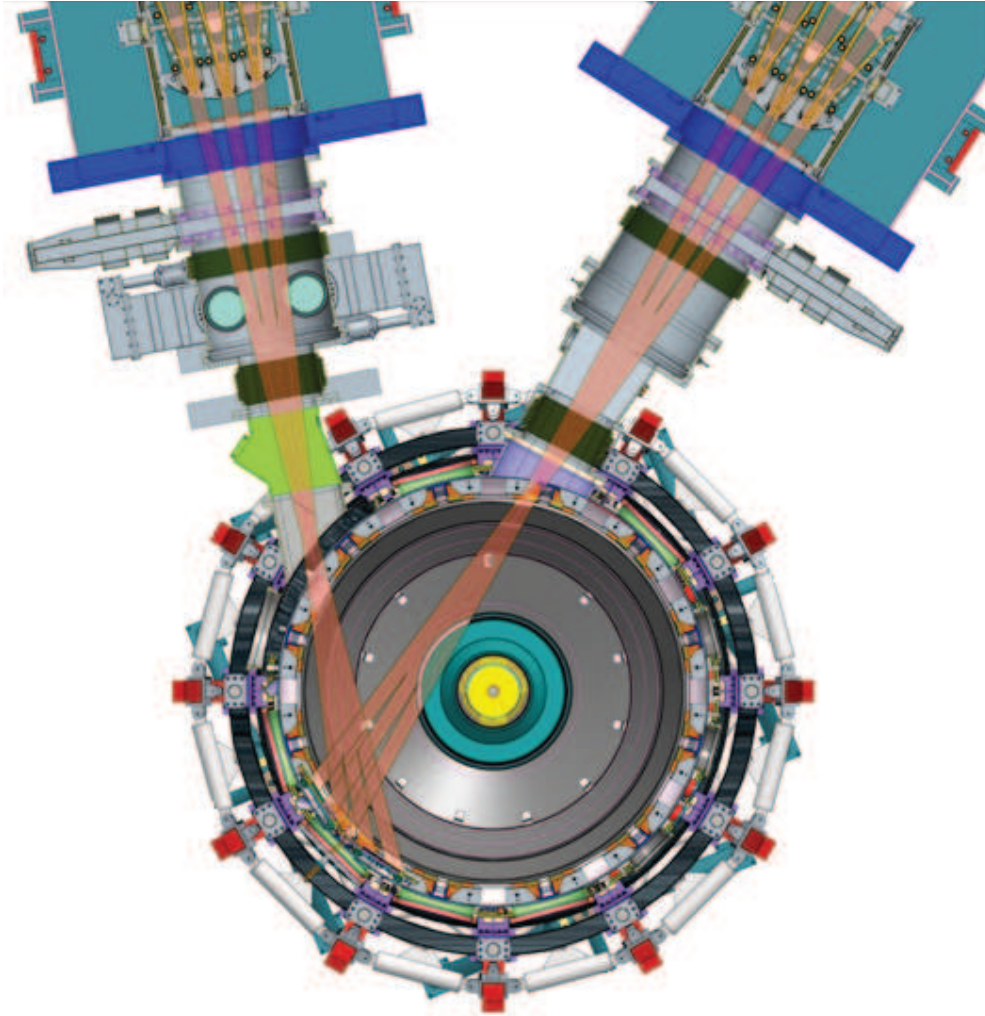


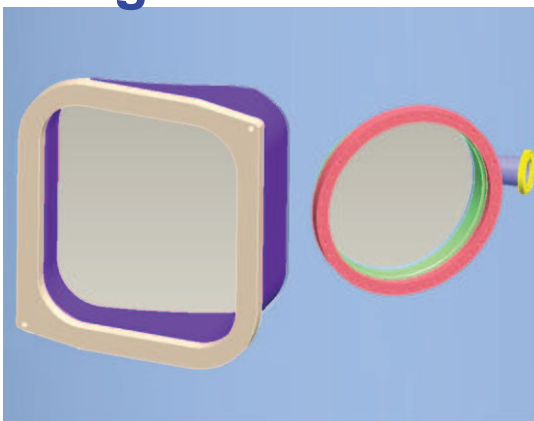
**Figure 19.** NSTX NBI power per source, power per beamline, and nominal maximum pulse-length versus NBI acceleration voltage.

(a) **New 2<sup>nd</sup> NBI** ( $R_{\text{TAN}}=110, 120, 130\text{cm}$ ) **Present NBI** ( $R_{\text{TAN}} = 50, 60, 70\text{cm}$ )



(b)

**Original NBI Port**



**New NBI Port**

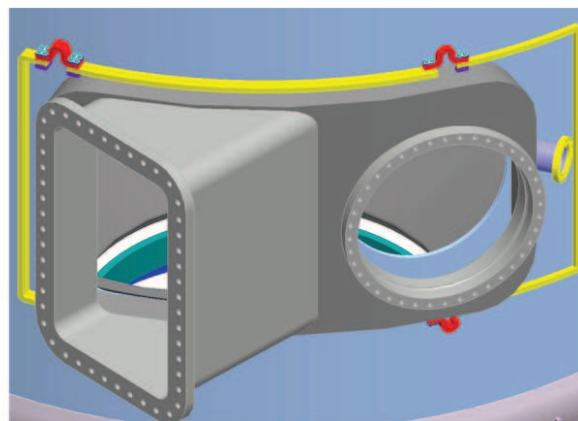


**Figure 20.** (a) Injection geometry of present and new 2nd NBI, and (b) modification of the present NBI port to a new NBI port cap to enable the more tangential injection.



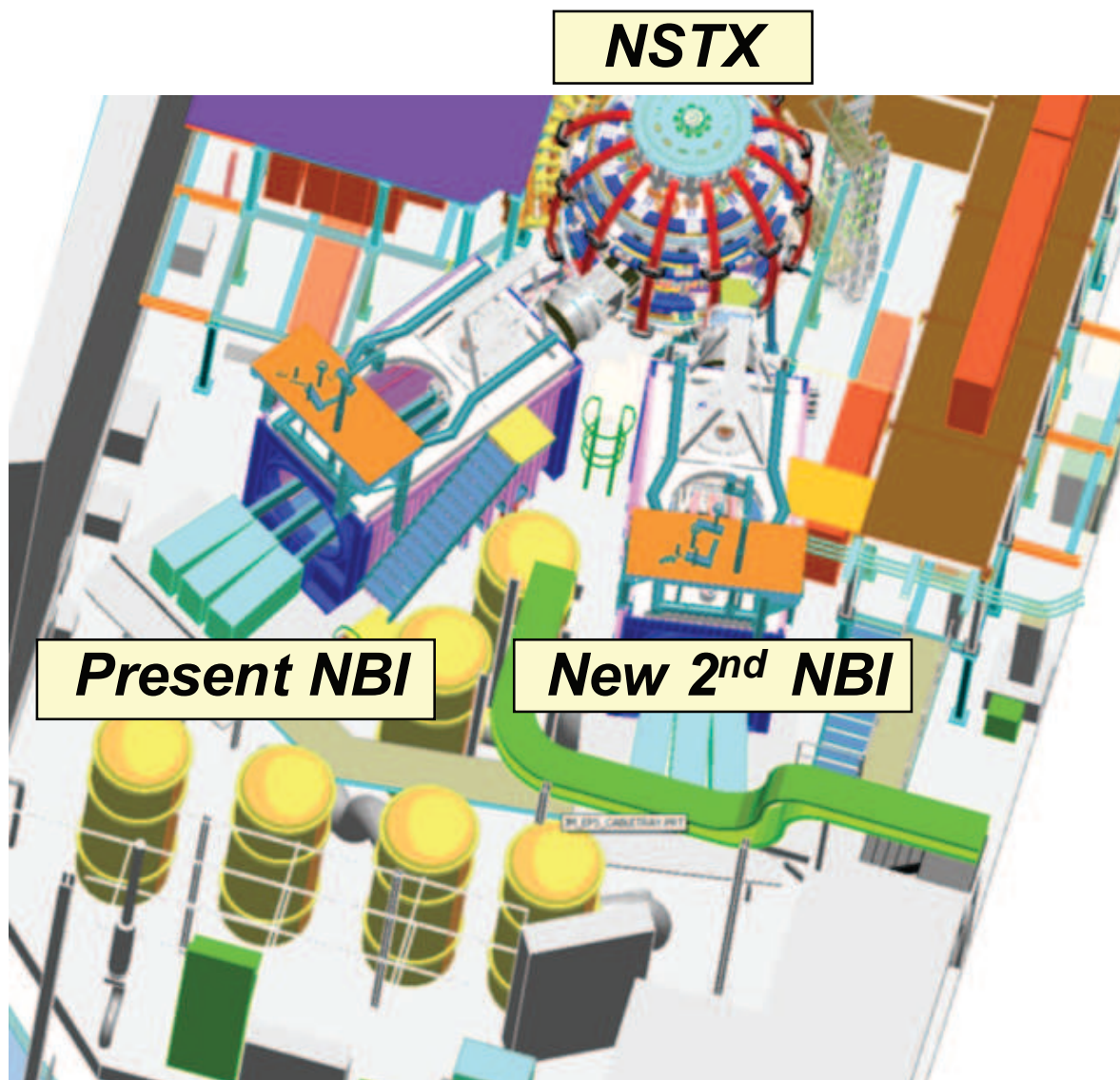


**Figure 21.** Drawing of top-down view of layout of NSTX test cell after installation of new 2nd NBI.

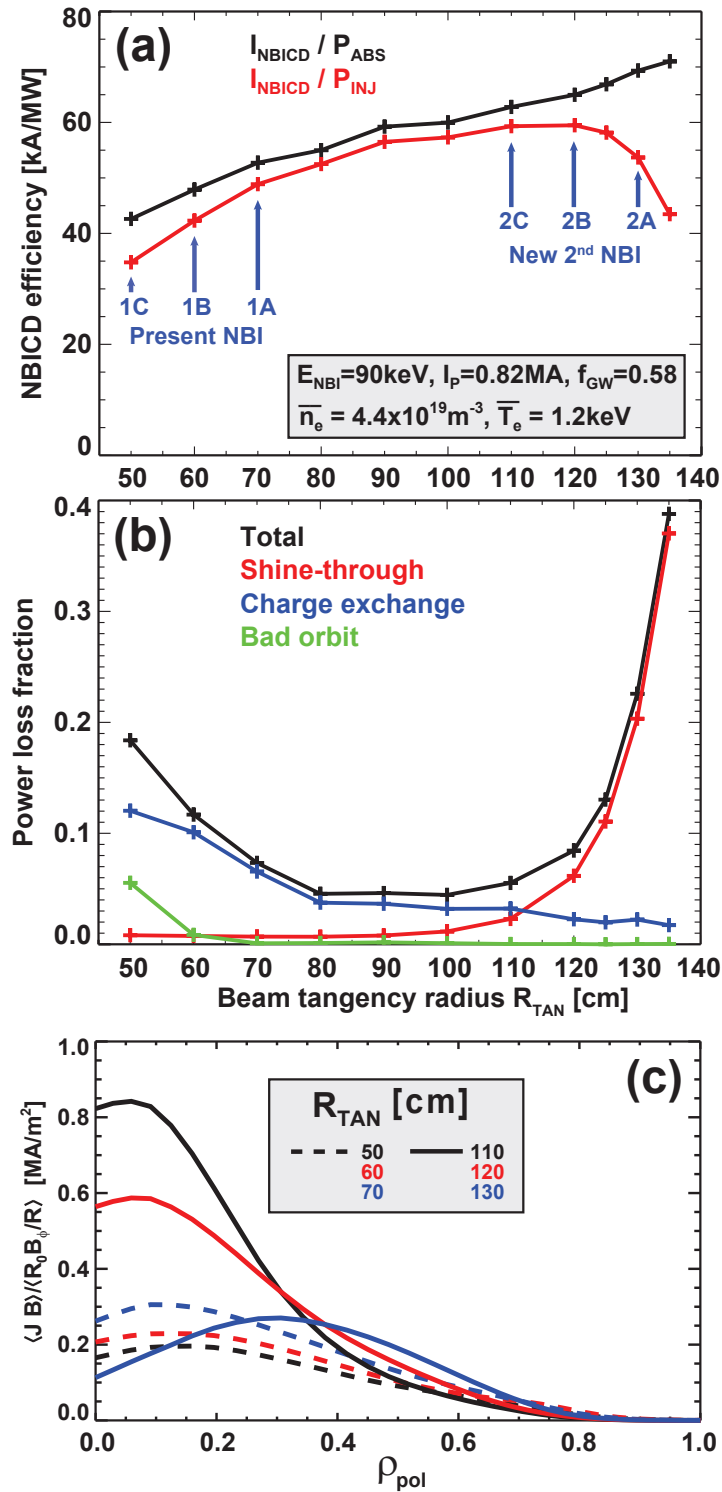


**Figure 22.** (a) NBI current drive efficiency (kA/MW) and (b) power loss fractions (total, shine-through, charge exchange, and bad orbit) as a function of beam tangency radius  $R_{TAN}$ , (c) NBI current drive parallel current density profiles vs. minor radius for the tangency radii of the present (dashed) and new 2nd NBI (solid) for an  $A=1.45$ ,  $I_P = 0.82\text{MA}$ ,  $B_T = 0.55T$  NSTX target plasma with a 13cm outer gap.

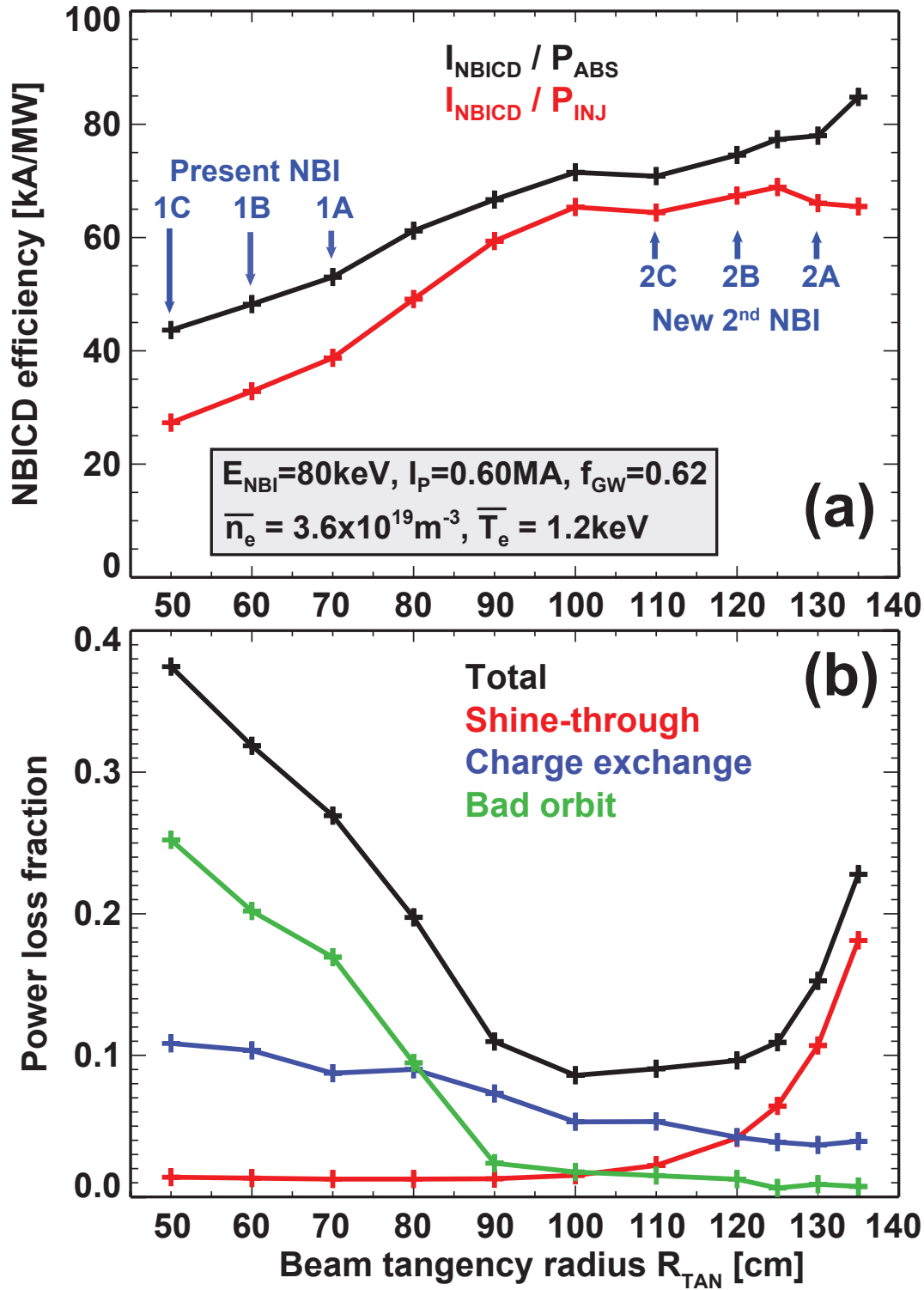


**Figure 23.** (a) NBI current drive efficiency (kA/MW) and (b) power loss fractions (total, shine-through, charge exchange, and bad orbit) as a function of beam tangency radius  $R_{TAN}$  for an  $A=1.65$ ,  $I_p = 0.60 \text{ MA}$ ,  $B_T = 0.9T$  NSTX Upgrade target plasma with a 7.4cm outer gap.

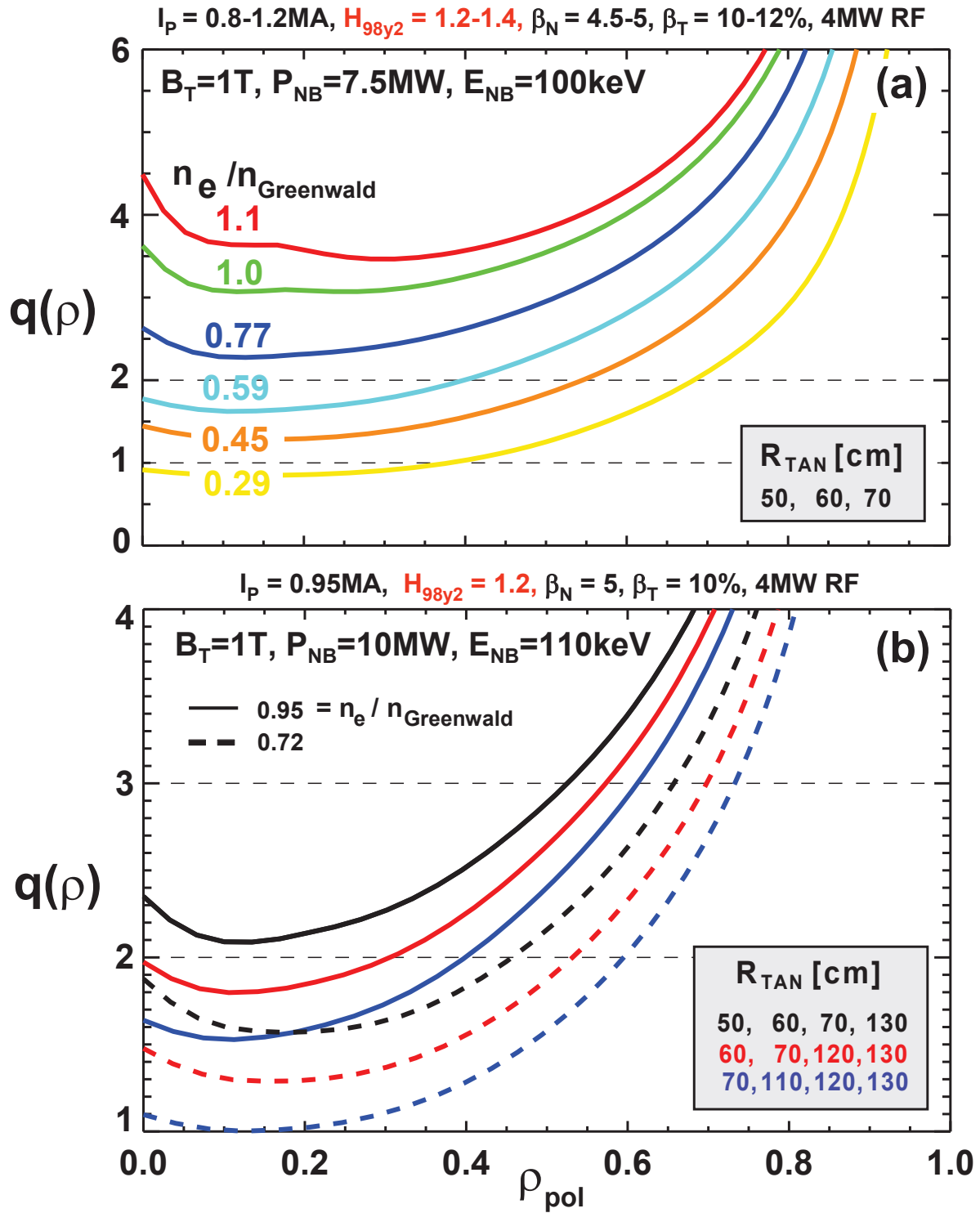


**Figure 24.** (a) Comparison of parallel current density profiles for existing (dashed) and 2nd (solid) NBI sources, and  $q$  profile controllability vs. density for (b) existing and (c) additional NBI sources for NSTX Upgrade target plasmas with  $A = 1.65-1.7$ ,  $\kappa = 2.6-2.7$ , and outer gap = 7.5cm.

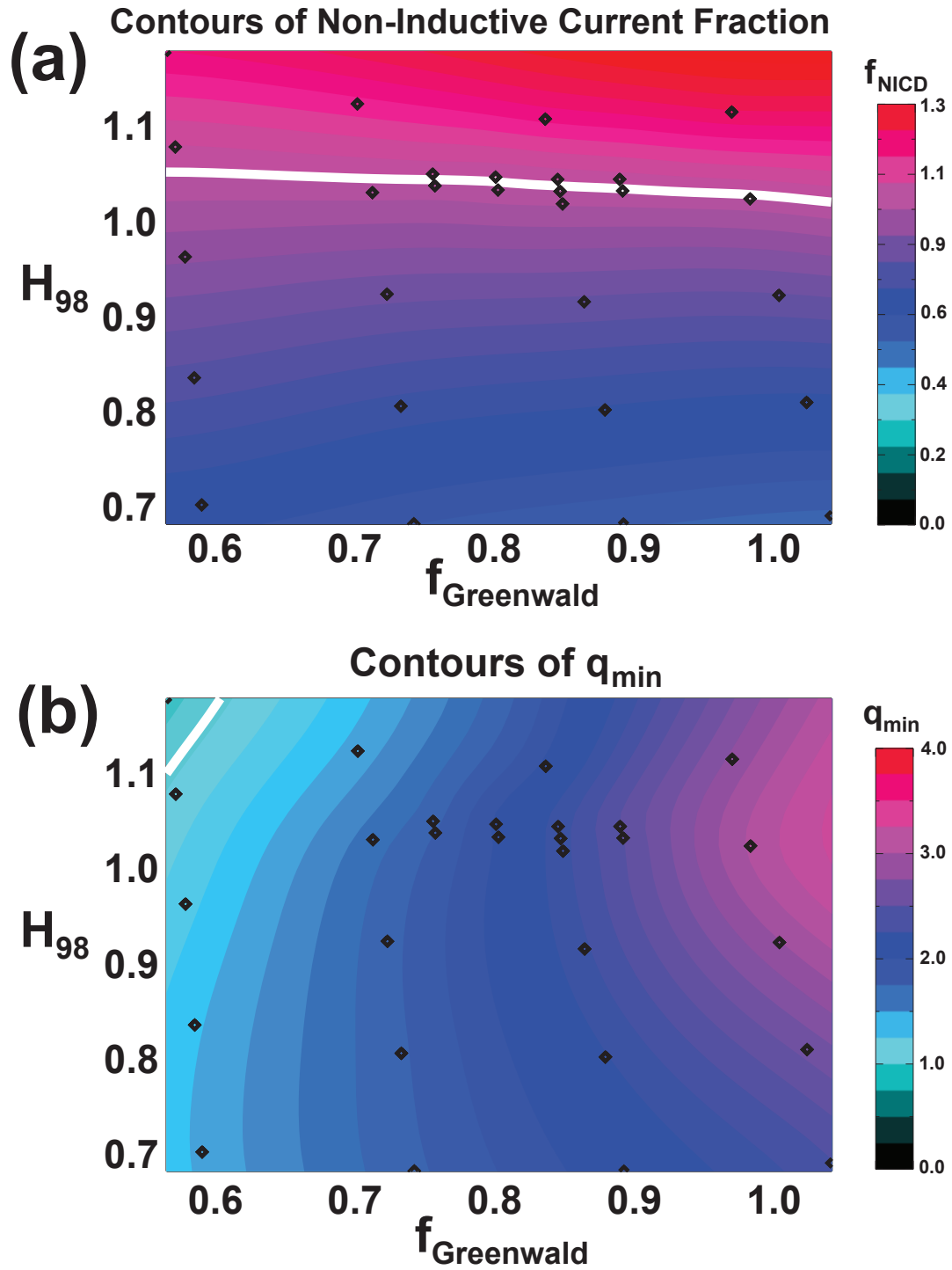


**Figure 25.** Contours of (a) non-inductive current fraction and (b) minimum safety factor  $q_{\min}$  versus  $f_{\text{Greenwald}}$  and ITER H-mode confinement multiplier  $H_{98}$  for 1MA plasmas with 12MW of NBI heating.



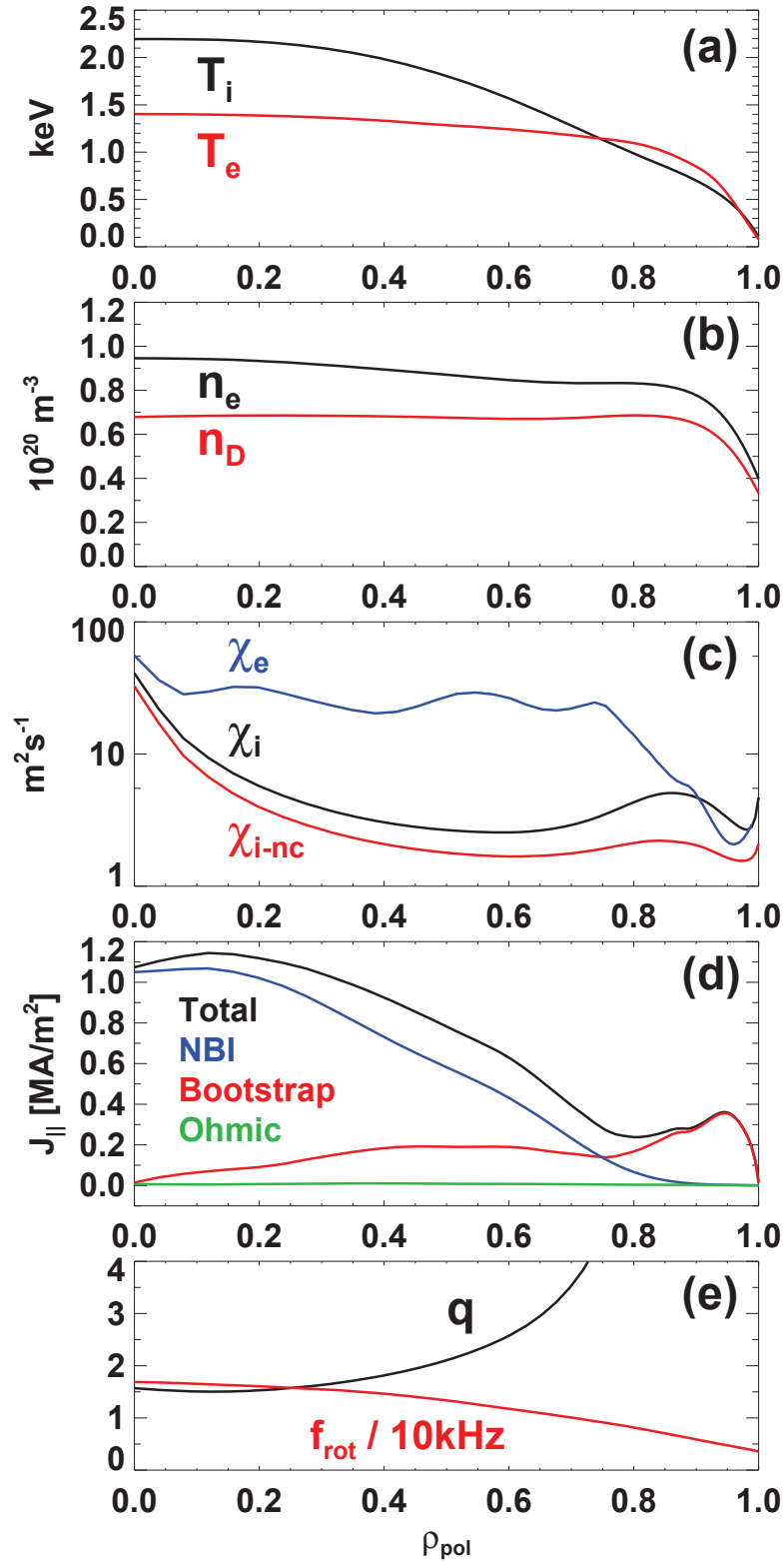


**Figure 26.** Profiles of (a) ion and electron temperature ( $T_i, T_e$ ), (b) electron and deuterium density ( $n_e, n_D$ ), (c) electron and ion thermal diffusivity ( $\chi_e, \chi_i$ ), (d) parallel current density ( $J_{||}$ ) including inductive/ohmic and non-inductive components, and (e) effective charge and safety factor ( $Z_{eff}, q$ ), for a TRANSP simulation of a 100% non-inductive NSTX Upgrade plasma with  $I_P=0.975\text{MA}$  and  $B_T = 1\text{T}$ .

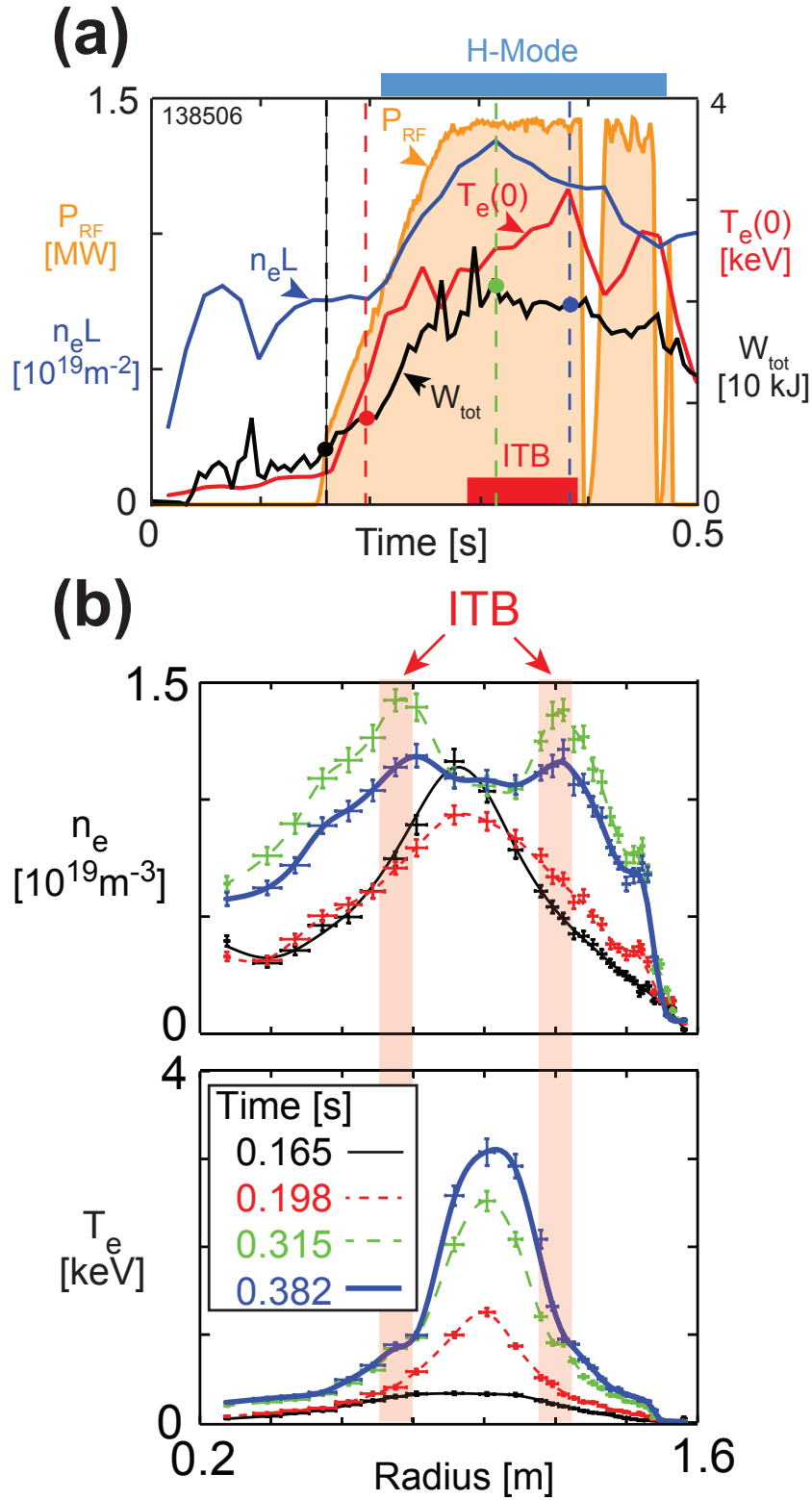


**Figure 27.** (a) Time evolution of  $n_e L$ ,  $T_e(0)$ ,  $W_{tot}$  and  $P_{RF}$  for an  $I_P = 300$  kA,  $B_T = 0.55$  T HHFW deuterium H-mode (shot 138506) using  $k_\phi = -8 \text{m}^{-1}$  RF heating, (b)  $n_e$  and  $T_e$  profiles show the development of an H-mode pedestal as the RF power is ramped up followed by the formation of an electron internal transport barrier (eITB).

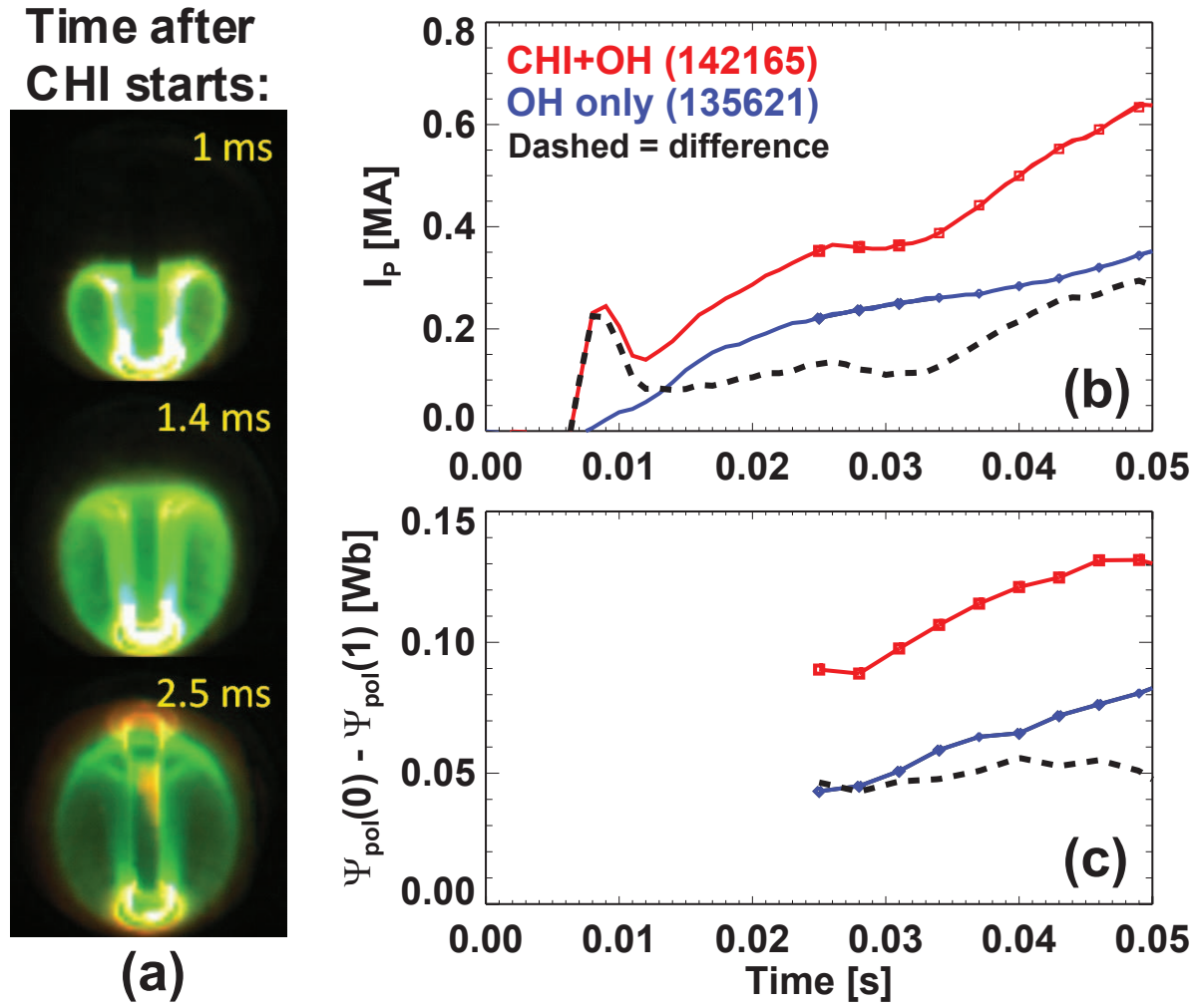


**Figure 28.** (a) Evolution of CHI plasma boundary light shortly after plasma formation, (b) plasma current savings and (c) poloidal flux savings from CHI coupled to induction in NSTX start-up plasmas.

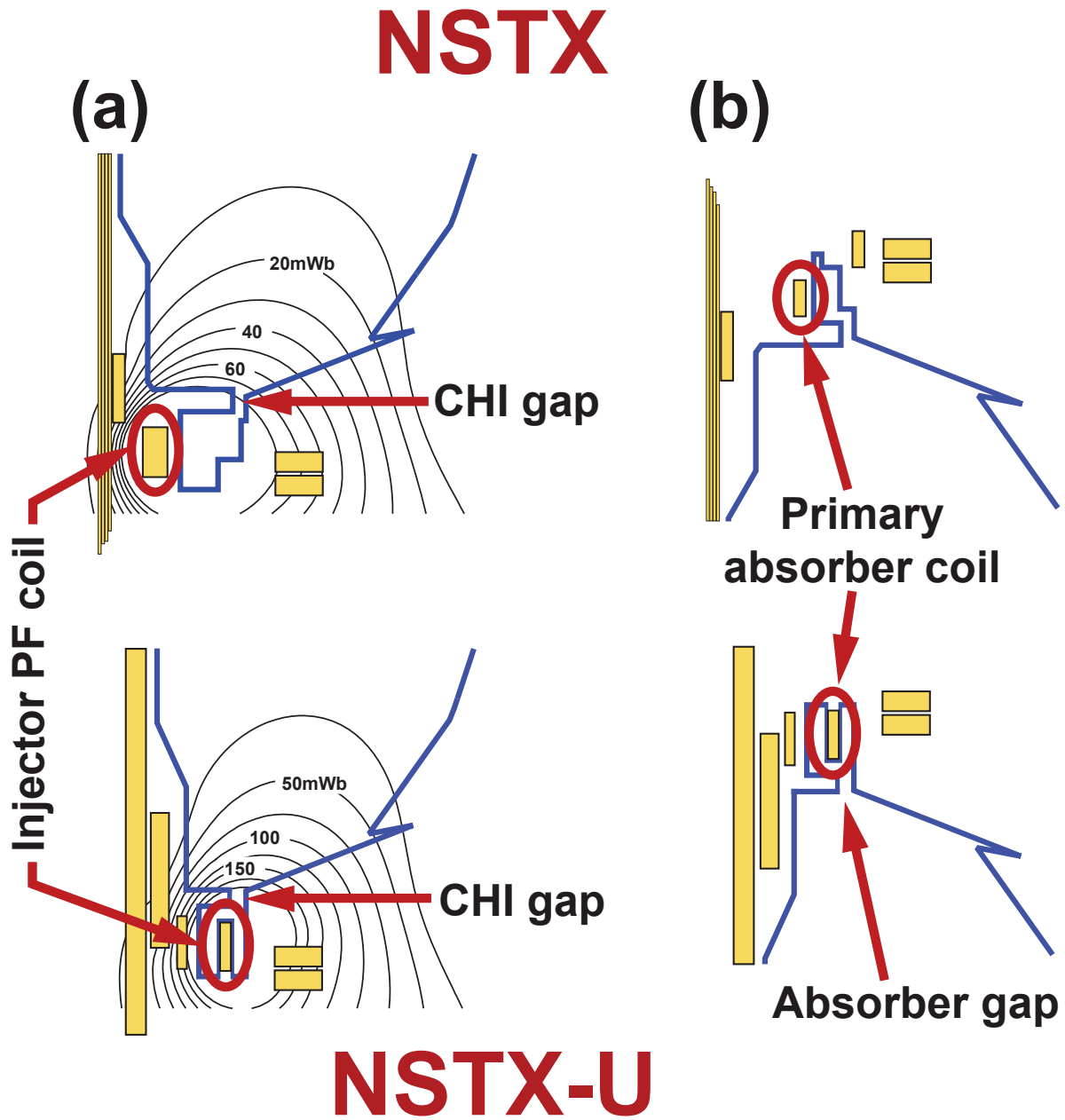


**Figure 29.** (a) Poloidal flux contours in the injector region of NSTX (top) and NSTX-U (bottom), and (b) field-nulling and divertor coils in the absorber region for CHI experiments.

Parameters	NSTX	NSTX-U	ST-FNSF	ST Pilot Plant
Aspect ratio: A	1.30	1.50	1.50	1.70
Elongation: $\kappa$	2.6	2.8	3.1	3.3
Major radius: $R_0$ [m]	0.86	0.93	1.2	2.2
Minor radius: a [m]	0.66	0.62	0.80	1.29
Toroidal field at $R_0$ : $B_T$ [T]	0.55	1	2.2	2.4
TF rod current: $I_{TF}$ [MA]	2.4	4.7	13.2	26.4
Toroidal flux: $\Phi_T$ [Wb]	2.5	3.9	15.8	45.7
Reference maximum sustained plasma current: $I_{PS}$ [MA]	1	2	10	18
Start-up plasma normalized internal inductance: $I_i$	0.35	0.35	0.35	0.35
Injector flux footprint: d [m]	0.6	0.56	0.73	1.17
Injector flux for projecting start-up current: $\psi_{inj}$ [Wb]	0.047	0.10	0.66	2.18
Bubble-burst current: $I_{bb}$ [kA]	3.3	9.0	79	165
Injector current: $I_{inj}$ [kA]	4.0	10.8	95	198
Start-up plasma flux: $\psi_p$ [Wb]	0.04	0.08	0.53	1.74
Start-up plasma current achieved or projected: $I_P$ [MA]	0.20	0.40	2.00	3.60
Current multiplication: $I_P / I_{inj}$	50	37	21	18
Multiplication limit: $\Phi_T / \psi_{inj}$	53	38	24	21
Injector current density [kA/m <sup>2</sup> ]	4.9	12	63	39

**Table 3.** Achieved parameters for CHI plasma formation in NSTX and projections to NSTX-U, ST-FNSF, and ST Pilot Plant

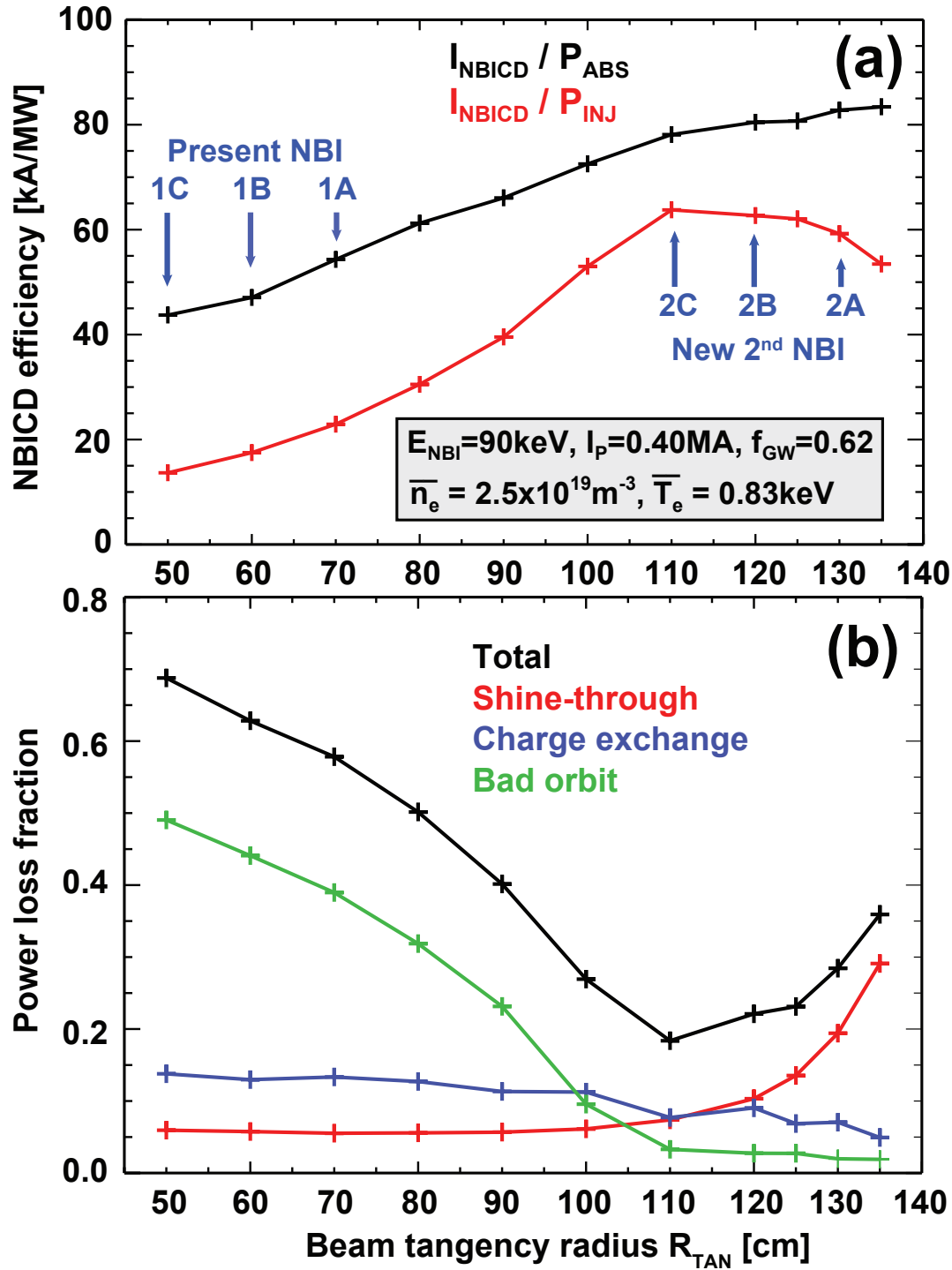


**Figure 30.** (a) NBI current drive efficiency (kA/MW) and (b) power loss fractions (total, shine-through, charge exchange, and bad orbit) as a function of beam tangency radius  $R_{TAN}$  for an  $A=1.65$ ,  $I_P = 0.40 \text{ MA}$ ,  $B_T = 0.9 \text{ T}$  NSTX Upgrade target plasma with a 7.4cm outer gap.

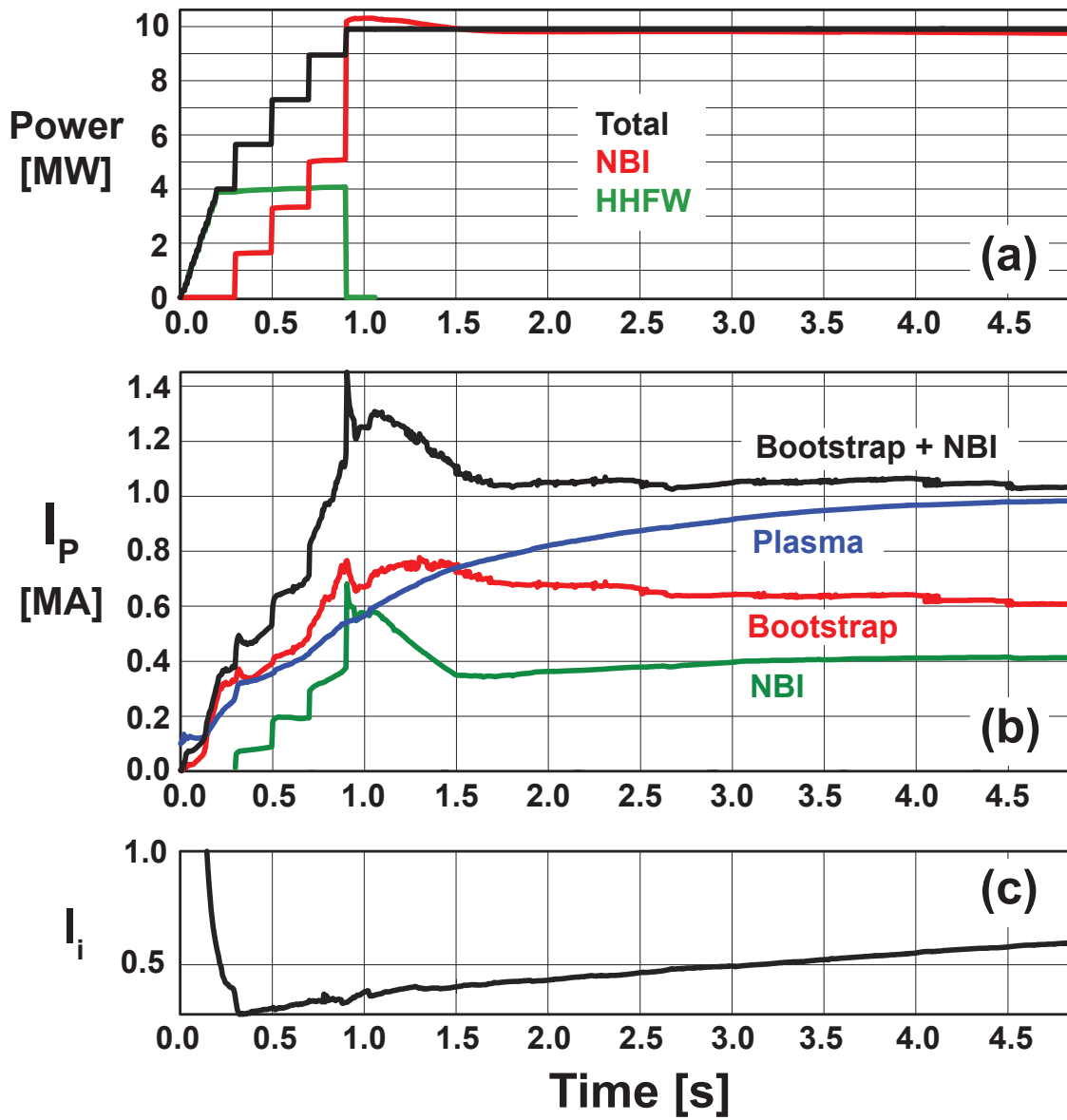


**Figure 31.** Evolution of (a) heating powers, (b) plasma current components, and (c) internal inductance from TSC simulations of plasma-current ramp-up to  $I_P = 1\text{MA}$  without using the ohmic solenoid.

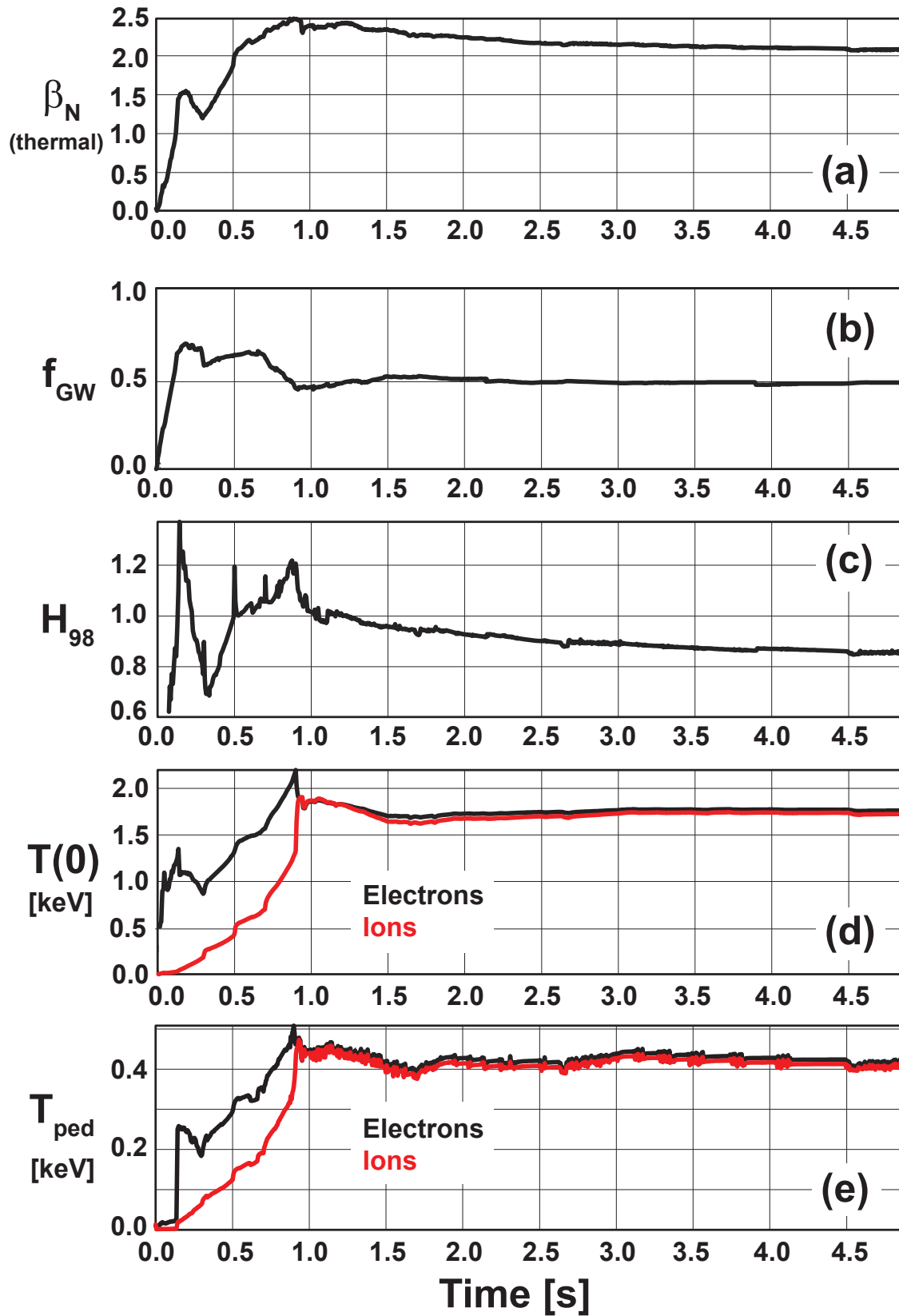


**Figure 32.** Evolution of (a) normalized beta (thermal component), (b) Greenwald fraction, (c)  $H_{98}$ , (d) central electron and ion temperatures, and (e) H-mode pedestal electron and ion temperatures from TSC simulations of plasma-current ramp-up to  $I_P = 1\text{MA}$  without using the ohmic solenoid. The H-mode is triggered at  $t=0.12\text{s}$  in the simulations.



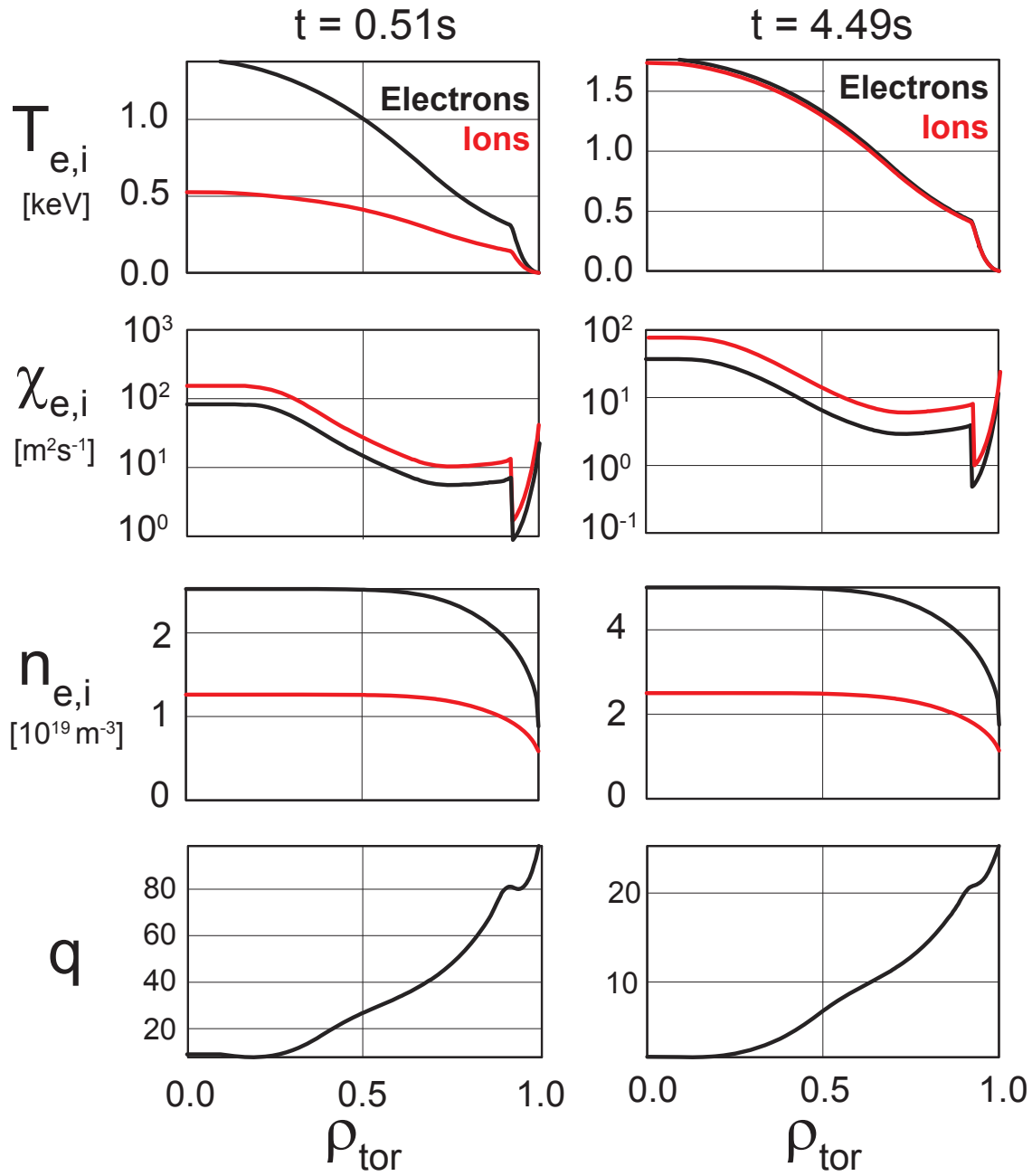


**Figure 33.** Profiles of the electron and ion temperatures, thermal diffusivities, and densities, and  $q$  profiles from TSC simulations of plasma-current ramp-up without using the ohmic solenoid. The profiles are plotted for two times in the simulations: early in the ramp-up ( $t=0.51\text{s}$ ,  $I_P=0.35\text{MA}$ ), and later in time ( $t=4.5\text{s}$ ) when the plasma current ( $I_P=1\text{MA}$ ) is nearly equal to the NBI+bootstrap overdrive current.

Category	Scenario Index	Disruption scenario description	Initial position index	Final position index	VDE drift time [ms]	$I_p$ quench time [ms]	$I_p$ quench rate [GA/s]	Halo fraction $f_h$
1	1	Centered disruption, fast quench	1	1		1	2	0
1	10	Centered disruption, medium quench	1	1		4	0.5	0
2	2	Initiated shifted to CS, fast quench, no halo	2	2		1	2	0
2	6	Inward drift to CS, very slow quench, halo	1	2	10	100	0.02	0.2
2	11	Inward drift to CS, fast quench, halo	1	2	10	1	2	0.2
2	12	Inward drift to CS, medium quench, halo	1	2	10	4	0.5	0.2
2	19	Inward drift to CS, fast quench, no halo	1	2	10	1	2	0
2	20	Inward drift to CS, medium quench, no halo	1	2	10	4	0.5	0
2	21	Inward drift to CS, slow quench, no halo	1	2	10	40	0.05	0
3	3	Initiated shifted down to inboard, fast quench, no halo	3	3		1	2	0
3	7	Vertical drift to inboard, very slow quench, halo	1	3	10	100	0.02	0.35
3	13	Vertical drift to inboard, fast quench, halo	1	3	10	1	2	0.35
3	14	Vertical drift to inboard, medium quench, halo	1	3	10	4	0.5	0.35
3	22	Vertical drift to inboard, fast quench, no halo	1	3	10	1	2	0
3	23	Vertical drift to inboard, medium quench, no halo	1	3	10	4	0.5	0
3	24	Vertical drift to inboard, slow quench, no halo	1	3	10	40	0.05	0
4	4	Initiated shifted down to middle, fast quench, no halo	4	4		1	2	0
4	8	Vertical drift to middle, very slow quench, halo	1	4	10	100	0.02	0.35
4	15	Vertical drift to middle, fast quench, halo	1	4	10	1	2	0.35
4	16	Vertical drift to middle, medium quench, halo	1	4	10	4	0.5	0.35
4	25	Vertical drift to middle, fast quench, no halo	1	4	10	1	2	0
4	26	Vertical drift to middle, medium quench, no halo	1	4	10	4	0.5	0
4	27	Vertical drift to middle, slow quench, no halo	1	4	10	40	0.05	0
5	5	Initiated shifted down to outboard, fast quench, no halo	5	5		1	2	0
5	9	Vertical drift to outboard, very slow quench, halo	1	5	10	100	0.02	0.35
5	17	Vertical drift to outboard, fast quench, halo	1	5	10	1	2	0.35
5	18	Vertical drift to outboard, medium quench, halo	1	5	10	4	0.5	0.35
5	28	Vertical drift to outboard, fast quench, no halo	1	5	10	1	2	0
5	29	Vertical drift to outboard, medium quench, no halo	1	5	10	4	0.5	0
5	30	Vertical drift to outboard, slow quench, no halo	1	5	10	40	0.05	0

Table 4. Disruption scenarios used for stress analysis for NSTX-Upgrade.

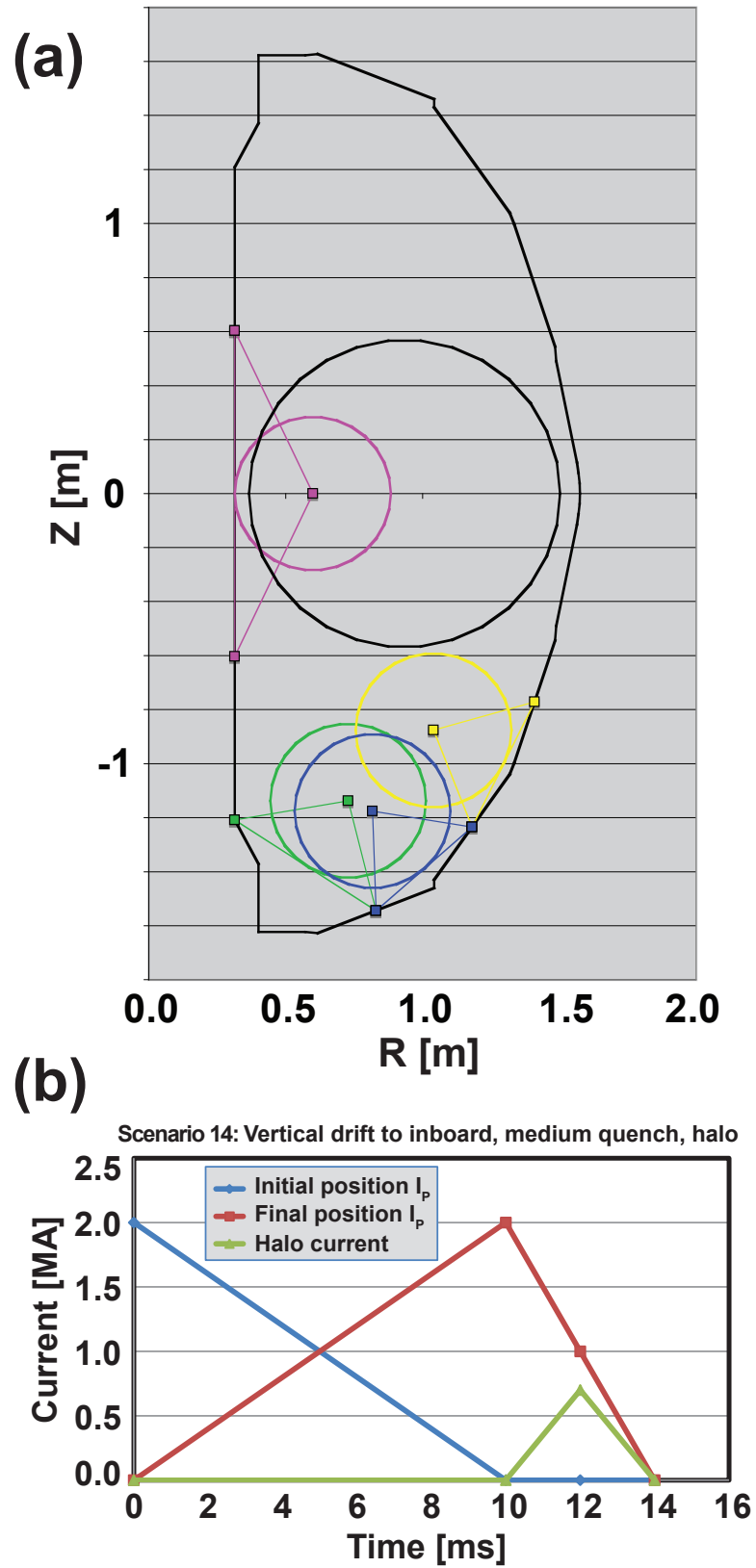


**Figure 34.** (a) Locations and sizes of disrupting plasmas (circles) and halo current entry and exit points (box symbols) on the limiter boundary used in stress analyses, and (b) time evolution of plasma current at initial position (blue) and final position (red), and halo current (green) for a representative VDE to the inboard divertor: Scenario 14 in Table 4.

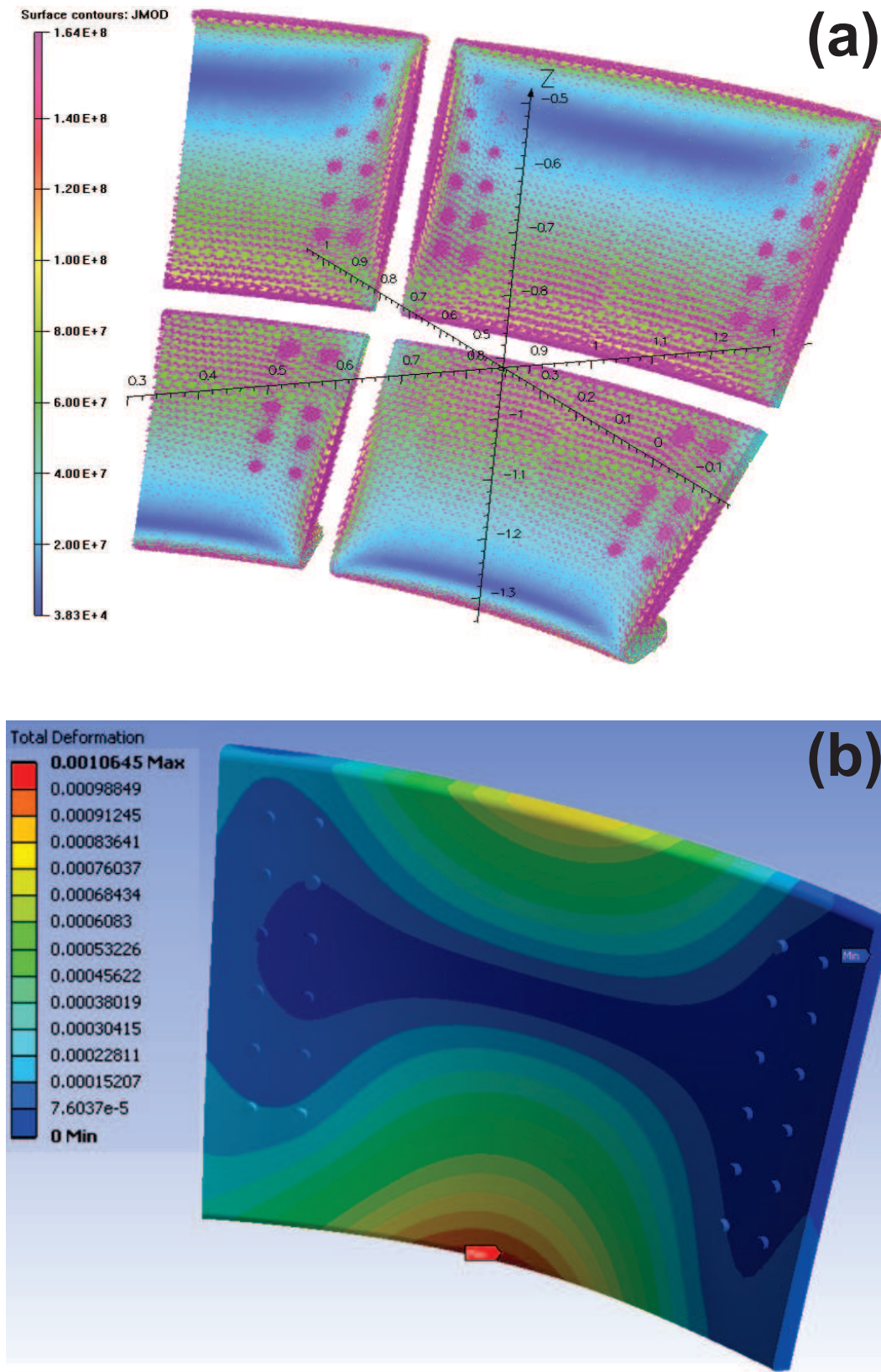


**Figure 35.** (a) Passive plate current density [ $A/m^2$ ] and (b) primary passive plate deflection [m] during a simulated downward VDE.

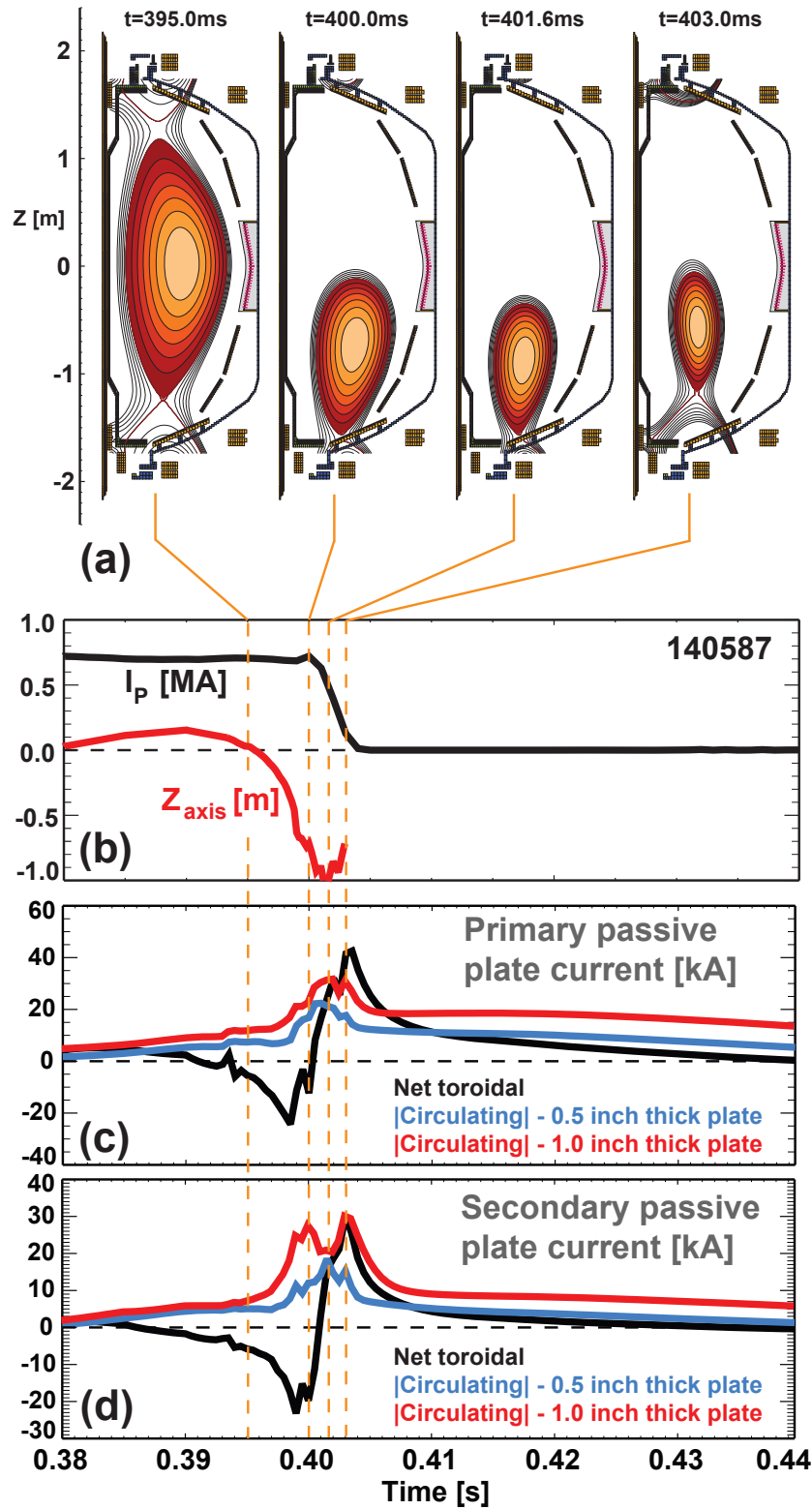


**Figure 36.** (a) Plasma position and shape evolution, (b) plasma current and magnetic axis position, (c) primary passive plate currents and (d) secondary passive plate currents during a vertical displacement event (VDE) and current quench in NSTX.

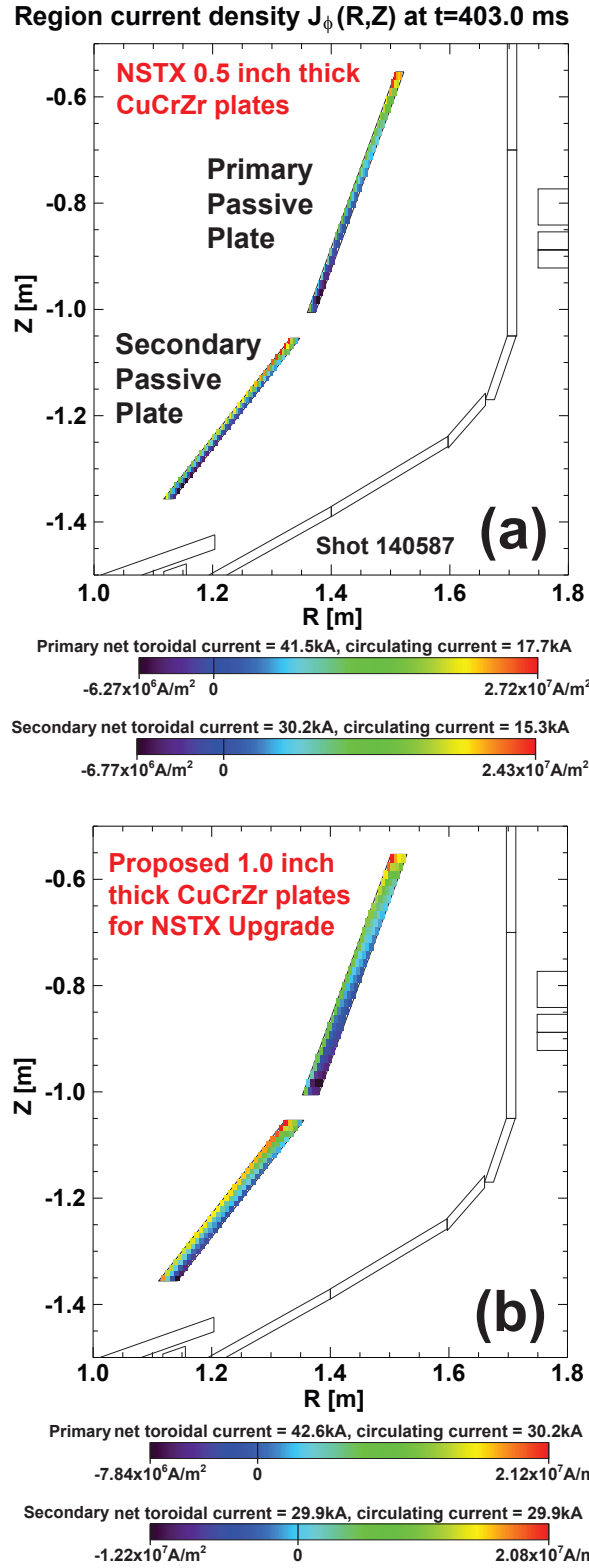


**Figure 37.** Toroidal current density in the primary and secondary passive plates at the time of peak net toroidal current and near the time of peak circulating current for (a) the present NSTX passive plates and (b) thicker passive plates being assessed for NSTX Upgrade for the shot shown in Figure 36.

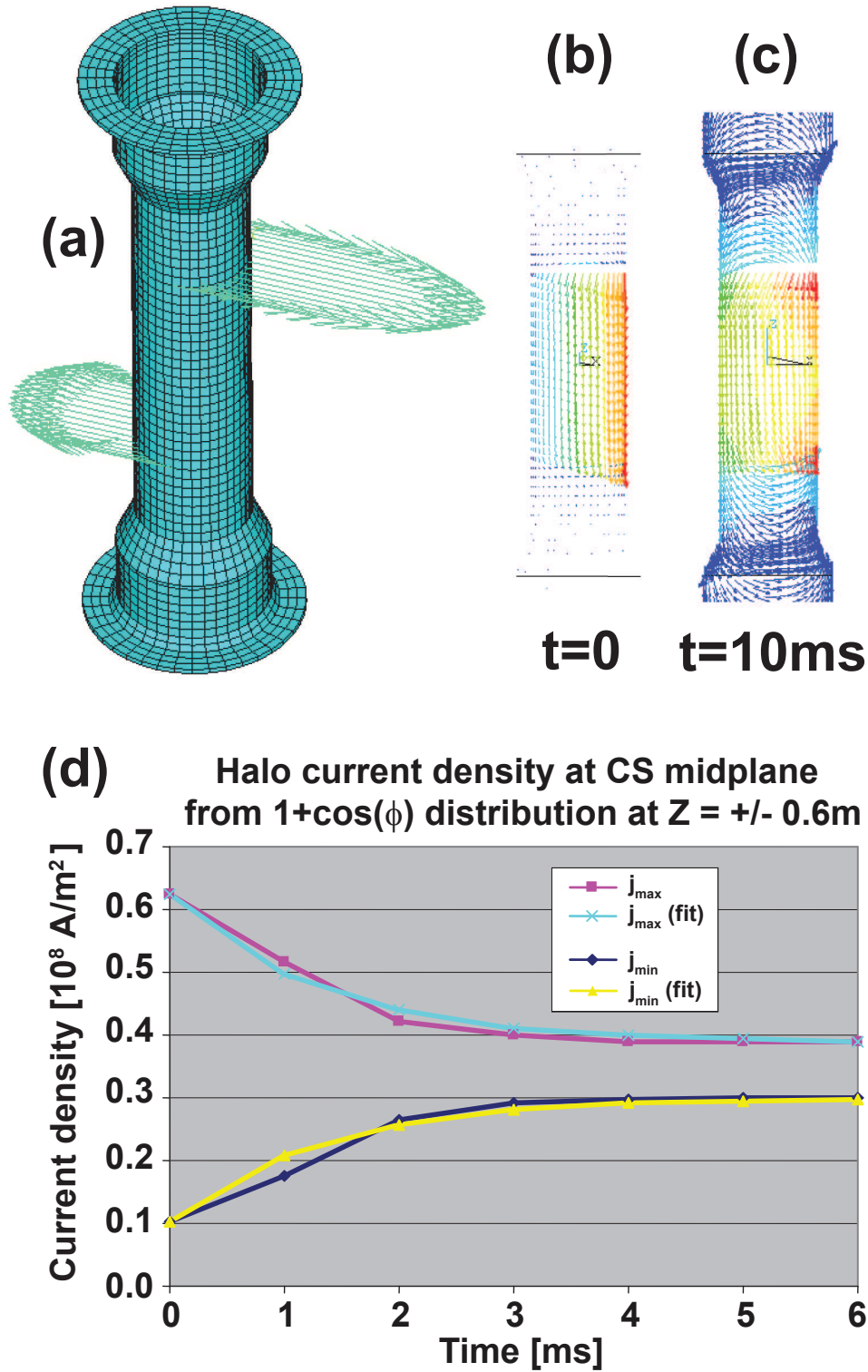


**Figure 38.** (a) Distribution of current injected into center-stack (CS) casing to simulate halo current strike with toroidal peaking factor of 2, (b) (inductive) distribution of halo current on CS casing immediately following halo current strike, (c) (resistive) distribution of halo current 10ms after halo strike, and (d) halo current density at the CS mid-plane versus time after strike.



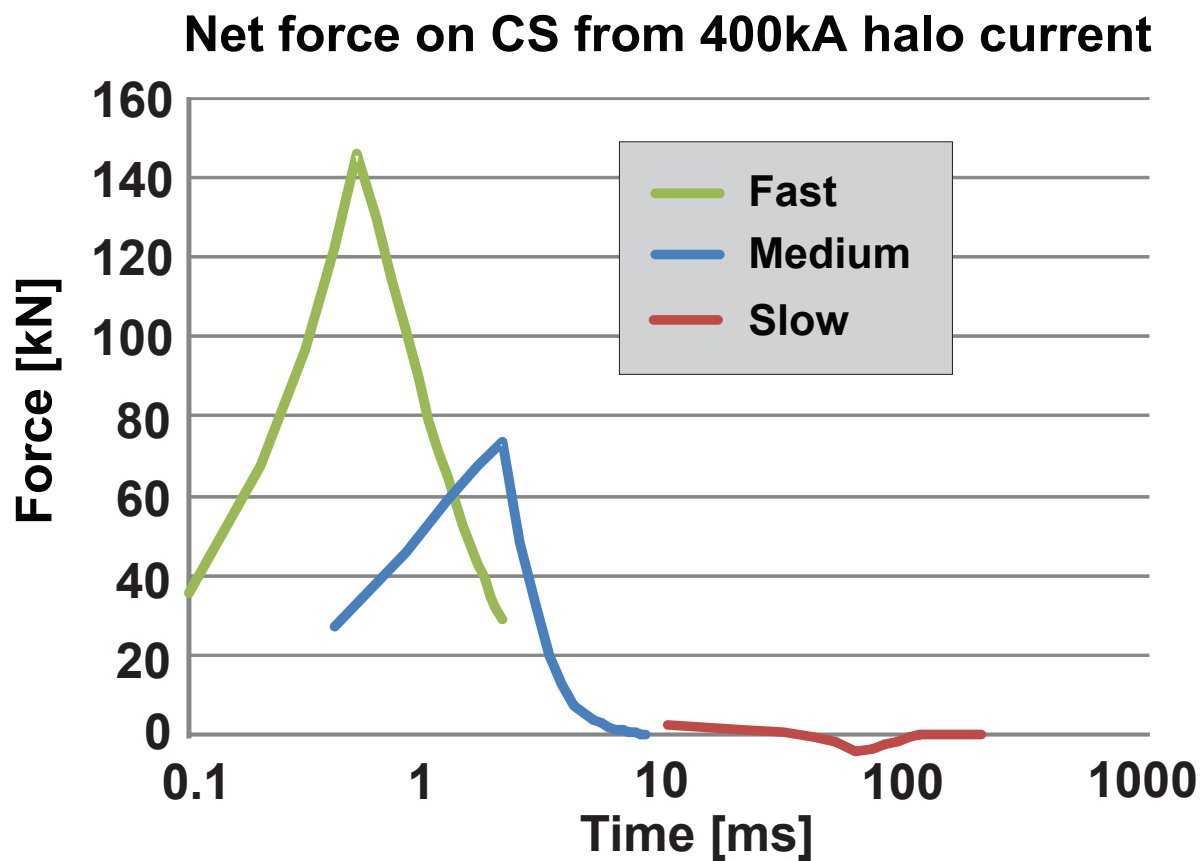


**Figure 39.** Net force on the center-stack from halo currents driven by fast, medium, and slow current-quenches for disruption scenario indices 11, 12, and 6 respectively in Table 4. Note the log scale used on the time axis.



### VALEN model of NSTX Upgrade

#### (a) passive conducting structure

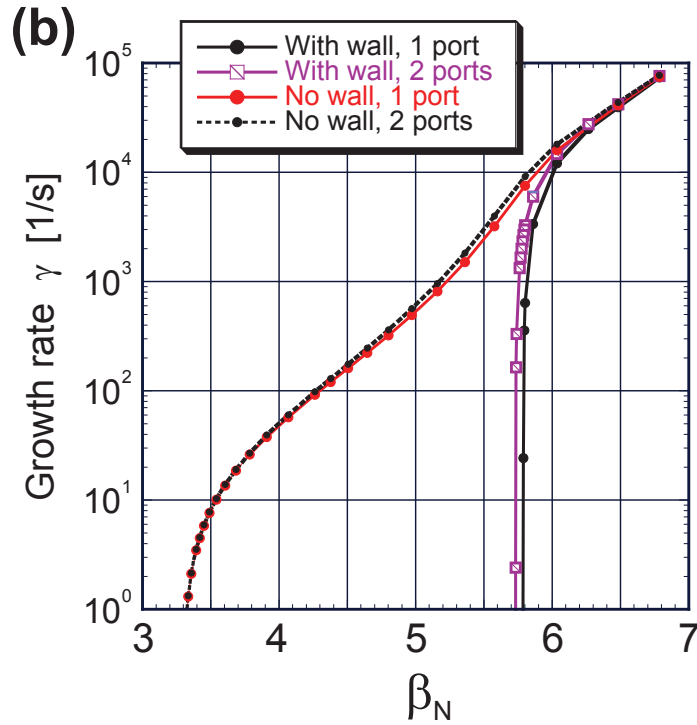
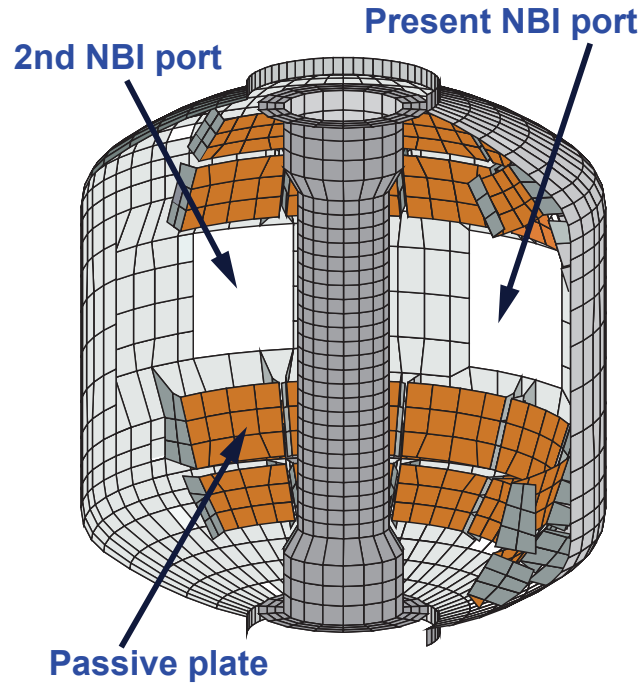


**Figure 40.** (a) VALEN model of the NSTX Upgrade passive conducting structure including the vessel cut-outs for the present and 2nd NBI ports and (b) predicted  $n=1$  RWM growth rate vs.  $\beta_N$  for one and two vessel penetrations for NBI ports.

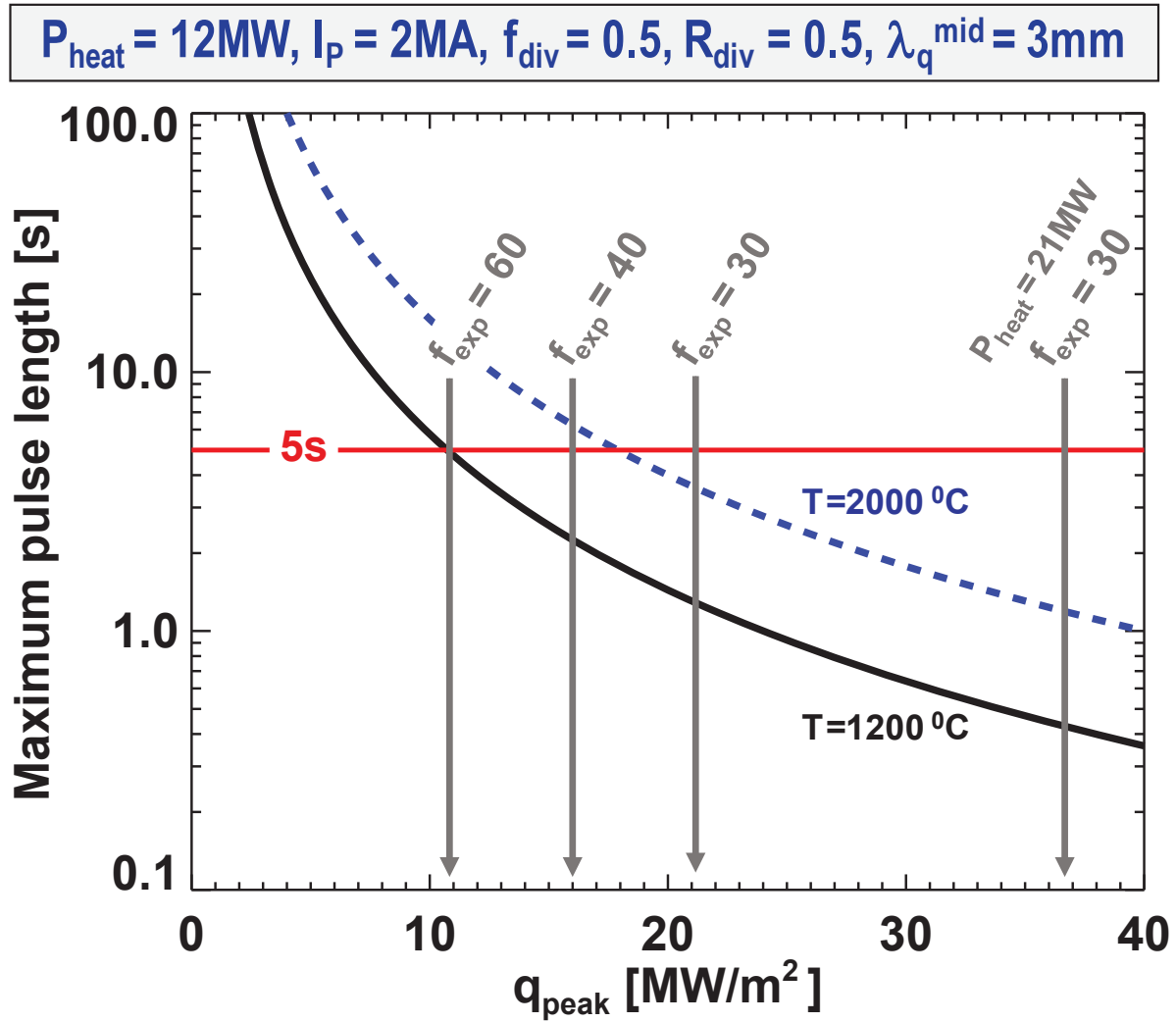


**Figure 41.** Projected NSTX Upgrade pulse-length limits versus peak divertor heat flux for two divertor carbon PFC temperature values.

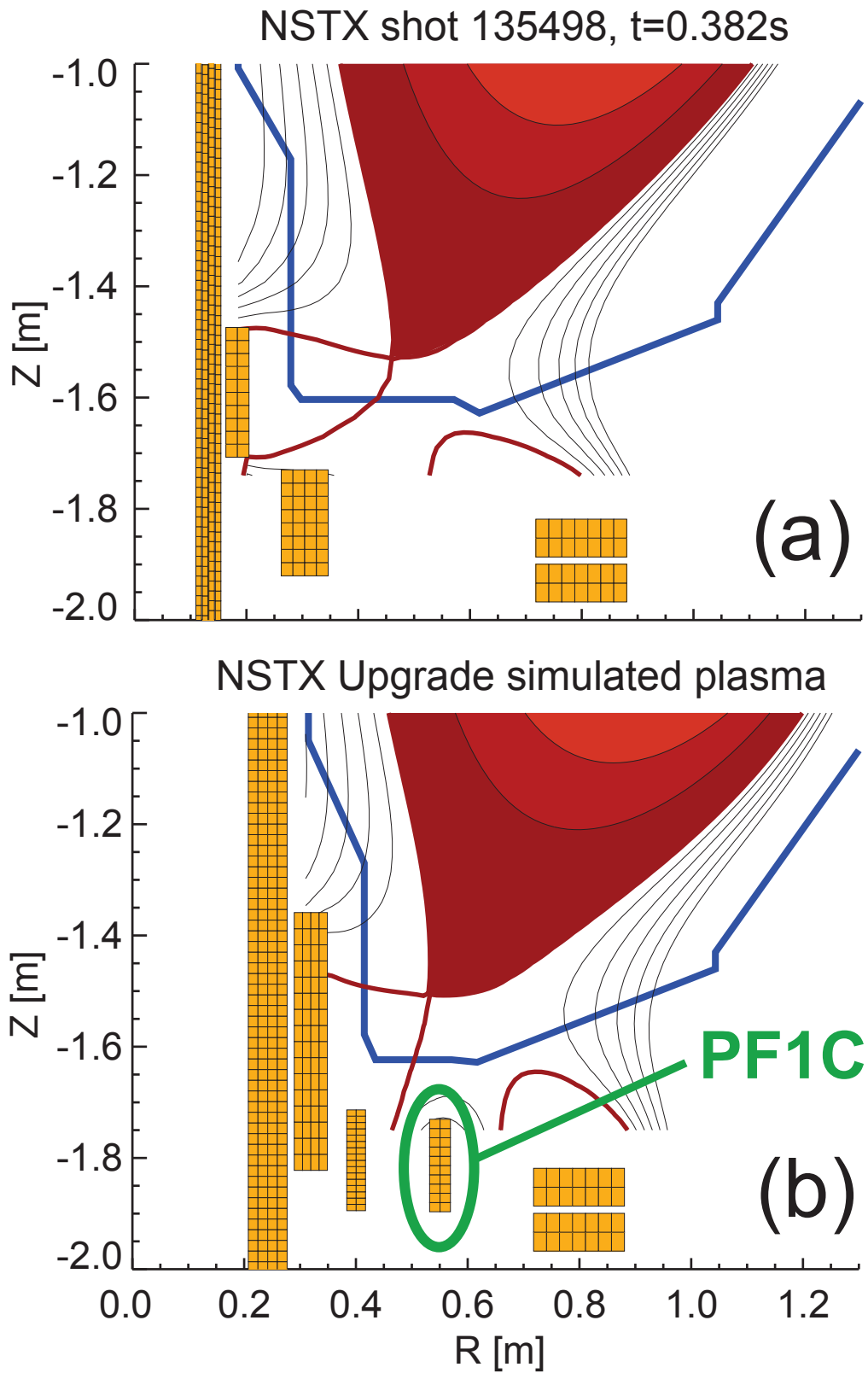


**Figure 42.** (a) Snowflake divertor in NSTX and (b) NSTX Upgrade.

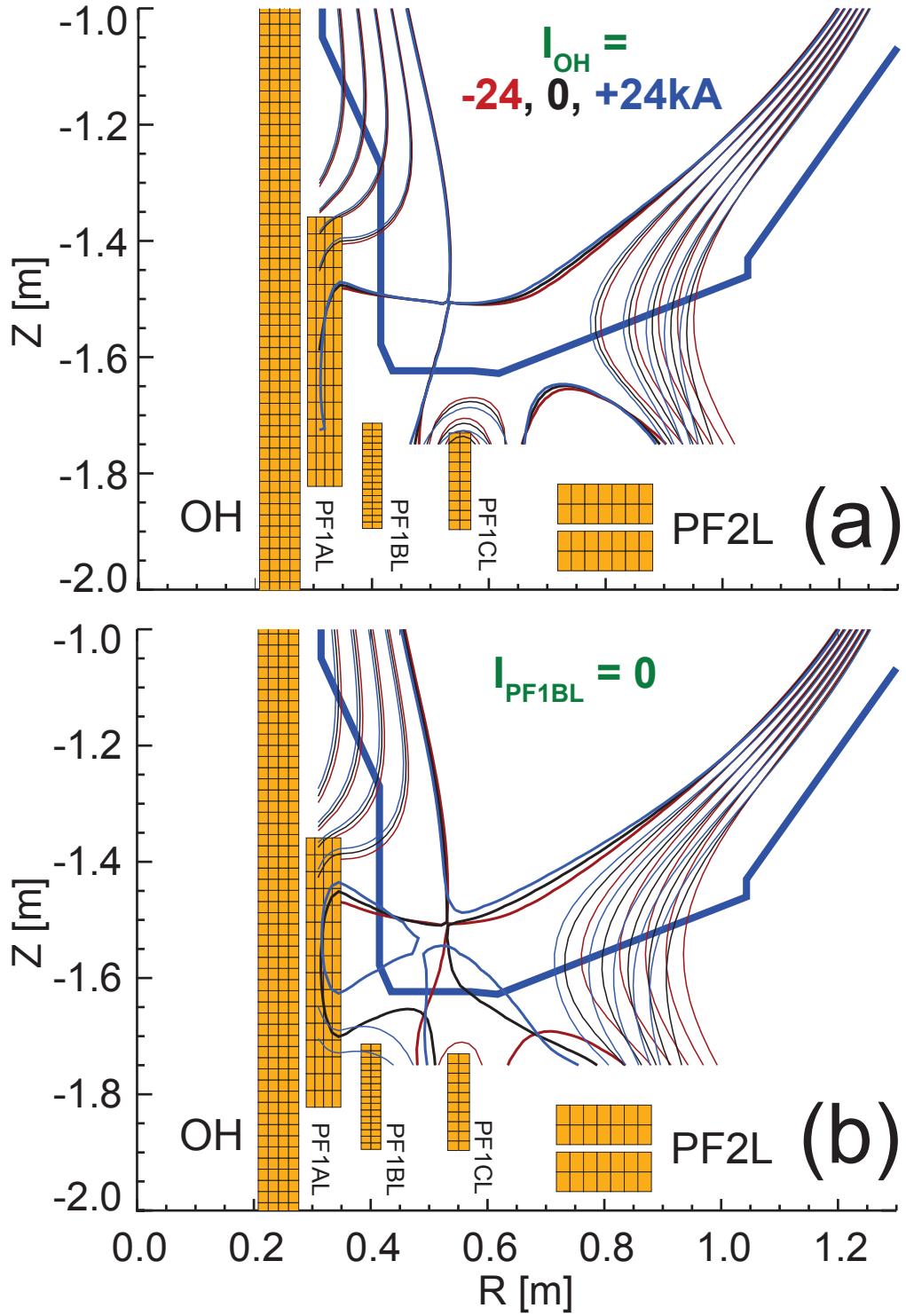


**Figure 43.** (a) Overlay of boundaries in NSTX Upgrade as a function of ohmic heating solenoid current  $I_{OH}$  utilizing all divertor PF coils, (b) overlay of snowflake boundaries versus  $I_{OH}$  but with constraint of zero PF1B current.

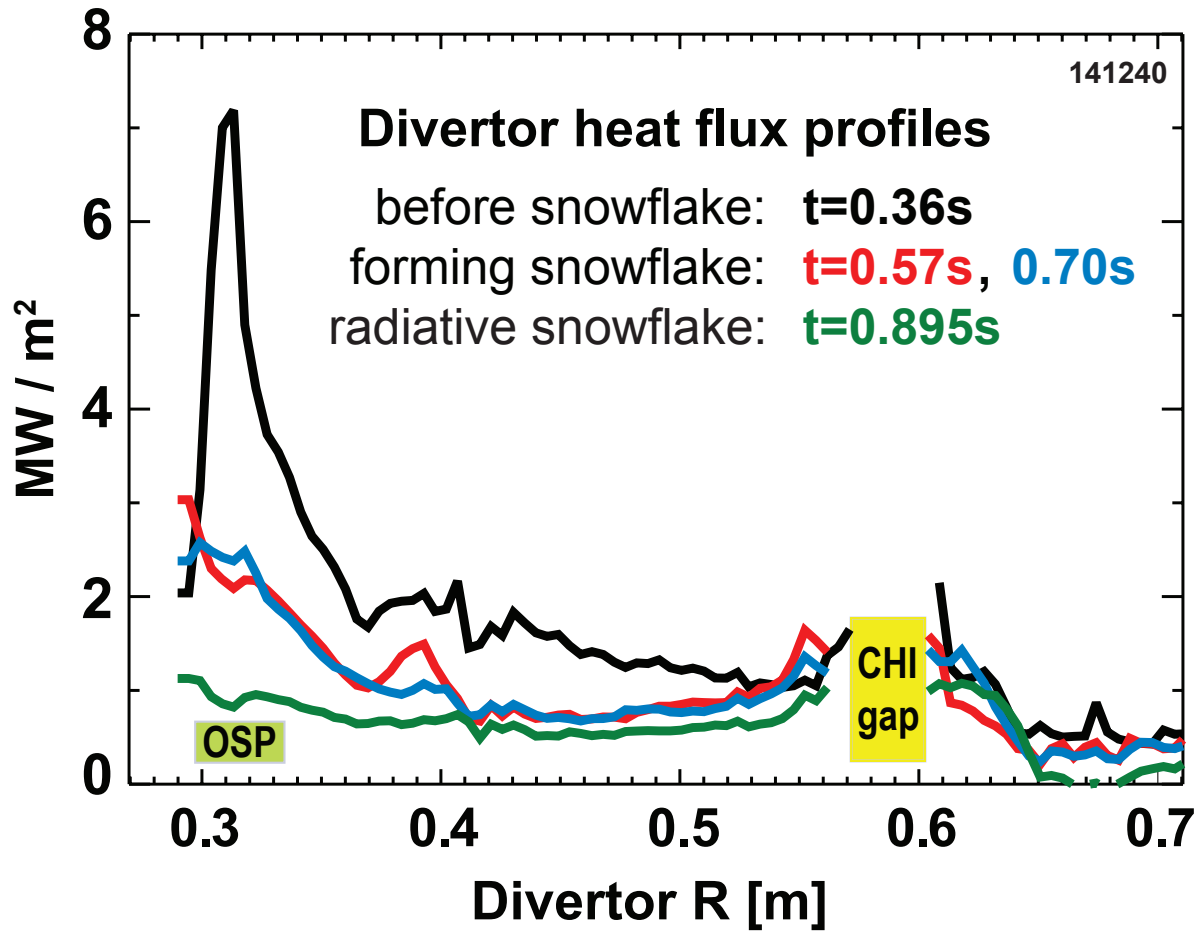


**Figure 44.** Peak heat flux in a standard divertor configuration in NSTX (black) compared to the snowflake divertor configuration (red and blue), and a partially detached "radiative" snowflake (green) obtained at different times in the same discharge.